AN ABSTRACT OF THE THESIS OF

Joel Walenza-Slabe for the degree of Master of Science in Materials Science presented on December 20, 2012.
Title: Sputtered $Pb(Zr_{0.52}Ti_{0.48})O_3$ (PZT) Thin Films on Copper Foil Substrates.

Abstract approved:

_____

Brady J. Gibbons

$Pb(Zr_{0.52}Ti_{0.48})O_3$ (PZT) thin films are of interest for their large dielectric permittivity, ferroelectric, and piezoelectric properties. The material has been widely studied for use in high frequency transducers, multi-layered capacitors, and ferroelectric random access memory. Copper foils are an inexpensive, flexible substrate with a low resistivity which makes them ideal for many transducer and capacitor applications.

PZT thin films on copper foils were produced by RF sputtering and crystallized under reducing conditions. Causes and prevention of a cuprous oxide interlayer are discussed. The film structure was characterized by XRD, SEM, and AFM. The permittivity was low, but remanent polarization increased to as high as ~40 $\mu C/cm^2$ as film thickness and crystallization temperature increased.

Residual stresses were measured by x-ray diffraction using the $\sin^2\psi$ method. The relative permittivity of the PZT/Cu films was measured as a function of applied AC electric field. By performing a Rayleigh analysis on this data one can

determine the relative contributions of the intrinsic, reversible, and irreversible components to the permittivity. The residual stress could be correlated to the reversible part of the permittivity. The first order reversal curves (FORCs), which characterize the ferroelectric switching, give indications of the defect state of the film.

Cantilever energy harvesters were fabricated. Large electrodes were able to be evaporated onto the films after oxidizing pinholes and cracks on a hot plate. Devices were tested on a shaker table at < 100 Hz. A dynamic model based on Euler-Bernoulli beam equations was used to predict power output of the fabricated devices. The observed output was comparable to model predictions. Resonant frequency calculations were in line with observed first and second resonances at ~17 Hz and ~35 Hz which were also close to those predicted by the dynamic model.

Sputtered $Pb(Zr_{0.52}Ti_{0.48})O_3$ (PZT) Thin Films on Copper Foil Substrates

by
Joel Walenza-Slabe

A THESIS

submitted to

Oregon State University

in partial fulfillment of
the requirements for the
degree of

Master of Science

Presented December 20, 2012
Commencement June 2013

Master of Science thesis of Joel Walenza-Slabe presented on December 20, 2012.

APPROVED:

Major Professor, representing Materials Science

Director of the Materials Science Program

Dean of the Graduate School

I understand that my thesis will become part of the permanent collection of Oregon State University libraries. My signature below authorizes release of my thesis to any reader upon request.

Joel Walenza-Slabe, Author

ACKNOWLEDGEMENTS

I would like to express my sincere appreciation to my wife Casey and my sons Yuri and Sage for always giving me love and laughter, the two greatest gifts. Also, I would like to acknowledge the rest of my family, and their love.

Without the serial revisions of my advisor Brady Gibbons this would thesis would require only one of those little staples. He has a rigorous sensibility for what constitutes good science and it has been an honor to work under his guidance.

In particular, I would like to thank (the now) Dr. Yu Hong Jeon for many helpful suggestions and discussions. It has been a great pleasure to work alongside Kirsten and Bryan. Thanks to Ashley and Austin for their material aid on the AFM and for many helpful conversations. I am looking forward to working with our new group members soon. It's to the point where loneliness is never really an issue, even at 2 o'clock in the morning.

Thanks also to Dr. Cann and everyone across the hall. Troy has been a big help on this project. Thanks to everyone else in that group for giving me fantastic access to your lab and for all the great advice.

To the many people around campus who put their efforts into supporting research, you have my gratitude. This includes, but is by no means limited to, all of the folks in the machine shop in Rogers Hall, the Electron Microscopy Facility,

and the EECS cleanroom. Without these facilities and dedicated, knowledgeable operators and excellent management Oregon State University could not do the excellent research that it does.

I cannot remember how many times I have silently thanked my very first chemistry professor, Dr. Paul Smolenyak, a dedicated and inspiring teacher. Moreover, it has been my pleasure to work with astounding teachers at Oregon State University, Portland State University and Yavapai Community College.

My brother, who might also be a social-capitalist, has inspired me by always walking the Noble Eightfold Path. Also thanks to my friends in Portland, Prescott, and New Jersey who helped me to walk straight on many diversions.

Thanks to my committee members, Drs. Brady Gibbons, David Cann, John Conley, and Greg Herman for agreeing to be at the same place and time five days before Christmas to listen to my spiel. Your kind reading and insightful comments and suggestions for my thesis were greatly appreciated.

TABLE OF CONTENTS

TABLE OF CONTENTS (Continued)

Page

TABLE OF CONTENTS (Continued)

LIST OF FIGURES

LIST OF FIGURES (Continued)

Figure Page

LIST OF FIGURES (Continued)

Figure Page

LIST OF FIGURES (Continued)

LIST OF FIGURES (Continued)

Figure Page

LIST OF TABLES

This thesis is dedicated to
my mother and to my father.

1. Motivation

The motivation of this research was to demonstrate the deposition of $Pb(Zr_xTi_{1-x})O_3$ (lead zirconate titanate, or PZT) on copper foils via RF magnetron sputtering and *ex-situ* crystallization. PZT has been extensively researched and has been widely adopted by industry for use as acoustic transducers and actuators, particularly in bulk form. [1-4] In the last twenty years there has been much research into applications of PZT thin films for use in piezoelectric microelectromechanical systems (MEMS) as well as multilayer ceramic capacitors (MLCCs). [5-8] Much of this work has been conducted on $SrTiO_3$, sapphire, and platinum coated silicon substrates. The properties of these films have generally been very satisfactory. However, these substrates are mechanically rigid and relatively expensive which makes them unsuitable for all but the most specialized purposes.

On the contrary, copper is a cheap, mechanically compliant (as a foil), and highly electrically conductive substrate, which makes it an attractive substrate on which to deposit PZT. This has been demonstrated by several research groups over the last ten years, who generally used a solution deposition method to deposit the highest performing films. [9-12] Here, attempts to create films of similar quality using an RF magnetron sputtering technique are undertaken.

There are several advantages to sputtering versus solution methods to derive thin films. One can deposit films onto curved surfaces, which might be useful for

depositing on uniquely shaped components. Quality PZT films have been demonstrated using dip coating but this deposition method is non-selective and requires a chemical mask in order to avoid coating the entire substrate. [13, 14] Sputtering has applications in developing sensors for aerofoil and for mm-scale robotics. [15] Also, there are no organics involved in sputter deposition thus there could be implications for processes where the presence of organics is not permissible. Much research is currently focused on solution-based techniques, for good reason. The technology and energy associated with maintaining high vacuum deposition systems is costly both economically and environmentally. Yet, in the electronics industry, many processes are conducted entirely in vacuum and it may not be feasible to break the vacuum in order to insert an intermediate solution-based process. Often many tools can be fit into a large vacuum system and a sputtering process might be more convenient when used in such a system.

One application that is particularly suited for PZT on copper foil is a cantilevered energy harvester that, due to the compliance of the substrate, is expected to have a lower resonant frequency and allow the development of higher voltages across the device. The idea behind this device is that a piezoelectric material is mounted on a flexible substrate that absorbs atmospheric vibrations and bends, generating a voltage between electrodes placed across the sample. The choice of the substrate, substrate dimensions, and PZT thickness all affect the resonant frequency of the device. The device must be designed to take advantage of the amplitude and frequency of the vibration source while meeting the required

power output. The variety of vibration sources is numerous. Typical sources mentioned include acoustic vibrations in a building, on an underground pipeline, in a car, on a highway, on a railroad track, or attached to industrial equipment. Typically a thin film device would not generate a huge amount of power, but perhaps a small array might generate power in the realm of a few μW. The primary aim of such research is to place sensors alongside transmitters that can charge a small battery capable of intermittently relaying status information to a distant receiver. Technical details of cantilever energy harvesters will be discussed later.

Switching is another application for which a piezoelectric cantilever on copper foil could be used. High-frequency MEMS for switching is a new and exciting area of research. [16, 17] The foil is conductive and so can act as both the substrate and the bottom electrode, reducing the size of the device. The compliance of the substrate can decrease the electrical energy required to drive the device and increase the throw of the switch.

One of the primary advantages to the copper substrate is its mechanical compliance. Copper can be molded into an array of curved or irregularly shaped substrates. By properly designing sputtering system geometry, perhaps utilizing an advanced stage for rotating and translating the substrate during deposition, PZT could be sputtered onto copper foil after molding. Alternatively, PZT could be sputtered onto flat copper pieces which can then be bent and molded,

depending on the compliance of the PZT. This kind of freedom would be ideal for designing form-fitting transducers.

As far back as 1997, the deposition of PZT onto base metal electrodes (BMEs), such as copper and nickel, has been suggested for the purpose of creating thin film MLCCs. [18, 19] The worldwide production of MLCC capacitors in 2000 was 550 billion pieces. [20] Today, 95% of MLCCs are produced on BMEs. [21] MLCCs on BMEs have largely replaced large Ta capacitors, allowing manufacturers to embed high capacity capacitors directly on circuit boards and microchips. [5] MLCCs are fabricated by interleaving electrodes and high-ε_r dielectrics, such as mixtures of $BaTiO_3$ and other dielectrics. [22] Thin film MLCCs face an uphill battle to compete with traditional MLCCs in terms of price mainly because of the cost and time associated with depositing so many layers of material. [5] However, thin film MLCCs are excellent candidates for high frequency applications due to their small profiles and high quality. Controlling the quality of the interface to ensure high resistivity and low leakage as well as improving the reliability are several challenges faced by thin film MLCCs. [5, 21]

1.1 Project objectives

i. Achieve good quality PZT sputtered directly on copper foil substrates

ii. Characterize the PZT films in terms of their microstructure and electrical properties.

iii. Examine the effect of the Cu substrates on the extrinsic contributions to the polarization.

iv. Model, and then fabricate and test sputtered PZT/Cu cantilever energy harvesters.

2. Ferroelectricity and piezoelectricity

2.1 Ferroelectricity

The anomalous dielectric properties of what are known as ferroelectrics have been investigated since the discovery of piezoelectricity in Rochelle salt in 1880 by the brothers Curie. [23] The first known perovskite ($CaTiO_3$-like, ABO_3) ferroelectric, barium titanate ($BaTiO_3$, BT), was investigated first around 1940 by Wainer and Salomon at the National Lead Company. [24] Research into solid solutions of perovskite $PbZrO_3$ (PZ) and $PbTiO_3$ (PT) began in earnest in the 1950s, soon finding use in many products.

The reader will no doubt recognize the analogy to ferromagnetism, though most ferroelectrics have little to nothing to do with iron. Ferromagnetism pertains to the alignment of electron spin, and ferroelectricity to the alignment of electric dipoles. There are some other similarities in how such materials can be viewed but the most important are the division of crystals into domains and the hysteresis of electric or magnetic polarization under applied fields. An excellent comparison of these two phenomena is given in. [25]

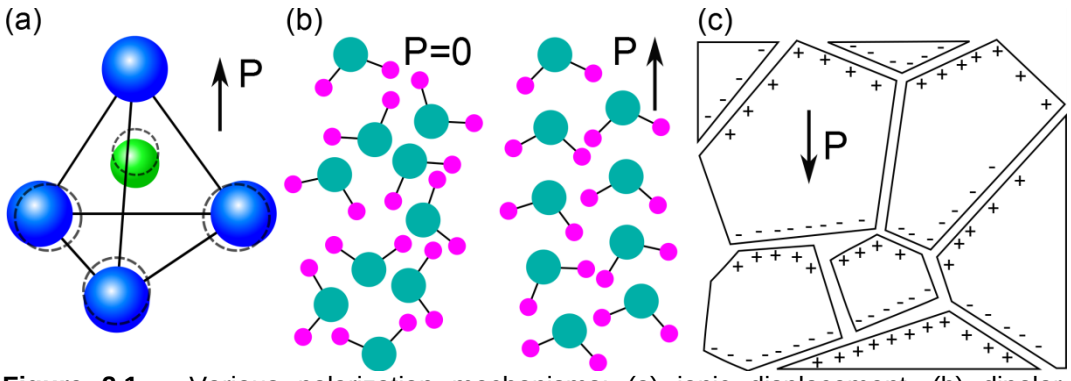

Figure 2.1 – Various polarization mechanisms; (a) ionic displacement, (b) dipolar realignment and (c) space charge segregation.

A dielectric medium is one that can experience an electric polarization throughout the bulk made up of microscopic electric dipole moments. These dipoles can be in the form of ionic displacements, dipolar reorientation, space charge segregation or otherwise (Fig. 2.1). All dielectrics exhibit some kind of polarization response to an applied electric field but usually it is a linear one to a first order approximation. Ferroelectric crystals, on the other hand, are made up of spontaneously polarized regions called domains. Ferroelectrics exhibit a complicated non-linear, hysteretic response to an applied electric field, due largely to this domain structure, and so they are termed non-linear dielectrics.

2.1.1 Dielectrics

In Fig. 2.2, a parallel plate capacitor is illustrated. A linear dielectric material responding to an electric field applied across parallel conducting plates, $\mathbf{E_0}$, develops a uniform polarization **P**. The net effect of the polarization is a bound

surface charge, σ_b, which is equivalent to the magnitude of the polarization, $|\mathbf{P}|$, in this simple case.

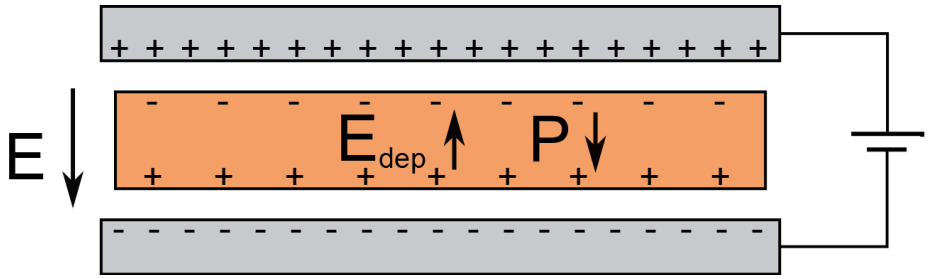

Figure 2.2 – Parallel plate capacitor.

There is also a resulting depolarizing field, $\mathbf{E_{dep}}$, which partially cancels the applied electric field giving a net field inside the dielectric.

$$\mathbf{E} = (\mathbf{E_0} - \mathbf{E_{dep}}) \qquad \text{Equation 2.1}$$

To a good approximation, σ_b and **P** are proportional to the applied field according to the dielectric susceptibility, χ_e. We can let the dielectric be isotropic and so χ_e is a scalar quantity. The dielectric permittivity, ε, is also defined in terms of the susceptibility. The permittivity of free space, or vacuum, is ε_0. Thus the permittivity and susceptibility are equivalent concepts and they are related to each other and to the polarization of the material through Eqns. 2.2(a) and 2.2(b).

$$\varepsilon = \varepsilon_0(1+\chi_e) \qquad \text{Equation 2.2(a)}$$

$$\mathbf{P} = \chi_e \varepsilon_0 \mathbf{E}$$ Equation 2.2(b)

The magnitude of the bound charge can be had from the conservation of electric flux, **D**, across both electrode/dielectric interfaces. **D** is defined by applying Maxwell's equations to an array of finite dipoles.

$$\mathbf{D} = \varepsilon \mathbf{E} + \mathbf{P}$$ Equation 2.3

And from the proportionality assumed for **P** the electric flux and the equivalence of σ_b and P, σ_b is found easily.

$$\mathbf{D} = \varepsilon \mathbf{E_0} = Q / A$$ Equation 2.4

$$\sigma_b = \frac{Q}{A}(1 - \frac{1}{\varepsilon_r})$$ Equation 2.5

$$\varepsilon_r = \frac{\varepsilon}{\varepsilon_0}$$ Equation 2.6

Here, ε_r is the relative permittivity, or dielectric constant. It is a very important parameter for characterizing any dielectric, linear or non-linear. It is directly related to the bound surface charge and therefore the ease with which the work of charge segregation can be performed in a capacitor, for instance.

Figure 2.3 – Simplistic equivalent circuit of a real capacitor.

A real dielectric, however, exhibits electronic behavior similar to an LCR circuit where a resistor represents dielectric loss due to conduction and a capacitor represents charge polarization. The most basic electronic representation is shown in Fig. 2.3. Dielectrics also have a certain inductance associated with them due to the flow of current through space charge and free carriers due to defects associated with vacancies. The motion of space charge or ionic defects, most obvious in low frequency alternating fields, also contributes to the inductance.

Dielectric loss is related to the motion of charge by conduction mechanisms present in real dielectric. Charged defects allow for ionic conduction, while pinholes (in a thin film) or second phases growing in grain boundaries may provide a route for Ohmic conduction. The loss spectrum in the frequency domain can be rather constant or it can be a broad peak about a natural frequency, known as a relaxation. These relaxations are generally attributed to the presence of space charge in voids and grain boundaries in the film.

2.1.2 Perovskite structure

Lead zirconate titanate (PZT) is a solid solution of $PbTiO_3$ and $PbZrO_3$ with the Perovskite structure and having anomalously high dielectric constant and piezoelectric coefficients. It has found the most widespread use of any ferroelectric and competes with $BaTiO_3$ as the most researched ferroelectric material.

The ideal perovskite structure, with the formula ABO_3, is a simple cubic lattice with space group $Pm\bar{3}m$. It can be drawn, with face centered oxygen sites forming octahedra occupied by the B atoms, which therefore have 6 nearest neighbors (Fig. 2.4). The A atoms have 12 nearest neighbors and occupy the corners of the unit cell.

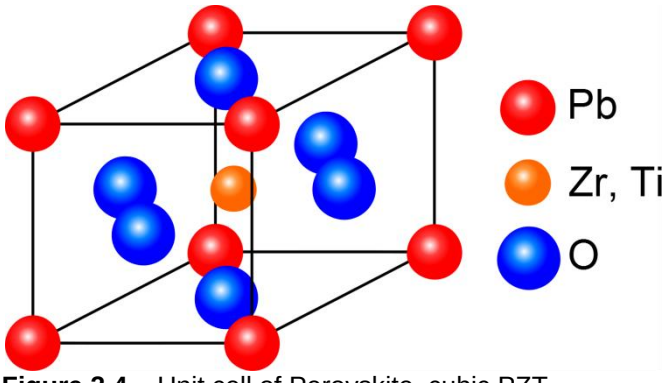

Figure 2.4 – Unit cell of Perovskite, cubic PZT.

The Goldschmidt criterion can be used to assess the perovskite structure given the ionic radii of the constituent atoms is given below. The Shannon radii for Pb^{2+}, Ti^{4+}, Zr^{4+} and O^{2-} are 1.49 Å, 0.605 Å, 0.72 Å and 1.4 Å, respectively.

$$t = \frac{r_A + r_O}{\sqrt{2}(r_B + r_O)}$$ Equation 2.7

In a stable compound the tolerance factor $t \approx 1$, but a polar distortion develops when $t > 1$, indicating that the B atom resting in the octahedron is too small. This is the situation that allows for the long range order associated with ferroelectrics. Conversely, when t < 1 the A atom is too small and so prefers a reduction from from the usual 12-fold coordination. In this case, oxygen octahedron rotate to accommodate the lower coordination and Glazer tilting occurs. [25] This is the situation that occurs in anti-ferroelectrics, where there is short range order, but in the absence of an applied field the macroscopic polarization is zero. Using the Shannon radii above gives the *t* values for $PbTiO_3$ and $PbZrO_3$ as 1.02 and 0.963, respectively, indicating that $PbTiO_3$ is likely to be ferroelectric and $PbZrO_3$ is likely to be anti-ferroelectric – and we know this is the case.

Above the Curie point for bulk $PbTiO_3$, at about 485°C, $PbTiO_3$ exists as a paraelectric, cubic perovskite. [26] Below 485°C $PbTiO_3$ distorts to a tetragonal $P4mm$ space group. The Curie point for $PbZrO_3$ is about 230°C, above which it is paraelectric and below which it is orthorhombic with a $Pbam$ space group.

$Pb(Zr_xTi_{1-x})O_3$ where 95<x<55 are rhombohedral, with R3c (low temperature) and R3m (high temperature) space groups. [27, 28]

2.1.3 The morphotropic phase boundary (MPB)

It has long been known that both the dielectric and piezoelectric properties of the solid solution $Pb(Zr_xTi_{1-x})O_3$ reach a strong maximum in a very narrow range of compositions around x = 0.52 known as the morphotropic phase boundary (MPB). This is the case for thin films as well. [29] There are several theories that attempt to explain the existence of the MPB.

The theory was first put forth by Noheda that the enhanced dielectric and piezoelectric properties of $Pb(Zr_{0.52}Ti_{0.48})O_3$ are due to the presence of a metastable monoclinic phase previously unnoticed in the binary phase diagram that exists in a slim area around the MPB. [30] The presence of this reduced symmetry phase allows for a rotation of the polarization vectors present in the tetragonal or rhombohedral unit cells into the metastable monoclinic phase with only a very small energy barrier. [31] Soon after this, a predominantly monoclinic phase was discovered in the <001> poled lead zinc niobate-lead titanate, PZN-PT, system and so it seems that, in fact, this type of transition may not be a special case at all, but only the tip of the iceberg. [32]

This discovery actually fits nicely with the long held theory that the enhanced ferroelectric and piezoelectric properties at the MPB were due to the abundance of avenues for domain growth due to the combination of rhombohedral and tetragonal phases. The tetragonal phase has six possible directions for domain wall motion, while the rhombohedral has eight. Therefore a combination of these gives fourteen different avenues for domain growth. That these two phases are possibly able to transform into each other through a metastable state increases the likelihood for domain growth and domain wall motion.

2.1.4 Lattice polarization

The enhanced polarization in ferroelectrics is owed to the stability of a reduced symmetry polar ferroelectric phase below the Curie temperature. Above the Curie point, PZT forms a centrosymmetric paraelectric phase where it exhibits no spontaneous polarization. The Curie point can be thought of as the point where any further decrease in the temperature causes the frequency of certain vibrational modes to approach zero. The dielectric constants usually have quite strong temperature dependence, peaking very near the Curie temperature and then rapidly dropping, as the crystal becomes paraelectric. A sketch showing the rough temperature dependence for the dielectric constant of PZT is shown Fig. 2.5.

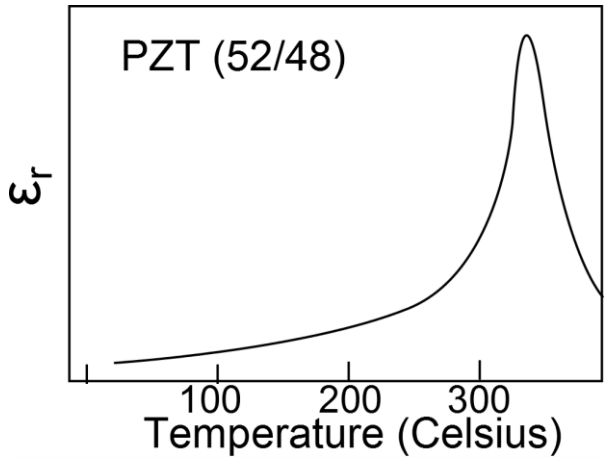

Figure 2.5 – Typical dependence on temperature of the relative permittivity of a ferroelectric.

This behavior is often fit using the Curie-Weiss law, shown below, where *A* is a fitting parameter, T is the temperature and θ_c is the Curie temperature.

$$\varepsilon = \frac{A}{T - \theta_c} \qquad \text{Equation 2.8}$$

In the case of perovskites the tendency to polarize spontaneously is due to a compromise between Coulombic forces, which favor long range ordering, and the electron density, which is more spherical and has lower energy in the centrosymmetric phase. [25] The stabilization of the ferroelectric phase is a second order Jahn-Teller effect. In $PbTiO_3$ there are two second order effects due to the ligand field stabilization of the Ti^{4+} ion as well as the hybridization of a lone pair that forms an asymmetrical covalent bond between Pb^{2+} and two neighboring oxygen anions. [33] This covalent bonding is said to be responsible for the stabilization of the tetragonal phase as well as account for the fact that

$PbTiO_3$ has a much higher dielectric constant than $BaTiO_3$, where the Ba-O bonding is strictly ionic. These are the driving forces for ordering and thus polarization in ferroelectrics.

2.1.5 Ferroelectric domains

As was previously mentioned, an analogy can be drawn between ferroelectricity and ferromagnetism by looking at two key features of both otherwise completely different phenomena. These are the division of a ferroelectric or ferromagnetic crystal into electrically or magnetically polarized domains and the hysteresis observed in the macroscopic polarization under large electric and magnetic fields.

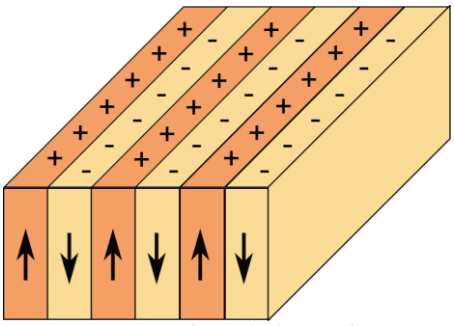

Figure 2.6 – Domains of alternating polarization in a single crystal.

Ferroelectric crystals are split into domains whose spontaneous polarization vectors are oriented in different (but complimentary) directions (Fig. 2.6). Within a

domain the lattice points are all subjected to the same distortion. Defects and other mechanical boundary conditions aside, the equilibrium size of domains are governed by two competing factors. On the one hand there is a cascade effect whereby the strain of the lattice at a domain boundary induces a dipole in the next site which results in a strain on that site. And on the other hand surface charges eventually form a large depolarization field with high associated energy. In order to minimize the depolarization field, domains may be twinned into adjacent domains of opposite polarity. These are known as 180° domain walls. The 180° domain boundaries have a very low energy because the lattice distortion is the same and only the direction of polarization is different.

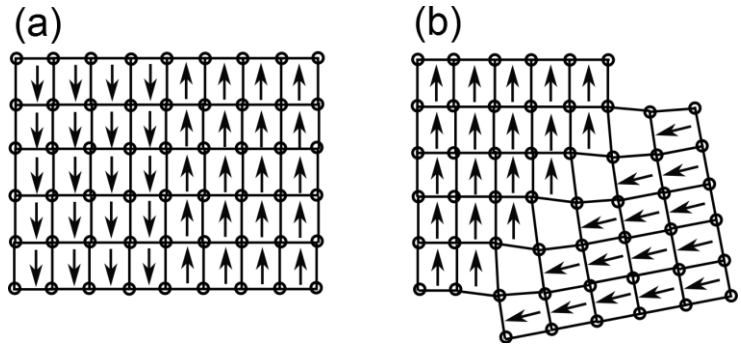

Figure 2.7 – (a) A 180° domain wall and a (b) 90° domain wall.

As polycrystalline ceramics are cooled below the Curie point, domains will nucleate at several places in the crystallite, which may be oriented along different polar axes. Thus, the 180° and 90° domain walls in Fig. 2.7 may form in the tetragonal phase and 71°, 90° and 109° domain walls may form in the

rhombohedral phase. Polycrystalline ceramics, and thin films in particular, can be subjected to very high mechanical stresses which can increase the formation of non-180° domain walls.

The measurement of dielectric and piezoelectric properties will depend strongly on the anisotropy of the film, which comes about naturally as a result of thin film processing. The the measurement axis is perpendicular to the plane of the film and is known as the 3 (or *z*) direction. The 1 (or *x*) and 2 (or *y*) directions lie in the plane of the film. Films often are subjected to biaxial stress due to the processing conditions and nucleation of crystallites often occurs at the film-substrate interface. In light of this, properties should are often the same along the 1 and 2 directions, but different along the 3 direction. In thin film samples the *c*-domains are those whose *c*-axes are aligned to the 3 (or z) axis (Fig. 2.8). Domains where the *c*-axis of the unit cell lies in the plane of the film are known as *a*-domains.

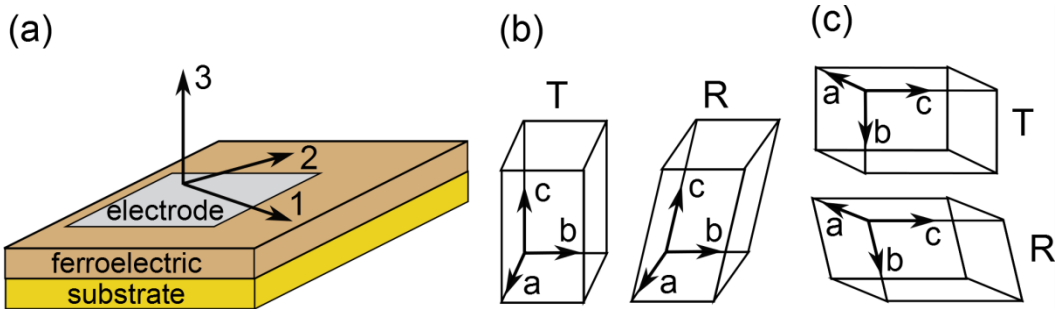

Figure 2.8 – (a) The coordinate system chosen for the device, (b) unit cells in *c*-domain orientation relative to the substrate in (a) and (c) unit cells in *a*-domain orientation relative to the substrate in (a).

The dielectric constant and loss of ferroelectric thin films are typically measured at sub-switching fields (<20 kV/cm), but typically around 1 kV/cm and a frequency of 1 kHz. This field is not strong enough to cause domain reversal. In films which are primarily *a*-domain, the dielectric constant is found to be much higher than in films which are primarily *c*-domain. In the *a*-domains the atoms are relatively free to oscillate with a small field perpendicular to the strain state associated with the domain. The applied field is so weak that there is not enough energy required to change the lattice structure as in the case of 180° switching of *c*-domains.

In contrast, poled ceramics or textured films which contain primarily *c*-domains tend to exhibit a larger polarization in the high field regime. Since there is no strain associated with 180° domain switching, it takes less energy to switch *c*-domains and they can therefore switch at lower field strengths.

2.1.6 Domain switching

The ferroelectric hysteresis behavior can be explained by the motion of domain boundaries and nucleation of new domains in the ferroelectric crystal, which is decidedly nonlinear due to the differences between the boundary conditions (i.e. stress, defects, and geometry) on various domains. As well there are linear regions to the hysteresis loops under various field strength regimes. A typical hysteresis loop is shown in Fig. 2.9(a).

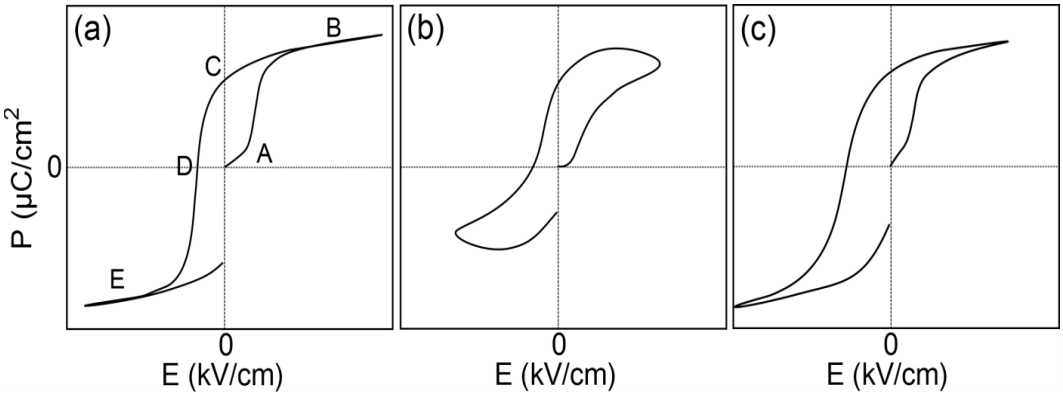

Figure 2.9 – (a) A typical, hysteresis loop, (b) a very lossy hysteresis loop possibly caused by the presence of ionic or electronic defects and (c) a hysteresis loop shifted along the abscissa by an internal bias field.

Under small fields (less than ~1 kV/cm) the polarization induced is small and roughly linear to point A, and is due mostly to the polarization of atoms in *a*-domains. The rate of polarization change with applied field increases until reaching the positive coercive field (E_c) where domain wall motion becomes important (section AB). The ease with which new domains are nucleated and grow is indicated by the steepness of the sides of the loop as well as the strength of E_c. The presence of charged defects has been known to pin domain boundaries, reducing the extent to which switching can occur. At strong fields (B) the ferroelectric reaches saturation as all of the domains that can be switched already have been and the response becomes linear.

As the applied field begins to sweep in the reverse direction, some of the domains reverse due to a depolarizing field until zero field strength, at C, where what remains is called the remanent polarization (P_r). At a zero field the

electrodes are shorted, however there are always uncompensated charges at the electrode-ferroelectric interface due to dead or reacted interlayers which contribute to the depolarizing field. Unequal distributions of charge in the voids and grain boundaries can also contribute to this. The sweep continues in the reverse direction until the net polarization becomes zero at the negative E_c at point D and finally saturates in the reverse polarization at point E.

The polarization is reorientable, meaning that if an applied field switches some fraction of the domains “up” then a field applied in the reverse direction can switch them back down. Although films may eventually become fatigued they can be switched thousands or millions of cycles without losing their ability to reorient.

Qualitative information concerning the dielectric loss of the film can be gained by analyzing the shape of the hysteresis loops. Electrically lossy films have wide loops, humps, and never completely saturate as the depolarizing field becomes excessively strong, such as the loop in Fig. 2.9(b). Furthermore, films with space charge can give erroneously high values to the polarization as the charge being displaced is not related to the polarization of domains but to the displacement of said space charge. A loop shifted along the abscissa, shown in Fig. 2.9(c), indicates the presence of an internal field brought about by charged defects in the film, possibly at the substrate interface. [34] This phenomenon is known as self-polarization.

2.1.7 Mechanisms of domain switching

The accepted approach toward domain reversal studies in bulk ceramics is based on what is called the Kolmogorov-Avrami-Ishibashi (KAI) model. In this model reversed domain nucleation occurs and is then grown out sideways. The fractions of domains polarized in the direction of the field is represented by the following formula where *p* is the fraction of the ferroelectric reversed, *t* is the time and t_0 and *n* are parameters which include the geometry of the nuclei, the domain boundary mobility and the electric field.

$$p(t) = 1 - e^{-(t/t_0)^n}$$ Equation 2.9

However, there is a problem in that the KAI model failed to predict the correct fraction of the ferroelectric reversed in the first tens to several hundred nanoseconds after application of the applied electric field. A solution was proposed by researchers who studied the polarization between small (15 μm x 15 μm) electrodes on a timescale of 8 decades beginning from 10 ns after the application of the field. It was found that the switching characteristics are more typical of an array of very small ferroelectric elements which are switched independently of each other with each element possessing a unique switching probability. [35] This was interesting in that it lends a physical interpretation to the stochastic theory of domain switching, where a ferroelectric is comprised of a set of domains with a distribution of switching fields. Other researchers have shown,

however, that there is cooperative motion between domains separated by microns. [36]

2.1.8 Rayleigh analysis

It has been demonstrated that the low amplitude AC field dependence of the dielectric constant is due to reversible domain wall motion. This is thought to result from domain wall motion through a random, spatially distributed electrical or mechanical energy potential. [37] The potential is widely thought to be heavily dependent on defects, such as $V_O^{\bullet\bullet}$, which act like energy barriers to domain wall motion, pinning the domains and preventing their movement if the electric field is not strong enough to overcome them. [38] An example of the potential energy landscape and physical picture representing such point defects is given in Fig. 2.10. Aside from the dielectric constant, the piezoelectric constants and the elastic compliance have also been shown to obey a Rayleigh law under applied stress. [39-42]

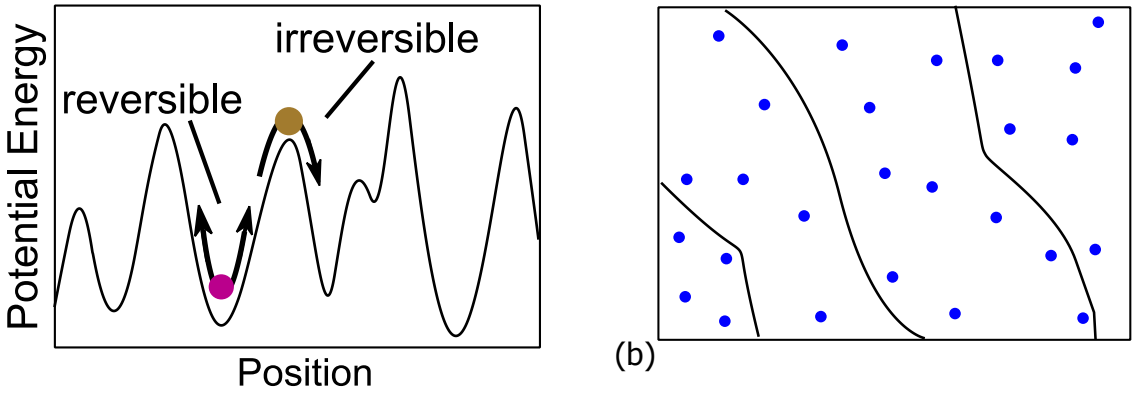

Figure 2.10 – (a) Potential energy barriers and (b) physical landscape of defects pinning domains.

The motion of the domains in response to an applied field is thought to be restricted by defects such as electronic point defects, dislocations, rhombohedral-tetragonal interfaces, substrate clamping and an internal electric field. [41, 43] It was also proposed that large internal stresses that result in a decrease of the domain wall mobility in the tetragonal phase provide less of an obstacle for the 109° and 71° domain walls in the rhombohedral phase. [44] At the same time, the additional directions available for domain reorientation in MPB compositions enhance the Rayleigh response above that expected for purely rhombohedral or tetragonal compositions. [42]

The phenomenon is nearly linear in the regime where the AC field amplitude, E_0, is less than one half of E_c ($E_0<1/2E_c$). The dependence of the electric displacement on the electric field in this regime is given by Eqn. 2.10. The relative permittivity is given by ($\varepsilon'_{init} + \alpha_{irr}E_0$), which is a linear function of E_0. [45]

$$D(E) = \varepsilon_0(\varepsilon'_{init} + \alpha_{irr}E_0)E \pm \frac{\alpha}{2}(E_0^2 + E^2) \quad \text{Equation 2.10}$$

where E is the instantaneous electric field and α_{irr} is the Rayleigh parameter. The plot of ε'_{irr}-E_0 shows some hysteresis due to losses associated with the pinning and unpinning of domain walls. According to Rayleigh theory these should be proportional to α_{irr} according to Eqn. 2.11. Therefore plotting the real and imaginary parts of the dielectric constant against each other yields a straight line of slope 4/3π. [40, 41, 45]

$$\varepsilon'' = \frac{4\alpha_{irr}}{3\pi} \quad \text{Equation 2.11}$$

This relationship applies to ferroelectrics in general, and is independent of material. However, an exception has been reported for hard, or acceptor doped, PZT. The acceptor doping causes the material to exhibit a quadratic dependence of ε'_{irr} on E_0. [37, 41, 46] In this case the plot ε'_{irr}-ε'_{irr} still gives a straight line, but the slope is different. It was then postulated that the nonlinear contribution must be due to a lossless reversible process. [45]

The Rayleigh parameter, α_{irr}, accounts for irreversible domain wall motion. The value ε'_{init} is actually a combination of the intrinsic dielectric constant and reversible domain wall motion

$$\varepsilon'_{init} = \varepsilon'_{intr} + \varepsilon'_{rev} \quad \text{Equation 2.12}$$

where ε'_{intr} is the intrinsic dielectric constant due to the polarization associated with cationic displacement and ε'_{rev} is the contribution due to reversible domain wall motion. [42] Thus, the dielectric constant can actually be thought to consist of three parts. The intrinsic component can be diminished by large internal fields negating the applied field and cation loss or substitution which reduces the number of dipoles contributing to the dielectric displacement. The reversible and irreversible contributions can both be reduced by such things as the electronic point defects, stress, and internal fields, as described above. The difference between the reversible and irreversible contributions is mainly due to their field dependence. The reversible component will have weak or no field dependence whereas the irreversible component will have strong field dependence, which can be quantified by the Rayleigh parameter.

Rayleigh coefficients for several thin film materials are given in Table 2.1. It should be noted that most of the films for which Rayleigh data are reported are fairly thick (≈1μm). This is because the Rayleigh parameter tends to drop dramatically below this thickness. [36] The behavior has been shown to be enhanced by a cooperative interaction between domain walls acting on the scale of microns, which may account for the observed thickness dependence. This also implies that this is a long-range effect capable of transgressing across grain boundaries. [36, 39]

Table 2.1 – Rayleigh coefficients for various thin films.

	Thickness (nm)	α_{irr} (cm/kV)	ε'_{init}	$\alpha_{irr}/\varepsilon'_{init}$ (cm/kV)
$PbTiO_3$(101) and (111) [47]	260	2.9	340	0.0096
(45/55) PZT(111) [37]	1440	13	1340	0.0097
(52/48 PZT(100) [37]	900	38.2	1288	0.03
(52/48) PZT(111) [37]	900	28.2	1097	0.026
PMN-PT(100) [37]	1000	61.5	2060	0.03
PMN-PT(111) [37]	600	40.2	1746	0.023
PZT polycrystalline [48]	1870	900	35.4	0.039

2.1.9 First order reversal curves (FORCs)

FORCs are a subset of the Preisach formalism used to describe hysteretic effects in general. Preisach's formalism has been used extensively in the study of magnetic materials and has recently been used to characterize ferroelectric hysteresis. The ferroelectric is modeled as a distribution of bistable units, individually called hysterons, which each behave as a two-state switch. It should be noted that the hysterons do not have any physical representation outside of this distribution, i.e. they are not necessarily ferroelectric domains. However, the model may describe the pinning of ferroelectric domains by stress or internal field, where the domains are assumed to respond to a field by a stochastic process such as the Barkhausen jumps that occur in magnetic media. [49] The hysterons have a distribution of switching fields, and they make up the ferroelectric ensemble. When the system is at saturation, all of the hysterons are

said to be switched up or down, depending on the polarity of the applied field. The macroscopic polarization is given by Eqn. 2.13. Here, $q(\alpha,\beta)$ is either -1 or +1 depending on the switching history, $\rho(\alpha,\beta)$ is the irreversible Preisach distribution, $\rho_{rev}(\alpha)$ is the reversible distribution, and α and β are the ascending and descending field strengths, respectively.

$$P = \iint_{\alpha>\beta} q(\alpha,\beta)\rho(\alpha,\beta)d\alpha d\beta + \int_{\alpha_{min}}^{\alpha_{max}} k(\alpha)\rho_{rev}(\alpha)d\alpha \qquad \text{Equation 2.13}$$

The interesting parameters are the distribution functions, $\rho(\alpha,\beta)$ and $\rho_{rev}(\alpha)$, which describe the switching behavior of the ferroelectric. These are defined by Eqns. 2.14-2.15.

$$\rho(\alpha,\beta) = \frac{1}{2}\frac{\partial^2 P(\alpha,\beta)}{\partial\alpha\partial\beta} \qquad \text{Equation 2.14}$$

$$\rho_{rev}(\alpha) = \lim_{\beta\to\alpha-}\frac{1}{2}\frac{\partial P(\alpha,\beta)}{\partial\beta} \qquad \text{Equation 2.15}$$

Although founded on mathematics, it lends itself to a very simple geometric interpretation. The triangle in Fig. 2.11 describes the half-plane defined by α and β. When the ferroelectric is negatively saturated, the triangle appears as Fig. 2.11(a), where all of the hysterons are negatively poled. After increasing the field, α, a horizontal line divides the half-plane. Now decreasing the field β adds a link to the dividing line, see Fig. 2.11(b). The top area represents the negative switched hysterons and the bottom area represents the positive switched

hysterons. With knowledge of the distribution functions, therefore, we can know the polarization for any arbitrary field history applied after either negative or positive saturation, in theory. [50]

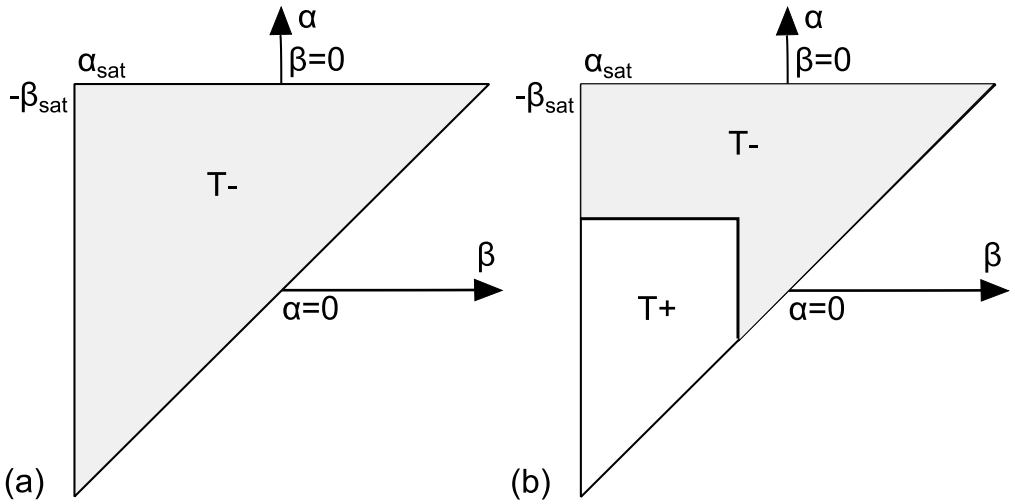

Figure 2.11 – (a) Negatively saturated Preisach half-plane and (b) Preisach half-plane after increasing the field and then decreasing it again.

In practice, there are several conditions that the FORCs must satisfy in order for the Preisach analysis to strictly apply. These are the wiping out and congruency properties. [51] The wiping out property states that extrema of the applied field wipes out the history of any smaller variations in the field. The congruency property states that all back and forth half loops between two local extrema are congruent. Often, ferroelectrics do not satisfy these preconditions and for this reason, the experimentally obtained distributions are known as FORC, and not Preisach, distributions. [48] This research is further limited by the lack of a Preisach-based phenomenological analysis which could relate the polarization

and internal field to the experimentally obtained FORCs. [51] Such a model would have applications in the fields of ferroelectrics and magnetostrictive materials.

Although FORCs are presently limited, they are nonetheless useful in characterizing the hysteresis behavior of ferroelectrics. For instance, there are differences in the FORC distributions of virgin and fatigued ferroelectric films. [52, 53] Asymmetry in $\rho(\alpha,\beta)$ across the line α=0 indicates an offset in switching fields. This may be due to trapped charges at an electrode interface, which causes an internal bias field. Mechanical clamping may also contribute to an offset in the switching field for domains near the interface relative to those at the surface of the film. [53] A model was proposed utilizing a Preisach type formalism to describe the quadratic dependence of the piezoelectric coefficient on applied stress. [54] This showed that the analysis could be applicable to piezoelectricity as well as polarization hysteresis.

2.2 Piezoelectricity

Electrostriction is the strain proportional to the square of an applied field, which occurs in all dielectrics. On the contrary, piezoelectrics have a linear strain response to an applied field, to a first order approximation. Piezoelectric materials also exhibit the reverse effect whereby the application of a compressive or tensile stress results in the development of an electric field across the sample.

The internal field developed as a result of applied stress is known as the direct effect and the strain response to an applied field is known as the indirect effect. [26] These are illustrated in Fig. 2.12.

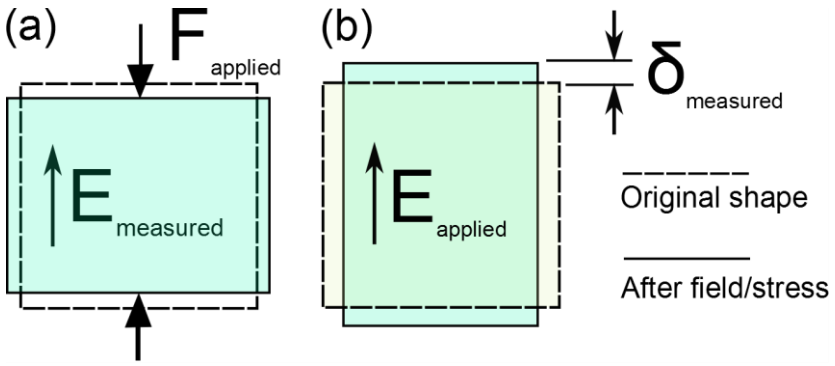

Figure 2.12 – (a) The direct piezoelectric effect and (b) the indirect piezoelectric effect.

Piezoelectricity is a property of 20 of the 21 non-centrosymmetric crystal point groups. The other 11 crystal classes do possess a center of symmetry and do not exhibit the piezoelectric effect. All ferroelectrics are also piezoelectric, although the reverse is not true. There are materials, ZnO and AlN for example, which are piezoelectric but do not exhibit a reorientable spontaneous polarization.

2.2.1 Thermodynamic derivation of piezoelectric coefficients

The Gibbs free energy of a piezoelectric system is illustrative of the relationship between the strain (x_{ij}), stress (σ_{ij}), electric displacement (D_i) and field (E_i). Here it is assumed an elastic dielectric material subjected to a small perturbation of the mechanical stress and electrical field with the temperature kept constant (allowing the entropy term to go to zero). The isothermal Gibbs energy can be written several ways, depending on the choice of independent variables. In the two forms given below, dG_σ uses σ_{ij} and E_i as the independent variables and dG_x uses x_{ij} and E_i. A third and fourth equation exist using the electric displacement.

$$dG_\sigma = -x_{ij}d\sigma_{ij} - D_i dE_i \qquad \text{Equation 2.16}$$

$$dG_x = -\sigma_{ij}dxi_j - D_i dE_i \qquad \text{Equation 2.17}$$

This is interesting because in order to achieve equilibrium, the system will always attempt to minimize its free energy. It can be seen by integrating Eqns. 2.16 and 2.17 that under equilibrium conditions ($\Delta G = 0$) an increase in the magnitude of the applied electric field (ΔE) will be accompanied by an increase in the magnitude of σ_{ij} or x_{ij}, respectively.

$$x_{ij}\Delta\sigma_{ij} = -D_i\Delta E_i \qquad \text{Equation 2.18}$$

$$\sigma_{ij}\Delta x_{ij} = -D_i\Delta E_i \qquad \text{Equation 2.19}$$

The total differentials for x_{ij} and D_i, with respect to the independent variables σ_{ij} and E_i in dG_σ, explicitly define the piezoelectric field-strain constant (d_{ijk}, m/V or C/N), elastic compliance (s_{ijkl}, units of m^2/N) and dielectric permittivity at constant strain (ε_{ij}, C^2/Nm^2 or F/m). The constitutive equations for the isothermal piezoelectric system are obtained by integrating the differential and substituting constants for the partial derivatives (a good approximation as long as fields and stresses are not too great).

$$dx_{ij} = \left(\frac{\partial x_{ij}}{\partial \sigma_{kl}}\right)_E d\sigma_{ij} + \left(\frac{\partial x_{ij}}{\partial E_k}\right)_\sigma dE_k \xrightarrow[substitution]{integration} x_{ij} = s^E_{ijkl}\sigma_{kl} + d^\sigma_{kij}E_k \qquad \text{Equation 2.20}$$

$$dD_i = \left(\frac{\partial D_i}{\partial \sigma_{jk}}\right)_E d\sigma_{ij} + \left(\frac{\partial D_i}{\partial E_j}\right)_\sigma dE_j \xrightarrow[substitution]{integration} D_i = d^E_{ijk}\sigma_{jk} + \varepsilon^\sigma_{ij}E_j \qquad \text{Equation 2.21}$$

Likewise, the total differentials for σ_{ij} and D_i, with respect to the independent variables x_{ij} and E_i in dG_σ, explicitly define the piezoelectric field-stress constant (e_{ijk}, C/m^2 or N/Vm), elastic stiffness (c_{ijkl}, N/m^2) and dielectric permittivity at constant stress (ε_{ij}, C^2/Nm^2 or F/m).

$$d\sigma_{ij} = \left(\frac{\partial \sigma_{ij}}{\partial x_{kl}}\right)_E dx_{ij} + \left(\frac{\partial \sigma_{ij}}{\partial E_k}\right)_x dE_k \xrightarrow[substitution]{integration} \sigma_{ij} = c^E_{ijkl}x_{kl} + e^x_{kij}E_k \qquad \text{Equation 2.22}$$

$$dD_i = \left(\frac{\partial D_i}{\partial x_{jk}}\right)_E dx_{ij} + \left(\frac{\partial D_i}{\partial E_j}\right)_x dE_j \xrightarrow[substitution]{integration} D_i = e^E_{ijk}x_{jk} + \varepsilon^x_{ij}E_j \qquad \text{Equation 2.23}$$

The σ_{ij} tensor contains 9 components; however symmetry arguments result in a reduction to 6 independent components by contracting the tensor into a pseudo-tensor form. The e_{ijk} and d_{ijk} tensors can correspondingly be contracted into

pseudo tensor form e_{il} such that it has 18 components in a 3x6 matrix rather than 27 in a 3x3x3 matrix.

In the case of thin films with anisotropy only in the direction normal to the substrate (uniaxial anisotropy), as is typically the case except for biaxially textured films, the symmetry reduces to ∞/mm. We can further simplify e_{il} by choosing the equivalent directions 1 and 2 to be in the plane of the film and 3 to be in the measurement direction of applied field, perpendicular to the plane of the film. Analysis of the symmetry can show that only three unique piezoelectric coefficients (d_{31}, d_{33} d_{15} and e_{31}, e_{33}, e_{15}) and six unique compliance/stiffness coefficients (s_{11}, s_{12}, s_{13}, s_{33}, s_{44}, s_{66} and c_{11}, c_{12}, c_{13}, c_{33}, c_{44}, c_{66}) are necessary. The constitutive equations reduce to the following, where d_{ij} and e_{ij} are 3x6 pseudo tensors and s_{ij} and c_{ij} are 6x1 pseudo tensors.

$$x_i = s_{ij}^E \sigma_j + d_{ki}^\sigma E_k \qquad \text{Equation 2.24}$$

$$D_i = d_{ij}^E \sigma_j + \varepsilon_{ij}^\sigma E_j \qquad \text{Equation 2.25}$$

$$\sigma_i = c_{ij}^E x_j + e_{ki}^x E_k \qquad \text{Equation 2.26}$$

$$D_i = e_{ij}^E x_j + \varepsilon_{ij}^x E_j \qquad \text{Equation 2.27}$$

These relations describe the electromechanical coupling of the piezoelectric. Finally, a metric often used to describe the efficiency with which electrical energy

is converted to mechanical and vice versa are the electromechanical coupling coefficients, k_{ij}.

$$k_{ij} = \sqrt{\frac{\text{mechanical energy stored}}{\text{electrical energy applied}}} \quad \text{or} \quad k_{ij} = \sqrt{\frac{\text{electrical energy stored}}{\text{mechanical energy applied}}} \qquad \text{Equation 2.28}$$

2.2.2 Application of the piezoelectric coefficients

The two most important piezoelectric coefficients for thin film applications are d_{31} (e_{31}) and d_{33} (e_{33}). The d_{15} (e_{15}) coefficients describe the shear response to a field or stress, and they are not often used. The difference between the d_{ij} and e_{ij} coefficients is evident from the constitutive relations given above. The d_{ij} describe the strain developed in response to an applied field or the electric flux generated by an applied stress. The e_{ij} describe the stress developed under an applied field or the electric flux corresponding to a state of strain. The choice of whether to use d_{ij} or e_{ij} in an actuator depends on whether it is desired to work with the stress or the strain. Typically, it is desirable to convert the known electric field into a stress, thus the e_{ij} is preferred. For a transducer it depends on whether the measurement is of a stress (use d_{ij}) or a strain (use e_{ij}). For a cantilever energy harvester, usually it is the stress developed in the film which is modeled as a result of the electromechanical coupling of the films and so the d_{ij} is preferred.

For applications such as cantilever energy harvesters and actuators there are two schematics for achieving actuation, each of which actuates one or the other of the piezoelectric coefficients. A simple schematic for cantilever energy harvesters utilizing the d_{33} with interdigitated electrodes is shown in Fig. 2.13(a). The schematic utilizing the d_{31} with parallel plate electrodes is shown in Fig. 2.13(b). The d_{33} coefficient is usually larger than the d_{31} coefficient. However, there is a tradeoff with a smaller effective electrode area in the d_{33} design.

Also, the terms unimorph and bimorph describe asymmetric and symmetric stacks, respectively. In other words, in the unimorph configuration PZT and electrodes are only deposited on one side (PZT/Cu), whereas in a bimorph configuration they are deposited on both sides (PZT/Cu/PZT).

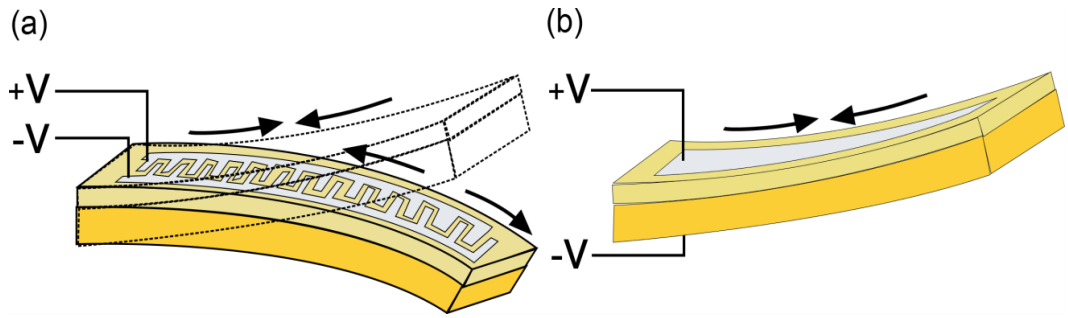

Figure 2.13 – Cantilever energy harvesters utilizing the (a) interdigitated electrode scheme and (b) the parallel plate scheme.

2.2.3 Poling

Poling is the alignment of polarization vectors (domains) in a sample by the application of an electric field at an elevated temperature. This takes place through the nucleation and growth of new, as well as the growth of existing domains. The piezoelectric effect is not observed in un-poled bulk polycrystalline samples due to the isotropic arrangement of the domains. The expansion of one domain cancels out the contraction of another oriented perpendicularly. However, stresses applied during thin film processing can lead to films which are anisotropic and do have an inherent piezoelectric response without poling. Another factor that can lead to anisotropic behavior in films is the self-polarization, whereby an internal bias field originating with an unequal space charge distribution, or a Schottky barrier at the substrate-PZT interface, can actually lead the film to "self-pole" as it cools through the Curie temperature. [34, 55]

In either case, a ceramic can be poled by the application of a sufficiently strong static field. It is usually done midway between room temperature and the Curie temperature. Poling can be used to enhance the piezoelectric effect in a bulk or thin film polycrystalline sample. With varying degrees of success, domains boundaries will move or be created to form domains whose polarization coincides with the applied electric field. Poling can usually cause the 180° domain boundaries, present in a ferroelectric, to coincide with the applied field due to the

absence of mechanical resistance. Poling can also partially align non-collinear domains, although the effect is limited by inter- and intra-granular stresses. Typical poling parameters for PZT are in the range of 40 kV/cm at 150°C and held for around 5 minutes. [26]

2.3 Lead zirconate titanate (PZT) thin films

This section addresses some of the issues that affect the properties of PZT thin films. The structure and composition of PZT thin films will be discussed, largely in the context of sputtered films. The sections immediately afterwards will deal with various complications including the effects of stress induced during processing, defects and conduction mechanisms, electrode yields, and interfacial effects. This section will conclude with a review of recent attempts to deposit PZT and other perovskite ferroelectrics on BMEs. Extra attention will be paid throughout to subjects that are of particular concern to RF magnetron sputtering and crystallization of PZT on BMEs, specifically copper foils.

Much research has been conducted on how to grow single phase PZT without a reduced lead content second phase. It is sometimes called a secondary phase and may be one of several distinct fluorite-like or pyrochlore phases. [56] These can often be seen to form at the air-PZT interface, but can be stable throughout the film if thermodynamic conditions allow it. Films with a pyrochlore phase will have poor characteristics such as reduced dielectric constant and increased

conductivity and dielectric loss. Even if a second phase does not appear, there can be charged $V_{Pb}^{//}$ defects which contribute to dielectric loss as well as decrease of the polarization of the film resulting from the non-equilibrium processing conditions of deposition and crystallization.

2.3.1 Structure and composition - deposition

Sputtering conditions, especially the sputtering pressure, power, and deposition rate have a very pronounced effect on the lead stoichiometry of the as-deposited amorphous film. Basic sputtering theory says that volatile elements have a lower sticking probability than non-volatile elements. [57-59] The ceramic target will also experience some change over time, particularly with regards to the sputtering rate. A long pre-sputtering, possibly for several hours on first use and several minutes on later depositions, is necessary in order to achieve repeatable results. An excess of lead, typically at least 10%, is usually added to the sputtering target mainly to account for lead loss during subsequent crystallization.

When considering the following qualitative arguments and reading through the literature it is important to notice how different every experiment is. For instance, sputtering from a 2.5 cm diameter target at a 3 cm throw distance and 10 mT is not the same as sputtering from a 10 cm target at 3 cm distance and 10 mT. So called “optimal sputtering conditions” are sensitive to many variables.

At high sputtering pressure lead in the film approaches the nominal concentration, that is, the concentration present in the target. At lower pressures (less than about 5 mTorr) the mean free path of incident atoms becomes very long and they have a great propensity to re-sputter lead and the resulting films may be pyrochlore. [60] Some researchers have found that at higher pressures a pyrochlore phase forms, which was attributed to the low surface mobility of the atoms once they have stuck to the substrate, due to losing energy in previous collisions. [61]

A similar idea is in play for the sputtering power. At higher powers more lead may be re-sputtered. However, the deposition rate is also higher and lead can be buried faster within the growing film. In one study, the concentration of lead in the film was found to decrease linearly with increasing power. [62]

2.3.2 Structure and composition - crystallization

Due to the highly reducing atmosphere required to avoid oxidation of a copper substrate, films must be crystallized *ex-situ*, literally meaning “off site.” Films cannot be crystallized during the sputter deposition. Many times PZT films are crystallized *in-situ*, literally “on site,” because it is thought that the films may be crystallized at lower temperatures or obtain better orientation in the case of textured films.

Heterogeneous nucleation of crystallites is presumably favored at the substrate-PZT interface due to the increased number of nucleation sites. Therefore, it is usually expected to see a bottom up growth mechanism. The films are expected to be polycrystalline, since the foil substrate is. Also, it is not likely possible to grow textured PZT on textured copper foils, the lattice parameters of copper (3.61 Å) and cubic PZT (4.04 Å) are much too different. For comparison, PZT films deposited on magnesium oxide (MgO, 4.2 Å), lanthanum nickelate (LNO, 3.84 Å), platinum (Pt, 3.9 Å) and strontium titanate (STO, 3.9 Å) are better matches to the lattice constant of PZT and oriented growth is seen in these cases. Thin films of PZT on polycrystalline or textured copper are expected to be randomly oriented.

The temperatures at which PZT thin films are usually crystallized into the perovskite structure vary from 500°C to 800°C, whereas the bulk crystallization temperature is usually somewhat higher. [63, 64] At lower temperatures a poor dielectric and non-ferroelectric reduced Pb fluorite-like phase tends to form. [65] At higher temperatures the films form many defects due to PbO loss, as well as possibly delaminate from or react with the substrate.

The film can be expected to lose its volatile constituent, lead, at temperatures starting around 400°C. Using higher temperatures aggravates the problem of lead loss can also result in oxygen vacancies, $V_O^{\bullet\bullet}$, especially at low partial

pressures of oxygen which is required in order to prevent oxidation of the copper. [66, 67]

Two major defects in PZT are charge carriers and ionic defects which can become trapped at the electrode interfaces or domain boundaries. The detriment to the properties of the film is two-fold. This charge is free to move around which leads to a conduction mechanism that increases the dielectric loss. Also, vacancies and charge carriers can suppress the polarization by becoming trapped at domain boundaries or at the electrode interfaces.

Oxygen vacancies ($V_O^{\bullet\bullet}$), or the electronic complementary electrons, e^-, and Pb vacancies ($V_{Pb}^{//}$), or the electronic complementary holes, h^+, may become trapped at domain walls, acting as an effective domain pinning mechanism, as in Eqns. 2.29 and 2.30, respectively.

$$O \longrightarrow \frac{1}{2}O_2(g) + V_O^{\bullet\bullet} + 2e^- \qquad \text{Equation 2.29}$$

$$Pb \longrightarrow Pb(g) + V_{Pb}^{//} + 2h^+ \qquad \text{Equation 2.30}$$

When PZT 40/60 films were annealed at 400°C in 1 atm N_2 for 30 min (about $1x10^{-6}$ atm O_2), the films experienced a polarization suppression and the hysteresis loops were shifted along the abscissa. [68] The polarization was restored by a subsequent re-oxidation at 400°C. Furthermore, electronic charge carriers may cause a shifting of the hysteresis loop. [69] The reason is that $V_O^{\bullet\bullet}$ are trapped near the top electrode interface, from which they escaped and

electrons are trapped at the bottom electrode. The internal bias field set up by the trapped defects shifts the hysteresis loop along the abscissa also.

It has been found by careful X-ray diffraction studies that post-crystallization spin coating of a PbO solution deposited layer followed by annealing at or near the crystallization temperature can convert small amounts of pyrochlore to PZT and possibly eradicate some of the $V_O^{\bullet\bullet}$ and $V_{Pb}^{//}$, thereby increasing the P_r and dielectric constant as well as reducing the dielectric loss. [70]

To prevent the formation of pyrochlore, several methods have been explored to rapidly bring the film firmly into the stability region for PZT formation. The usual method is to insert the sample into an open tube furnace after reaching temperature. Rapid thermal annealing (RTA) is one of the most popular alternative methods and involves bringing the sample up to temperature under a quartz lamp in a matter of a few seconds. [71, 72] Others have used laser annealing, which uses very brief laser pulses to heat the film without heating the underlying substrate. [73, 74] This technique has been used to make high quality PZT films on substrates that normally would not be compatible with high temperature processing. Microwave heating has also been explored for its ability to transfer heat very uniformly to the substrate and reduce crystallization times and temperatures. [75]

PZT films are often annealed in air in order to minimize the generation of $V_O^{\bullet\bullet}$ and $V_{Pb}^{//}$. PbO in the amorphous film will volatize at temperatures where the vapor pressure is significant according to the following reaction:

$$2PbO \xrightarrow{vap} 2Pb(g)+O_2(g) \qquad \text{Equation 2.31}$$

Therefore, by supplying excess O_2 the volatilization of lead can be partially mitigated. However, since the copper substrates would oxidize under these conditions it is necessary to crystallize under more reducing atmospheres. It should be mentioned that this is an open system and since there is essentially no lead vapor above the sample the arrow in the above equation only points in one direction, indicating non-equilibrium conditions.

2.3.3 Interface effects

Many researchers have noted a decrease in dielectric properties with decreasing film thickness, where the thickness is still very much more than that at which size effects become theoretically important. Though the causes might be disparate, the most likely common denominator in all of these is the formation of a low-*k* dielectric interfacial dead layer. Three possible contributors to this will be introduced here.

A contiguous low-*k* dielectric dead layer in series with a high-k layer, such as PZT, can be modeled using the formula for series capacitors. Here, *C* is the

measured capacitance and C_h and C_l are the capacitance of the high and low-*k* dielectric layers, respectively. The thicknesses of the layers are d_h and d_l and their relative permittivity are ε_h and ε_l. The result is that the capacitance of the stack is dominated by its lowest capacitance component.

$$\frac{1}{C} = \frac{1}{C_h} + \frac{1}{C_l} = \frac{d_h}{\varepsilon_0 \varepsilon_h A} + \frac{d_l}{\varepsilon_0 \varepsilon_l A} \qquad \text{Equation 2.32}$$

It was mentioned previously that the low-ε_r pyrochlore phase typically forms at the air-PZT interface. The reason for this is that lead leaves first from the surface, while crystallization typically occurs from the substrate-film interface onward. If it is assumed that the thickness of the dead layer is independent of film thickness then the curve *1/C* vs. d_h is a straight line and the dielectric constant of the high-*k* material is easily determined. The ratio d_l/ε_l can be determined by analyzing the slope of the line. [76] If the thickness of the dead layer could be accurately determined from, for instance, a transmission electron microscope (TEM) image or an X-ray photoelectron spectroscopy (XPS) depth profile, then the dielectric constant of the dead layer can be determined.

Another possible source of a low-ε_r dielectric occurs at the substrate-PZT interface. Take, for instance, the reaction between lead and Pt bottom electrodes to form Pb_xPt_{1-x}. This reaction, which readily occurs at the crystallization temperature, will create a dead layer as well as space charge trapped at the interface. [77] In the case of copper, which does not form a solid solution with

lead except at temperatures above 950°C, the important reaction is between diffused oxygen and copper which forms Cu_2O. [78] The dielectric constant of Cu_2O in thin film or bulk form is around 10, about 100 times smaller than thin film PZT. [79] Even if the thickness of the Cu_2O layer were only 10 nm, below a 500 nm thick PZT film, the measured dielectric constant of the film would appear as half of its real value. This illustrates the importance of preventing the oxidation of the copper substrate.

The effects of top electrode material evaporation were studied and the formation of metallic lead at the interface was observed by XPS during deposition. Cu, Pt, and Ag were used and had amounts of metallic lead which increased in that order. [80] During Pt deposition the metallic lead signal increased during deposition, indicating that it was forming a solution with the Pt. During the deposition of Cu and Ag, neither of which form a solution with lead, the signal saturated. The reduction of lead at the interface creates oxygen vacancies at the interface and a low-k interfacial dead layer. [81]

2.3.4 Conduction in PZT thin films

Conduction in an insulator is categorized as extrinsic or intrinsic. Extrinsic AC conductivity refers to the region in temperature where the carrier concentration is fixed and the increased conductivity with temperature is due to increased carrier mobility. Intrinsic conductivity refers to a region where defects are formed at

higher temperatures. The activation energy for the mobile charge carriers responsible for the extrinsic and intrinsic AC conductivity, σ_{AC}, may be fit to an Arrhenius form of Eqns. 2.33 and 2.34, respectively, provided that only a single type of defect is responsible for the conduction. [82, 83]

$$\sigma_{AC}(T) = \frac{\sigma_0}{T}\exp(-\frac{E_A}{k_B T}) \qquad \text{Equation 2.33}$$

$$\sigma_{AC}(T) = \frac{\sigma_0}{T}\exp(-\frac{E_A + \Delta H/2}{k_B T}) \qquad \text{Equation 2.34}$$

Above, E_A and H represent the activation energies and enthalpies associated with the mobility of the defects and the enthalpy required to thermally form defects, respectively. Note that for the intrinsic and extrinsic processes the activation energies will be different, in general.

Additionally, a dielectric relaxation may occur at low frequencies, which manifests as a broad hump in the dielectric loss. A depletion zone width thinner than the film thickness is known to cause a Maxwell-Wagner type relaxation effect. [84] On the other hand, there are Debye relaxations which are known to affect perovskite ferroelectrics, as well. The loss mechanism occurs due to a resonance between space charge in the film and the applied electric field. The center relaxation frequency is temperature dependent and can be fit to an Arrhenius equation of the form

$$\omega(T) = \omega_0 \exp(-\frac{E_A}{k_B T})$$ Equation 2.35

where E_A is the activation energy associated with the dielectric relaxation.

The primary electronic defects in PZT are represented by $V_O^{\bullet\bullet}$ and $V_{Pb}^{//}$, which form traps that influence the AC conductivity and the dielectric loss of the film. Trap levels are defined relative to E_c, E_t, E_v and E_f which are the energy levels of the conduction band, trap, top of the valence band and Fermi level, respectively. Trap levels are denoted (E_t-E_v) Deep traps refer to traps with energy above the Fermi level such that (E_F-E_t)<0 and are attributed to acceptor impurities and $V_{Pb}^{//}$. Shallow traps are traps at or below the Fermi level such that (E_F-E_t)>0, and are attributed to $V_O^{\bullet\bullet}$.

Several mechanisms may dominate the conduction mechanisms in PZT. Poole-Frenkel, Schottky and space charge limited current (SCLC) are thought to play a role in conduction in PZT thin films. [85, 86] Which of these mechanisms dominates depends on the type of defects and their trap levels, defect density, temperature, and the strength of the applied field. [87] Poole-Frenkel conduction is characterized by trap hopping. The defect density is high and conduction is limited by the ratio of the carrier concentration in the bulk to the trap density and level. Schottky conduction, on the other hand, is limited by the injected charge across the electrode-PZT interface.

It has been found that the Poole-Frenkel mechanism is dominant for very thin films or films where the depletion region is on the order of the film thickness, as might be expected for films with a high density of $V_O^{\bullet\bullet}$. [88] Thickness dependence of the leakage current versus applied field is an indication that the conduction mechanism is Poole-Frenkel. It is thought that the Schottky mechanism usually dominates for films greater than approximately 200 nm, where the depletion width is small relative to film thickness, and for fully depleted films. [84, 89] Traps due to defects at the interface can serve as intermediate states between the E_F and E_v, degrading the Schottky barrier height and possibly moving E_F closer to E_c such that Schottky conduction becomes possible at low fields. [90]

In contrast, in SCLC the defect density is low and conduction is limited by a field arising from the segregation of charge in the insulator. [91] The conduction is mainly limited by the ability of charge to leave the insulator. As the trap level increases the ability of the field to segregate charge decreases and the conduction becomes Poole-Frenkel or Schottky. [92]

2.3.5 Stress induced during processing

Films with primarily *a*-domains measured along the 3 direction show higher dielectric constants. This is due to the ability of the atoms to resonate, at small signal oscillating fields, about their equilibrium positions. [93] However, the

piezoelectric coefficient (d_{33}) and P_r will be smaller due to the large electrostatic forces within the domains. Films with primarily *c*-domains will exhibit a larger d_{33} and P_r, although the dielectric constant will be smaller.

The dielectric constant in thin films is usually smaller than that of bulk material. One reason for this is the small grain sizes associated with thin film embodiments. The grain size effect is well studied in bulk ferroelectrics. [94, 95] Stress in the ceramic increases with decreasing grain size according to an inverse power law. [96] According to Devonshire theory an increased stress leads to an increase in the dielectric constant of the ceramic to a point. Too much stress has the opposite effect by suppressing the tetragonality of the crystal structure. As grain size becomes smaller than about a micron, stresses in the film become too large and the dielectric constant falls. [26]

Stresses experienced by the film during heating, crystallization, and cooling can have significant influence on the domain structure of the film. During heating the substrate expands biaxially, putting the PZT film in tension during crystallization. Annealing the substrate at ~600°C during film crystallization can cause the underlying substrate to relax, thereby relieving tension in the film. However, on cooling there will be a large compressive force on the film. A large mismatch of the coefficient of thermal expansion (CTE) between the underlying substrate and film will add significantly to the resulting stress and affect the properties of the film.

An inhomogeneous sample could affect the variation in dielectric response within a sample. If the grain size and stress state are macroscopically inhomogeneous, the film could be undergoing grain growth or stress relaxation during crystallization, which may affect the properties of the film.

Whether or not the film is under tensile or compressive stress as it cools through the Curie temperature determines, to a degree, the preferential alignment of domains. If the film cools past the Curie temperature in tension this favors the formation of *a*-domains, where the polarization and *c*-axes of the unit cells lie in the plane of the film. Further cooling begins to put the films under a large compressive stress. Suppose instead that as the film is at temperature where there is a relaxation of stress, so much so that as the film cools through the Curie temperature it is now in compression. The *c*-domains are now favored, which lie out of the plane of the film. [97, 98]

The thermal residual stress at the interfaces for a composite bilayer with a thermal stress gradient is given by Eqns. 2.36-38. [99]

$$\sigma_{s,surface} = \frac{t_f(t_f^3 E_f - 3t_f t_s^2 E_s - 2t_s^3 E_s)}{t_s(2t_f^3 E_f - 3t_f^2 t_s E_f - t_s^3 E_s)} \sigma_{f,surface} \qquad \text{Equation 2.36}$$

$$\sigma_{s,interface} = \frac{t_f(t_f^3 E_f + 3t_f t_s^2 E_s + 4t_s^3 E_s)}{t_2(2t_f^3 E_f + 3t_f^2 t_s E_f - t_s^3 E_s)} \sigma_{f,surface} \qquad \text{Equation 2.37}$$

$$\sigma_{f,interface} = \frac{(4t_f^3 E_f + 3t_f^2 t_s E_f + t_s^3 E_s)}{(-2t_f^3 E_f - 3t_f^2 t_s E_f + t_s^3 E_s)} \sigma_{f,surface}$$ Equation 2.38

These equations use the subscript *s* and *f* to denote the substrate and film, respectively. The surface stress of the film is assumed to be known, which can be determined from x-ray diffraction residual stress measurements. A simplified equation for the thermal stress of a film crystallized on a dissimilar substrate is given in Eqn. 2.39. [100]

$$\sigma = \frac{E_f}{(1 - v_f)} (\alpha_f - \alpha_s) \Delta T$$ Equation 2.39

Estimates for the elastic modulus of thin film PZT used in the literature vary considerably from 55-100 GPa. [100, 101] As an example calculation, take E_f, v_f, $\alpha_{f,ferro}$, $\alpha_{f,cubic}$, and α_s to be 75 GPa, 0.3, 4x10^{-6} m/m, 6.7x10^{-6}, and 18x10^{-6} m/m, respectively, where the subscripts differentiate between the ferroelectric and cubic, non-ferroelectric thermal expansion coefficients. Then, a ferroelectric film with a Curie point of 400°C crystallized at 650°C would be under 870 MPa of compressive residual thermal stress after cooling to room temperature. Of course, this does not account for the temperature dependence of the thermal expansion coefficients. The elastic moduli depend on method of deposition, defects, orientation, and grain size. [102, 103] For instance, many thin films have nanocrystalline grains. The effect of grain size on the yield stress has been described by the Hall-Petch relationship (Eqn. 2.40)

$$\sigma_Y = \sigma_i + kd^{-n}$$ Equation 2.40

where σ_Y is the yield stress, σ_i is an intrinsic stress independent of the grain size, *k* is a constant, *d* the grain diameter and *n* a constant, often ~0.5. [104]

Values for the thermal expansion coefficient used by several authors for several substrates and for PZT thin films and bulk values are given in Table 2.2.

Table 2.2 – Coefficients of thermal expansion (CTE) for PZT, Cu, Cu_2O, and various other substrate materials.

	CTE (10^{-6} /K)
PZT (polycrystalline)	4.03 [105], 2.0 [99]
PZT (cubic)	6.1 [100], 6.7 [99]
Cu_2O	-0.6 (100˚C) and 0.7 (500˚C) [106]
Copper	18 [107]
Pt	14.2 [105]
Ti	6.5 [105]
SiO_2, thermal oxide	0.4 [105]
Si, single crystal	2.33 [105], 2.6 [99]
MgO, single crystal	8.6 [108]

There have been several reports that residual stresses can cause the film to become rhombohedral, resembling the structure of a Zr-rich PZT composition, in nominally tetragonal, Ti-rich PZT compositions. [109] A study using the local density approximation (LDA) found that the tetragonal to rhombohedral transition

is caused by a compressive stress. [110] The effect was seen in very thin films of PZT (111) fabricated by metal-organic chemical vapor deposition (MOCVD), with the rhombohedral phase present near the film-substrate interface and the free surface tetragonal. [109]

Several authors have also suggested the opposite, that large compressive or tensile biaxial stresses may stabilize the tetragonal phase. This was demonstrated theoretically using the Landau-Devonshire phenomenological theory. [111, 112] Experimentally, epitaxial films with a nominally rhombohedral composition, Zr-rich (70/30) and (80/20) PZT, have been deposited on MgO (001) by pulsed laser deposition (PLD) which show peak splitting associated with co-existing tetragonal and rhombohedral phases. [113] It is clear that the clamped boundary conditions, thermal expansion coefficients, and deposition method (solution, sputtering, PLD, MOCVD, epitaxial or not) all have an effect on the phase ensemble present.

The lattice parameter may be calculated from Bragg's law and the *d*-spacing equations for the relevant unit cell. Bragg's law, shown in Eqn. 2.41, relates the interplanar spacings to the peak position in terms of θ. These are shown in Eqns. 2.42-2.45 for cubic, tetragonal, orthorhombic and rhombohedral, respectively.

$$n\lambda = 2dsin(\theta) \qquad \text{Equation 2.41}$$

$$d_{hkl} = \left[\frac{1}{a^2}(h^2 + k^2 + l^2)\right]^{-1/2}$$ Equation 2.42

$$d_{hkl} = \left[\frac{h^2 + k^2}{a^2} + \frac{l^2}{c^2}\right]^{-1/2}$$ Equation 2.43

$$d_{hkl} = \left[\frac{h^2}{a^2} + \frac{k^2}{b^2} + \frac{l^2}{c^2}\right]^{-1/2}$$ Equation 2.44

$$d_{hkl} = \left[\frac{1}{a^2}\frac{(h^2 + k^2 + l^2)sin^2\alpha + 2(hk + kl + lh)(cos^2\alpha - cos\alpha)}{1 - 2cos^3\alpha + 3cos^2\alpha}\right]^{-\frac{1}{2}}$$ Equation 2.45

These equations can be solved by least squares fitting to several peaks in the observed XRD pattern, using the lattice parameter(s) and/or angle.

One estimate for the average biaxial residual stress in a thin film is commonly called the wafer curvature technique. The residual stress can be estimated by measuring the radius of curvature of the sample and applying Stoney's equation (see Eqn. 2.46), with only a few assumptions regarding the mechanical properties of the materials (Stoney). Here σ is the residual stress of the film, E_{eff} is the effective Young's modulus for the bilayer, d_s is the thickness of the substrate, r is the radius of curvature, and d_p is the thickness of the film.

$$\sigma = \frac{1}{6} E_{eff} \frac{d_s^2}{r d_p (1 - v)}$$ Equation 2.46

We can find E_{eff} by calculating the moment of area for the entire cantilever cross section, accounting for the PZT and the copper foil substrate using estimated values for the Young's modulus of PZT and copper, E_p and E_s. This can be done using Eqn. 2.47.

$$E_{eff} I_{eff} = E_p I_p + E_s I_s$$ Equation 2.47

where I_{eff}, I_p and I_s are the total moment of area, moment of area of the film, and moment of area of the substrate, respectively. However, under the assumption that $d_s >> d_p$, we can simply use the approximation $E_{eff} \approx E_s$. In order for this technique to be valid, the sample must exhibit curvature only about the axis parallel to the short dimension of the plane of the film. If the film exhibits noticeable curvature about the edges then the situation is much more complicated and Stoney's equation does not apply. [114]

Perhaps the most commonly used technique to determine the biaxial residual stress is the $\sin^2\psi$ method using x-ray diffraction. Several scans in 2θ are made at different ψ-tilts. As the angle of penetration becomes smaller the beam samples more in the plane of the film, providing a measurement of the change in the d-spacing with ψ. The angle χ can be used equivalently. The primary advantage of using χ is that the experiment is not restricted to large Bragg angles (2θ >120°, ideally), as is the case when using a ψ-tilt, although the resolution is

better at large Bragg angles. Thus, the χ-tilt method can probe the differences between stress states for many different reflections, giving more information about the anisotropy and stress gradients present in the film. A disadvantage is the additional mechanical complexity and cost of the goniometer stage. Another is the inability to explore negative ψ-tilts, which provide information on the shear stress, since negative and positive χ-tilts are equivalent. [115] The geometry the χ-tilt experiment is shown in Fig. 2.14.

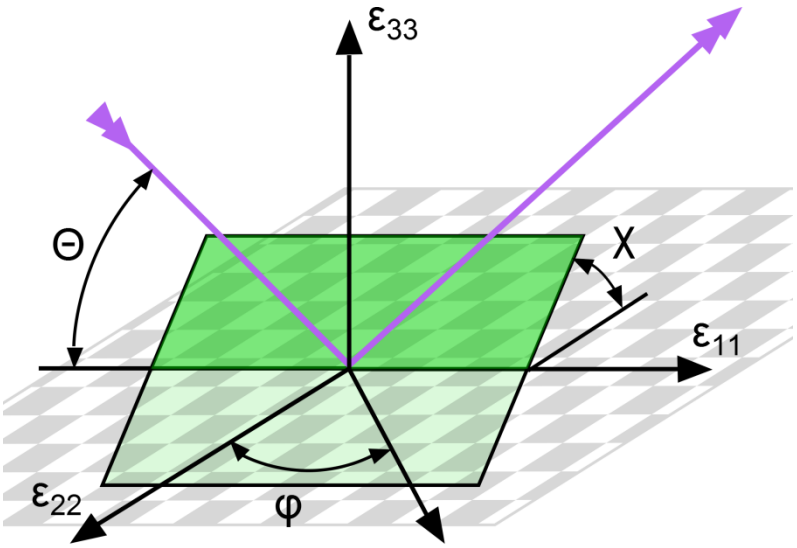

Figure 2.14 – Geometry of the χ-tilt experiment.

In order to use the $\sin^2\chi$ method, the unstrained lattice parameter must be known. Typically, the unstrained lattice parameter is that which was measured at χ=0, but this is only an approximation since the normal stress is most certainly nonzero. [115] Ideally, an unclamped sample exists, in the unstrained state, which can supply an unstrained lattice parameter value, d_0. [116] Another method is to extrapolate the linear fits from two different reflections and use their

intersection as the value for d_0. [117] However, this method can be inaccurate when the film exhibits stress gradients or anisotropy. Usually the lattice parameter given by the pattern at χ=0° is sufficient since the change in lattice parameter due to stress is small compared to the actual lattice parameter.

The analysis of the $\sin^2\chi$ data proceeds as follows, assuming zero shear stress and elastically isotropic grains. [116] Eqn. 2.48 gives the formula that relates the stress at an angle χ to the strained and unstrained lattice parameter. Here the measured d-spacing at the angle χ is d_χ, E is the Young's modulus of the film, and ν is Poisson's ratio of the film.

$$\sigma_\chi = \frac{E}{(1+\nu)}\frac{1}{sin^2\chi}\left(\frac{d_\chi - d_0}{d_0}\right) \qquad \text{Equation 2.48}$$

For a given reflection, the d-spacing in successive scans at different tilt angles, d_χ, is a linear function of $\sin^2\chi$. A linear regression of this plot gives the slope, m, which is given in Eqn. 2.49. The biaxial stress is thus related to m, E, and ν through Eqn. 2.50.

$$m = \frac{(1+\nu)}{E} d_0 \sigma_\chi \qquad \text{Equation 2.49}$$

$$\sigma_\chi = \frac{E}{(1+\nu)}\frac{1}{d_0} m \qquad \text{Equation 2.50}$$

Several issues can impede the analysis of the $\sin^2\chi$ data. The data can be affected by the penetration depth of the x-rays, which is particularly a problem for thick films or bulk samples.

Films with significant shear stresses exhibit ψ-splitting. Stress gradients appear as a parabolic, rather than a linear plot of d vs. $\sin^2\chi$. The situation for textured films is highly ambiguous, since the reflections are not available in the plane of the film and oscillations occur in the plot of d- $\sin^2\chi$. [115] These cases, along with the straightforward linear one, are illustrated in Fig. 2.15.

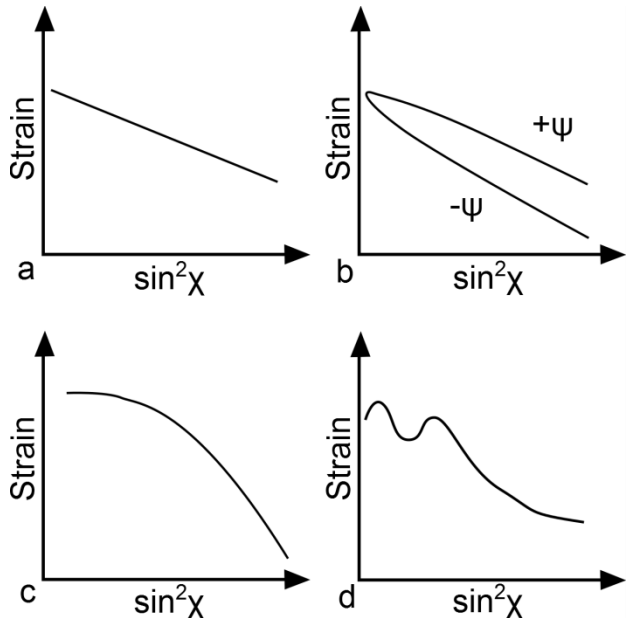

Figure 2.15 – (a) Isotropic strain, (b) *ψ*-splitting from shear stress, (c) strain gradient, and (d) anisotropic or textured film.

A more complicated technique utilizing φ, χ, and ψ together was proposed to maintain a constant sampling volume during the experiment. This method clarifies phase and texture analysis of textured films, and as well the shear stress elements in the film are accessible for full triaxial stress determination. [118, 119] Furthermore, using this method the stress gradient can be determined as a depth profile by applying a Laplace transformation of the polynomial fit to the 2θ-$\sin^2\psi$ relations. [120]

2.3.6 PZT on base metal electrodes (BMEs)

The introductory chapter concludes with a review of recent research into thin films of PZT, particularly of that deposited on base metal electrodes (BMEs). Several papers have been published concerning the reactive sputter and RF hollow cathode plasma jet deposition of PZT onto copper coated polymer films. [11, 12] The films were ferroelectric and switchable by atomic force microscope (AFM) tip; however, these films contained a plethora of second phases.

The most successful attempts have been made using a chemical solution deposition (CSD) route. Several researchers have reported on the CSD of PZT onto electroless nickel foils and electroless nickel coated copper foils. The films were characterized by a reactive interface at the nickel surface and a correspondingly low ε_r around 250 although the loss was around 2 percent. The

cross section of the interface was examined in the TEM and using the formula for series capacitance, the dielectric constant of PZT was estimated to be around 850 and that of the interfacial layer was estimated to be around 10. [121, 122]

Later research used control of the processing parameters to crystallize PZT without oxidizing the copper. It was reported that CSD films obeyed a strict adherence to the thermodynamic equilibrium predicted by the Cu-Cu_2O and PbO-Pb pO_2-temperature (pO_2 – partial pressure of oxygen) phase stability diagram. It was found that even minor excursions from the stability window resulted in large amounts of either pyrochlore at low pO_2 or Cu_2O at high pO_2. [10] However, results published around the same time, which were largely focused on developing a robust CSD route to minimize cracking found that films which were crack free did not form Cu_2O even on excursions to 10^{-6} atm O_2. [9, 123]

3. Experimental

Procedures developed to fabricate $Pb(Zr_{0.52}Ti_{0.48})O_3$ (PZT) thin films on copper foil substrates are described in this chapter. The procedure outline is as follows. Copper foil substrates were prepared by polishing and cleaning. PZT was deposited on the foils by RF magnetron sputtering and then crystallized at low oxygen partial pressures (pO_2), wrapped in a copper envelope. A solution based PbO layer was spin cast on the crystallized films and annealed. Structural characterization was carried out primarily by spectroscopic ellipsometry (SE), x-ray diffraction (XRD), scanning electron microscopy (SEM), and atomic force microscopy (AFM). The ferroelectric and dielectric properties of the samples were characterized by polarization hysteresis measurements and impedance analysis.

3.1 Substrate preparation and electrodes

Prior to deposition, the substrates were polished in order to maximize reproducibility. A high temperature mounting wax was melted onto a glass disc on a hot plate. 100 μm thick copper foils (Sigma Aldrich, 98% complexometric) were laid on the melted wax and covered with filter paper. A second disc was laid on top and the stack was clamped down and cooled until the wax hardened. Once mounted, the foils could be mechanically polished to a mirror finish using 5

μm and 0.3 μm alumina polishing media. The foil was gently removed from the wax and the back wiped clean of excess wax. The polished copper foils were ultrasonically cleaned in isopropyl alcohol before being stored for use. When the alcohol was allowed to dry naturally it was found to leave a residue. For this reason the foils were blown dry with compressed air immediately on removal from the alcohol. The substrates were ultrasonically cleaned again immediately before sputtering.

3.2 RF magnetron sputtering system

The RF magnetron sputtering system was custom built with one inch and two inch sputtering guns operating at 13.56 MHz with a manually controlled impedance matching network (Fig. 3.1). The reflected power is typically less than 1 % of the total power. Argon (99.999%) is used for the sputtering atmosphere. Chamber pressure is recorded with an MKS capacitance manometer. Upstream control is obtained with a mass flow controller (MFC) and downstream control using a manually controlled butterfly valve prior to the turbo molecular pump. Typical sputtering conditions are given in Table 3.1.

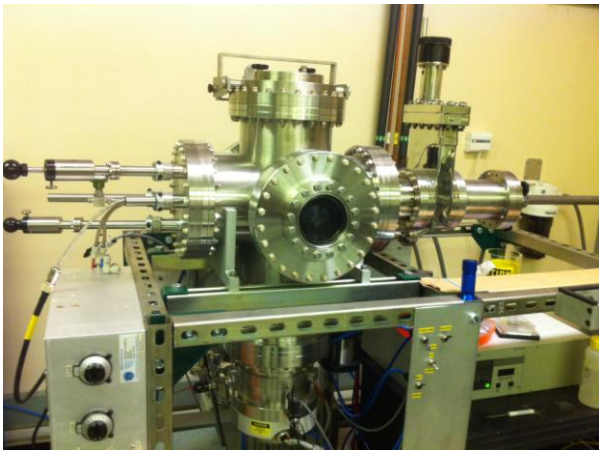

Figure 3.1 – Rf sputtering system. Sample is inserted into the load lock at right. Sputter guns are at left.

Table 3.1 – Typical sputtering conditions.

Sputtering conditions	Typical value
Sputter power density	5 W/cm^2
Ar pressure	30 mTorr
Target-substrate distance	5.5 cm
Target size	2 in
Deposition rate	15 nm/min

Sputtering is an inherently non-equilibrium process. The sputtering yield is defined as the number of sputtered atoms per incident ion. [124] In a compound containing multiple elements or phases, particular elements will have higher sputter yields than others which can influence the final film stoichiometry. In order to control the sputter yield, the target was equilibrated by sputtering for 5 min with the sample blocked. After this initial burn-in the sample was brought in and the

film deposited on it. While this provides an improvement in the compositional homogeneity of the film, the presence of a volatile element such as Pb complicates matters. As the target heats up during sputtering, Pb might volatize from the surface leading to a depth concentration gradient of Pb within the target. With a concentration gradient of Pb, solid state diffusion can deplete the underlying target as Pb atoms diffuse to the depleted surface at elevated temperatures. [124] Although this solid-state diffusion is a slow process, it likely changes in the Pb concentration from sputtered targets over time, and must be kept in mind. Any changes due to this effect will be very unpredictable and depend entirely on the history (number and length of depositions as well as time between depositions) of the target.

Chemical reactions can occur in the film due to the impingement of high-energy atoms and/or ions. Stoichiometry can be affected by the sputtering parameters as well as the history of the target, particularly when one of the components is volatile, as is the case for Pb containing compounds. There can be compositional gradients in sputtered PZT thin films, with the surface often enriched in Pb and the bottom electrode/film interface depleted. [125] There can also be a gradient in the Ti and Zr compositions with the film being depleted in Zr near the surface and near the bottom electrode interface. [126] On the contrary, solution deposited PZT films are more likely to be enriched in Zr near the surface, and enriched in Ti near the film/substrate interface. This was attributed to the relative

rates of decomposition of the Zr and Ti precursors as well as to the lower nucleation barrier of $PbTiO_3$ compared to that of $PbZrO_3$. [56, 127]

3.3 Sputter target preparation

Most of the experiments were completed using a 2 inch, 10% excess PbO sputtering target from Plasmaterials. However, some 1 inch sputtering targets were fabricated to explore variable PbO excess. The 1 inch PZT sputtering targets were produced with a molar excess of 5, 10 or 20 percent excess PbO.

TiO_2, ZrO_2 and PbO powders were weighed and combined with ethanol and milled in a vibratory mill for 6 hours along with YSZ media. The slurry was dried overnight and calcined at 900°C for 2 hours. The calcined PZT was reground to a powder and milled with ethanol and YSZ again and dried to produce fine powders. These powders were pressed into green targets 1 1/8 inches in diameter at 15 ksi for 3 min. The 5%, 10% and 20% targets were sintered in air at 1075°C, 1050°C and 1025°C for 2 hours, respectively.

3.4 Oxygen partial pressure (pO_2) controlled furnace

Films were crystallized in a reducing atmosphere to prevent oxidation of the copper substrate. The furnace (Carbolite) was fitted with a 3.5 inch diameter

quartz tube, which was capped and sealed with custom built fittings and o-rings on both ends. The ends were fitted with gas inlets and outlets. Forming gas (0.1% H_2 balanced with N_2) and UHP N_2 were flowed through a heated water bubbler to control the oxygen partial pressure. Films were placed in an Inconel boat which was hung on an alumina push rod for insertion and quenching. Schematics of the annealing tube and gas flow and control are given in Fig. 3.2.

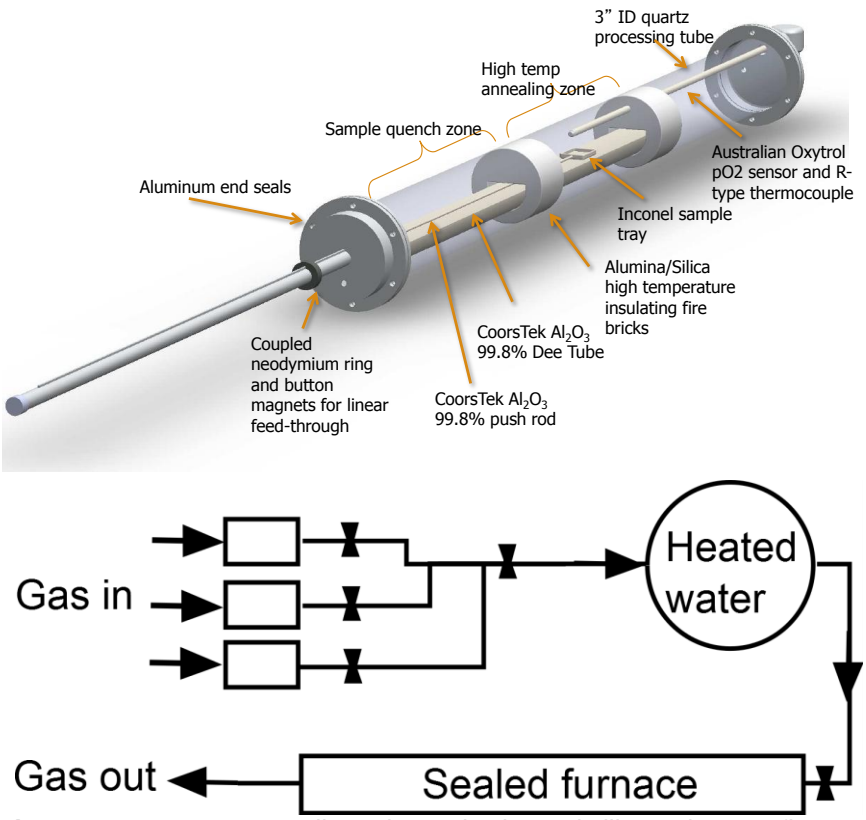

Figure 3.2 – Quartz annealing tube and schematic illustrating gas flow and control. [128]

The atmosphere in the furnace, and thus above the surface of the film, cannot be at equilibrium in terms of Pb vapor and so the system cannot be said to be closed. The film will lose Pb, even in a pure oxygen environment, due to the high vapor pressure of PbO at the crystallization temperature of PZT. Though the furnace is not a closed system, the guiding principle of integrating PZT films with copper foils is that there exists a stability region in pO_2-space where copper does not oxidize but Pb, Zr, and Ti do oxidize. The CuO, Cu_2O and PbO equilibrium curves in pO_2-temperature space are given in Fig. 3.3, with this stability region lying between the Cu_2O and PbO curves. The values of enthalpies and entropies used in these calculations are provided in Table 3.2.

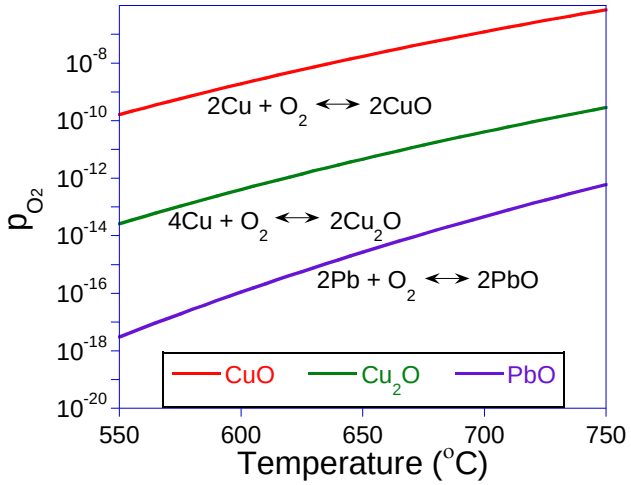

Figure 3.3 – Thermodynamic equilibrium curves for CuO, Cu_2O and PbO in pO_2-temperature space.

Table 3.2 – Standard molar enthalpies, entropies and heat capacities used in equilibrium calculations. Thermodynamic data from Gaskell. [129]

	ΔH° (kJ)	S° (J/K)	C_p (J/K)
Cu (s)	0	33.2	$22.6+6.3x10^{-3}T$
Pb (s)	0	64.	$23.6+9.75x10^{-3}T$
O_2 (g)	0	205	$30.0+4.18x10^{-3}T-1.67x10^{5}T^{-2}$
CuO (s)	-157.3	42.6	$37.5+14.4x10^{-3}T+3.45x10^{6}T^{-2}-1.02x10^{9}T^{-3}$
Cu_2O (s)	168.6	93.1	$62.34+24x10^{-3}T$
PbO (s)	-219	66.5	$37.9+26.8x10^{-3}T$

The pO_2 is measured with a $SIRO_2$ zirconia gas sensor from Australian Oxytrol Systems. Using a forming gas mixture, the pO_2 could be reliably controlled between approximately 10^{-11} and 10^{-20} atm. When using only UHP N_2, the pO_2 could be controlled between approximately 10^{-6} and 10^{-8} atm. The practically achievable range is dictated by the flow range of the MFCs and the concentration of the forming gas. The maximum temperature of the water bath, before condensation in the quartz tube was observed, was 50°C.

Even though the pO_2 was adequately controlled inside the tube, significant problems with oxidation of the substrate were observed, particularly as films became thicker. These problems were solved by wrapping the films in a copper foil envelope prior to crystallization (see Fig. 3.4). Wrapping the film in copper foil effectively shifted the pO_2, inside the wrapper at the exposed film and substrate surface, to the Cu-Cu_2O equilibrium curve if chamber pO_2 was higher than the curve. The reason is that the relatively large interior surface area of the envelope

acts as a sacrificial oxygen getter. Typical crystallization conditions are given in Table 3.3.

Figure 3.4 – Copper foil envelope for crystallizing and annealing PZT thin films on copper foils.

Table 3.3 – Typical crystallization conditions.

Parameter	550°C	650°C	725°C
pO_2	$2x10^{-17}$ atm	$1x10^{-14}$ atm	$5x10^{-13}$ atm
Time	45 min	30 min	15 min

The working principle of the controlled pO_2 furnace is the chemical equilibrium between O_2, H_2 and H_2O.

$$H_2\,(g) + \frac{1}{2}O_2\,(g) \leftrightarrow H_2O\,(g) \qquad \text{Equation 3.1}$$

The chemical equilibrium is defined to be the quotient of the products and reactants, and is only a function of temperature.

$$K_{eq} = \frac{[H_2O]}{[O_2]^{1/2}[H_2]} = \exp(-\frac{\Delta_r G^0}{RT}) \qquad \text{Equation 3.2}$$

where $\Delta_r G^0$ is the standard Gibbs free energy of the reaction, T is the absolute temperature, and R is the gas constant.

The H_2O partial pressure is controlled by the water bath temperature, which can be estimated by the Clausius-Clayperon equation.

$$\frac{dP_{H_2O}}{dT} = \frac{P_{H_2O}\Delta H_v}{T^2 R} \qquad \text{Equation 3.3}$$

where P_{H2O} is the partial pressure of water and ΔH_v is the latent heat of vaporization.

The pO_2 can be therefore be reduced by increasing the partial pressure of hydrogen in the inlet gas. The pO_2 can be increased by increasing the partial pressure of water.

3.5 PbO spin-cast overcoat and anneal

Some of the films were annealed again after applying a spin-cast PbO overcoat in an attempt to reverse some reduction of the film near the surface. [70, 130] In addition to ‘healing’ the PZT film, this procedure was found to be useful for thicker films where substrate oxidation was present. The additional annealing at low pO_2 was helpful in reducing any copper oxide present at the substrate-film

interface while the presence of PbO on the surface prevented the films becoming Pb-deficient.

A quantity of Pb (II) acetate was added to a volume of 2,2 diemethoxyethanol to achieve the desired molarity (up to 0.1 M). The volume was heated at 90°C for several hours to allow the lead acetate to go into solution. The solution was dropped onto the film and spun at 3000 rpm for 30 s. The films were typically annealed at 550~650°C for 20 min, wrapped in a copper foil envelope. These conditions are summarized in Table 3.4.

Table 3.4 – Typical PbO overcoat spin-casting and annealing conditions.

PbO annealing conditions	Typical values
PbO Concentration	0.1 M
Spin rate	3000 rpm
Spin time	30 s
Anneal temperature	650°C
pO_2	$1x10^{-14}$ atm
Time	20 min

3.6 Characterization equipment and methods

Structural characterization by x-ray diffraction (XRD) was carried out on a Bruker AXS D8 Discover x-ray diffractometer using copper K_α radiation. Thickness determination was determined on a J.A. Woollam VASE spectroscopic

ellipsometer (SE) from 700 nm to 1700 nm using a Cauchy model to approximate the optical properties of the PZT thin film. Below 700 nm the films were not well fit by the Cauchy model. Compositional depth profiling of one film was accomplished with X-ray photoelectron spectroscopy (XPS, PHI Quantera Scanning ESCA). .

Surface morphology was studied with scanning electron microscopy (SEM) using an FEI Quanta 600F. Cross sectional SEM was done at CAMCOR, at the University of Oregon, on an FEI Helios dual-beam FIB. The non-conductive surface of the film was sputter coated with either Au-Pd or carbon prior to imaging. Atomic force microscopy (AFM) was done with an Asylum MFP-3D.

Residual stress measurements were carried out using the $\sin^2\psi$ x-ray diffraction method. The results were verified using Stoney's equation to analyze the residual stress by measuring the curvature of a long, narrow PZT/Cu cantilever.

Dielectric measurements were carried out on an HP 4192A low-frequency impedance analyzer using a 50 mV_{rms} test signal. Temperature-dielectric measurements were made on the same, using a hot plate (VWR) as the heat source. Rayleigh measurements were completed on an HP 4284A LCR meter. Rayleigh measurements were performed by an increasing sweep of the test signal level over the first test frequency, then the second frequency, and the third, and so on.

Hysteresis, first order reversal curves (FORCs) and leakage current measurements were done on a Radiant RT66B ferroelectric tester. FORCs were measured from the $-V_{sat}$ condition, i.e. from -500~500 kV/cm, to obtain the ρ^{+}_{FORC} distributions, with a hysteresis frequency of 100 Hz.

4. Properties of sputtered PZT thin films on copper foils

The main goal of this research was to deposit $Pb(Zr_{0.52}Ti_{0.48})O_3$ (PZT) on copper foils without the formation of a Cu_2O interlayer or any other detrimental second phases. Cu_2O has a dielectric constant that is smaller than PZT by two orders of magnitude. A Cu_2O interlayer is effectively a capacitance in series, which lowers the overall capacitance of the device. The large concentration of defects usually present in Cu_2O can also greatly increase the dielectric loss. [106] Fabrication of Cu_2O-free PZT films on copper foils had previously been achieved with solution based techniques. [9, 10] Those authors reported reasonable dielectric constants (~900), low dielectric loss ($\tan\delta<0.05$) and remanent polarizations (P_r) of ~26 $\mu C/cm^2$. Crystallization was carried out at 600-650°C and 10^{-15} atm O_2, with films being built up from layers and crystallized in several steps. There are several advantages to attempting the sputtering technique, some of which were outlined in the introduction.

It proved difficult to produce rf sputtered PZT films on copper foils free of an interfacial layer without wrapping the films in a copper foil envelope during crystallization in a controlled pO_2 tube furnace. Since the properties of films with and without an interfacial layer were very different, it is advantageous to discuss these films separately. The adjustable parameters in each of these two categories were very different, as well. For instance, it is not possible to strictly control the pO_2 environment experienced by films wrapped in the copper

envelope. The envelope is folded and crimped on the edges and corners so that the atmosphere is mostly sealed. What oxygen is able to enter will react (under appropriate thermodynamic conditions) with the large interior surface of the copper envelope, effectively buffering the pO_2 so that it stays in the Cu_2O-PbO stability window near the Cu_2O equilibrium line. This discussion will proceed as follows: first, single layer films sputtered and crystallized under a range of conditions will be discussed; second, two layer films, attempted to prevent the formation of an interfacial layer, will be discussed; and third, PZT/Cu films free of an interfacial layer are discussed.

4.1 Single layer films with interfacial layer

Sputtering is inherently a non-equilibrium process, and there could be both higher oxides and reduced forms of Pb present in the amorphous film which could react with the copper foil substrate. Evidence that suggests this is occurring will be presented. Furthermore, there is some question regarding the nature of the interfacial layer, as to whether it is Cu_2O or Pb. There are overlapping XRD peaks at $2\theta \approx 36.2°$ corresponding to FCC Pb (200) and/or cubic Cu_2O (111). These two subjects are discussed in this section. Cu_2O peaks were indexed according to JCPDS PDF No. 00-005-0667 and tetragonal PZT peaks according to JCPDS PDF No. 00-050-0346. [131, 132]

Films crystallized without the Cu envelope displayed a strong tendency towards an increase in an interfacial layer peak at 2θ=36.2° with increasing film thickness and decreasing crystallization temperature. This behavior is exemplified in Figs. 4.1 and 4.2 where the area under the copper oxide peak, given in units of counts-per-second degrees, is the ordinate. On the other hand, the strength of the observed peak at 36.2° was relatively insensitive to the pO_2 and the sputter power density, illustrated in Fig. 4.3. This relative insensitivity to the pO_2 was also found for solution deposited PZT films on Cu foils. In that work, it was found that Cu_2O-free films could be crystallized in pure N_2 at 650°C, which gives a pO_2 of approximately 10^{-6} atm. [123] Films with similar properties were also crystallized in N_2/H_2 mixtures with a pO_2 of 10^{-15} atm O_2. [10] If the film were reacting with the substrate, it's possible that a thicker film might produce a thicker interfacial layer since there would be more material available to react. In this scenario, copper diffuses through the interlayer to react with the PZT. Also, the change in entropy for the formation of Cu_2O is strongly negative at all temperatures and pO_2 due to the transformation of gaseous oxygen (O_2) to the solid state (Cu_2O). If the PZT were taken as a source of highly mobile atomic oxygen, then at higher temperatures the entropy term in the Gibbs free energy equation becomes strongly positive.

$$\Delta G = \Delta H - T\Delta S \qquad \text{Equation 4.1}$$

Therefore, the Gibb's free energy could become positive, or less negative, at higher temperatures with the implication that a reaction at the interface is less thermodynamically favorable at higher temperatures.

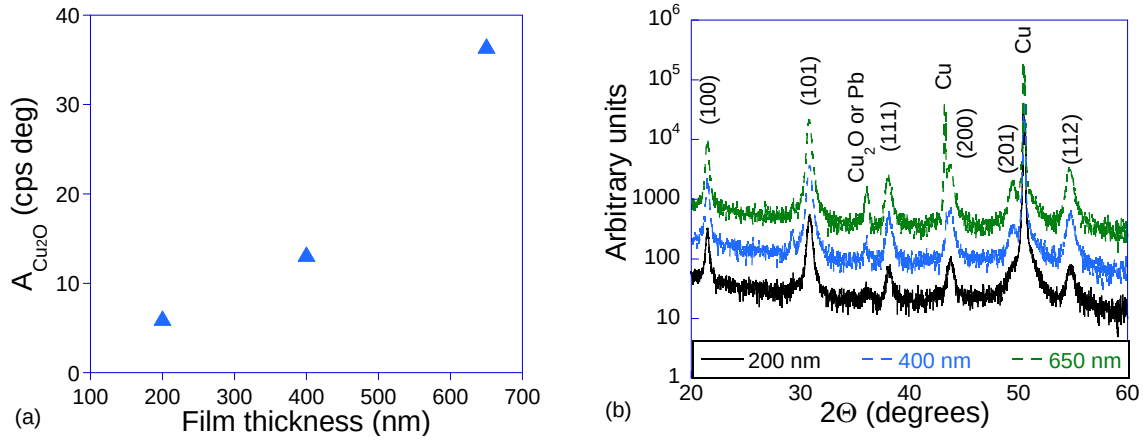

Figure 4.1 – (a) Dependence of peak at 36.2° on thickness for films crystallized at 725°C for 10 min in the thermodynamic stability region and (b) corresponding XRD patterns.

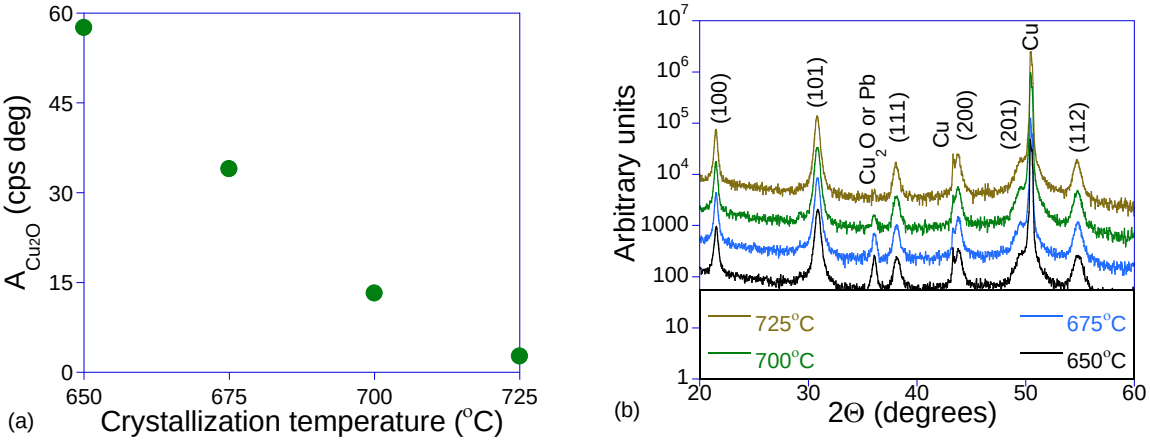

Figure 4.2 – (a) Dependence of integrated peak area at 36.2° on crystallization temperature for 275 nm films crystallized for 10 min in the pO_2 stability region (b) corresponding XRD plots.

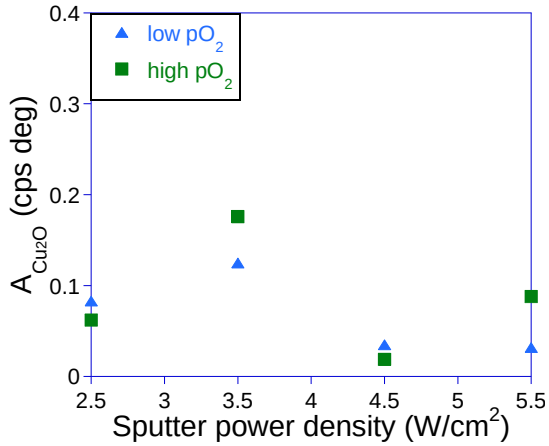

Figure 4.3 – Dependence of integrated peak area at 36.2° on sputter power density. 250 nm films crystallized at 725°C at 10^{-14} atm O_2 (low pO_2) or 10^{-6} atm O_2 (high pO_2).

The presence of this peak at 36.2° is associated with a high dielectric loss, exhibiting hysteresis loops reminiscent of flying lemons or worse; the Starship Enterprise. An exception is that films made from a 5% PbO excess target had poor dielectric and hysteresis properties despite the smaller amount of the interfacial phase indicated by the XRD patterns. It is likely that the loss of Pb from re-sputtering during deposition and vaporization during crystallization precludes using less than a 10% excess PbO target. For this reason all of the other films discussed in this thesis were sputtered from a 10% excess PbO target.

There are two potential explanations for this interfacial layer peak. The XRD peaks for Cu_2O (cubic) and metallic Pb (FCC) are almost overlapping. Some of the conditions under which we observe the peak at 36.2° to increase are

conditions under which we might reasonably expect the possibility of an interfacial layer of Pb to exist. However, there is more evidence to suggest that the peak is in fact a result of the presence of Cu_2O. For instance, in some severely oxidized samples a second peak (2θ=42.3°) matching the Cu_2O pattern, but not that of Pb, was observed (see Fig. 4.4). Rather than forming a mixture of Cu_2O and CuO, at high temperatures the cuprous phase is more stable, especially at low pO_2. [133]

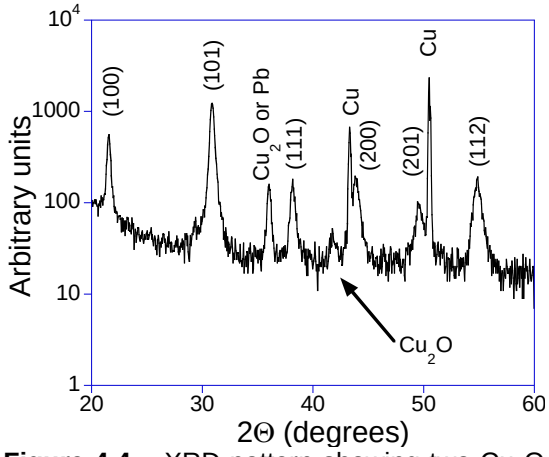

Figure 4.4 – XRD pattern showing two Cu_2O peaks. The film was 650 nm crystallized at 725°C in the stability region.

XPS data for a two layer film (discussed in detail in the next section) provides direct evidence for the presence of oxygen in the copper foil after crystallization. The diffusion of Cu into the PZT film was also noted (see Fig. 4.5).

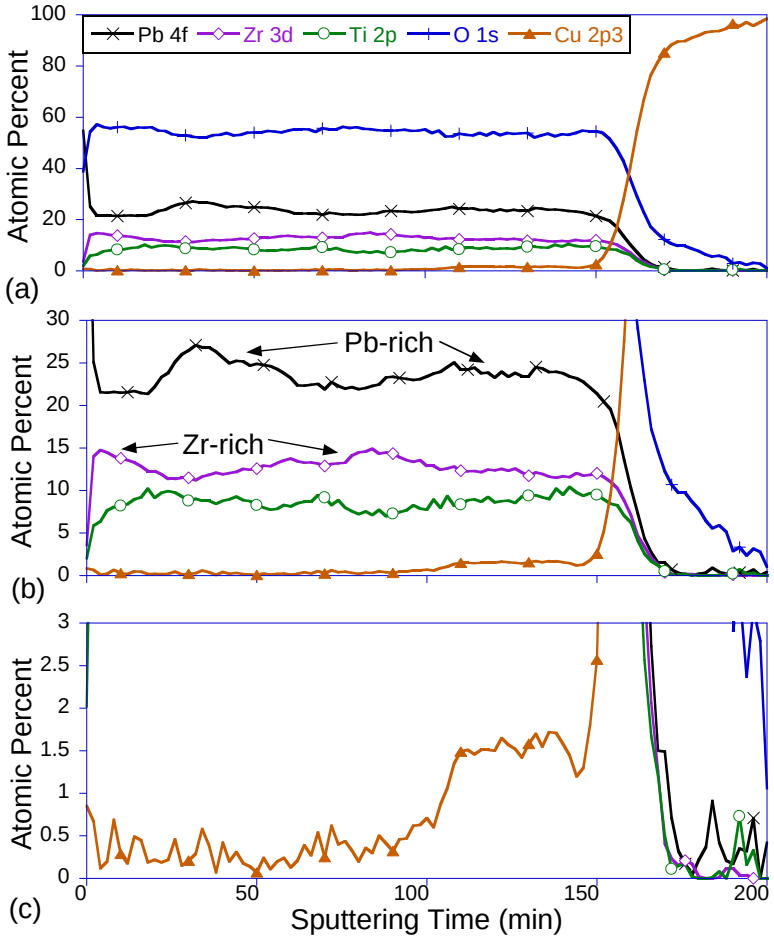

Figure 4.5 – (a) The film appears to be oxygen deficient or Pb is in excess; (b) oxygen diffusion into the copper foil (after 170 min) strongly indicates the presence of Cu_2O; and (c) copper was observed to have diffused a third of the way into the PZT film.

Lastly, a FIB milled cross section of a film with a very large peak at 36.2° was imaged by SEM, definitively revealing a thick interlayer of Cu_2O (when correlated with the XPS data). Elemental mapping was not performed on the interlayer to definitively determine the composition. However, the top surface of the interlayer is parallel to the film, which was deposited on the polished foil (see Fig. 4.6). It appears that the oxidation reaction attacked the copper unevenly. The PZT layer

is characterized by the formation of voids as well as interdiffusion between the foil and film.

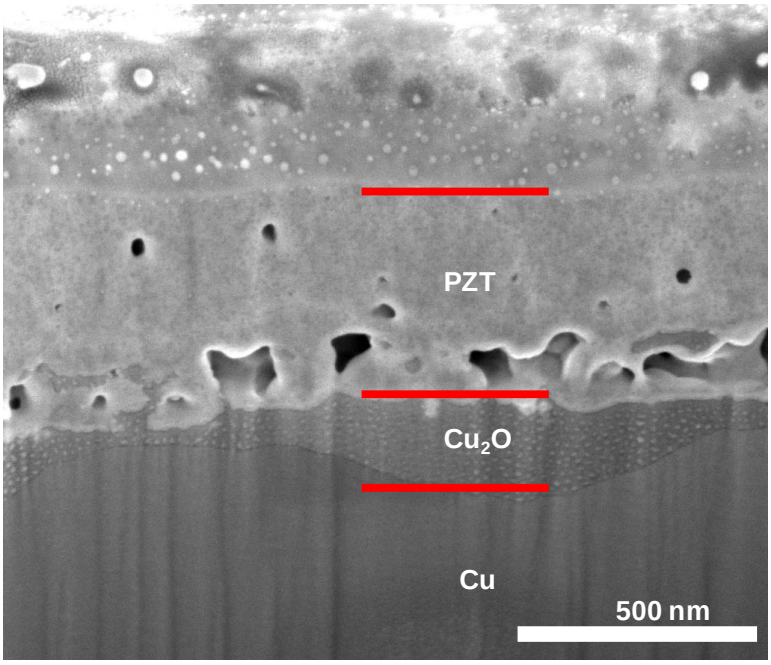

Figure 4.6 – Cross sectional SEM of a 500 nm single layer film crystallized at 725°C in the stability region.

Films sputtered from a 10 percent excess PbO target on polished copper seemed to benefit from a low temperature pre-crystallization heat treatment at 400°C for 20 min in a highly reducing environment (approximately 10^{-27} atm O_2 although the operating temperature of the pO_2 sensor was 550°C). This treatment resulted in reduced height and area of the XRD peak detected at 36.2°. At this low temperature the oxidation of copper should be diffusion limited, and should not occur at such a low pO_2. [134, 135] That said, at temperatures even 25°C higher oxidation occurred at the copper interface, even under highly

reducing atmospheres. This can be compared to the bare copper foil alone which, when exposed to these low temperature and low pO_2 atmospheres never showed any oxidation detectable by XRD. The same sample would consistently show an XRD peak at 36.2° when covered by the amorphous PZT film. One hypothesis for why this low temperature heat treatment was beneficial is that higher oxides of Pb in the sputtered amorphous film were reduced to an equilibrium state, releasing oxygen slowly and thus reducing the propensity for reaction at the interface between the PZT film and copper foil during the subsequent crystallization step. Sputtered PZT films have been known to include a mixture of non-equilibrium oxides of Pb such as PbO_2 or Pb_2O_3. [11, 12] Indeed, the higher oxides of Pb begin to rapidly decompose at around 400°C. [136] In general, PbO content in the film decreases with lower sputter pressure and target-substrate distance and with greater sputter power density. [60, 62, 137] The sputter power density was not found to systematically enhance the interlayer for 250 nm thick films, as described above. However, the peak was always very small for such thin films and there is error associated with calculating the peak area. The XRD peaks attributed to the interlayer were found to be stronger with increasing sputter pressure, which is consistent with increased PbO content in the film. However, if the pressure was reduced to below 30 mTorr there was a substantial fluorite-like phase present and the films displayed very poor electrical properties.

Evidence was presented that suggests increasing oxidation with increasing film thickness and decreasing crystallization temperature. A low temperature reducing heat treatment helped reduce the extent of the oxidation, but even a slightly higher temperature caused the interface to react and form Cu_2O, even under conditions where the bare electrode did not form an oxide. Given this, it is a reasonable hypothesis that the PZT film itself was the source of oxygen that was taken up by the copper foil, resulting in increased Cu_2O formation under the conditions stated above. During oxidation, copper is thought to diffuse towards the surface in a potential field, continuously revealing a fresh surface. [138] If copper was diffusing through a Cu_2O interlayer then a fresh copper surface would be available to react with free oxygen at the interface with the PZT. Therefore, copper is not like some other metals which grow a protective oxide layer. Rather, the reaction is limited only by the diffusion of copper cation up through the interfacial oxide. [106, 139, 140] Thus, the reaction is expected to be limited only by the availability of oxygen. So the thickness of the oxide layer is expected to be a strong function of crystallization time if the source of oxygen were atmospheric, i.e. pO_2. This dependence on the integrated area of the XRD peak at 36.2° was not seen. This provides the basis for consideration of a finite source of oxygen, such as the film, being responsible for oxidation of the substrate.

Since many of the problems discussed in this section were later overcome by using a copper envelope to buffer the pO_2, it is likely that this is a secondary

mechanism for oxidation. The sample insertion step (into the furnace hot zone) provides an opportunity for the film to leave the thermodynamic stability window by exposing the film to the higher pO_2 at equilibrium in the furnace hot zone, while the film and substrate themselves are still comparatively cool. If the oxidation proceeds before the film and substrate can get up to temperature, then opportunity exists for the formation of Cu_2O.

The presence of the second Cu_2O peak in the XRD patterns is highly suggestive that the interfacial layer is Cu_2O. The cross sectional SEM clearly shows an interlayer of 50 - 100 nm in thickness. XPS data in Fig. 4.5 shows oxygen present in the copper substrate, also consistent with the interface being composed of Cu_2O. Furthermore, the Cu_2O peaks present in the XRD patterns of crystallized films increased significantly when O_2 was introduced along with Ar during sputtering. It would be interesting to sputter PZT on oriented copper films or foils. The Cu (111) crystallographic plane is highly insensitive to oxidation. [106, 141] Thus, it's possible that some of the compatibility issues between PZT and copper could be overcome by using such a textured substrate.

Electrical characterization of the unwrapped films with Cu_2O present was performed; however the electrical properties were generally very poor. The hysteresis loops were misshapen in myriad ways, indicating space charge and premature dielectric breakdown, perhaps due to the void structure seen above.

4.2 Double layer films with interfacial layer

The Cu_2O peak detected in the XRD pattern increased with increasing film thickness. A multilayer approach to depositing thicker PZT films via rf sputtering was explored. The rationale was that, if we could not crystallize a thick film without the substrate oxidation reaction occurring, then perhaps we could fabricate the film with an intermediate crystallization step.

In order to minimize the space charge and the associated dielectric loss, two-layer films were formed by depositing a 250 nm layer followed by a 400°C heat treatment and a 5 min anneal at 725°C. A second 250 nm layer was then deposited followed by a 10 min anneal. Annealing was done in the thermodynamic stability window at 10^{-14} atm O_2. A representative XRD pattern is shown in Fig. 4.7.

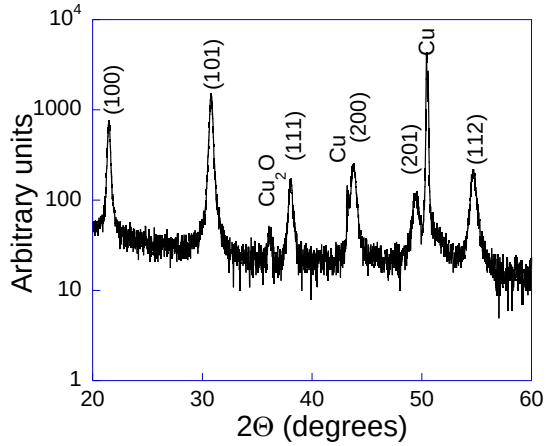

Figure 4.7 – XRD pattern of 500 nm film processed in two layers.

An XPS compositional depth profile for a two-layer film was shown in Fig. 4.5. The XPS data reveals some interesting features. First, oxygen has penetrated into the copper foil, which strongly indicates that the XRD peak at 36.2° is indeed attributable to Cu_2O. Second, XPS results also revealed that copper was diffusing almost a third of the way into the PZT film while maintaining a near constant concentration of 1.5±0.25 at%. It's not well understood what effect a copper dopant would have on the properties of PZT. Cu^{2+} is an acceptor when it substitutes for the B-site Ti^{4+} and Zr^{4+} cations. [142]

Finally, the Zr, Ti, and Pb compositional profiles show some interesting features. The Zr/(Ti+Zr) ratio is increasing towards the surface, and this can be seen in both the first and second layers of the film. Second, the films seem to be Pb deficient at the surface. The apparent Pb concentration spike near the surface in the XPS data is commonly attributed to an artifact of the measurement. [126] The Pb concentration depth profile is similar to what has been reported for DC-pulsed, reactively sputtered PZT films. [143, 144]

The dielectric response and hysteresis for one of these two-layer films are shown in Fig. 4.8. The dielectric loss at the relaxation frequency is still relatively high (7.5%), although much lower than in a film sputtered and annealed as a single layer. The dielectric constant, ~500 at 1 kHz, is lower than reports of solution deposited films of similar thickness on Cu foil (~900 at 1 kHz). It is uncertain what role, if any, the copper impurity identified by the XPS has in these films although

it has apparently saturated in the bottom third of the PZT film. There is clearly still some effect of the space charge reflected in these measurements, as the hysteresis curve appears to be rounding as it returns from saturation.

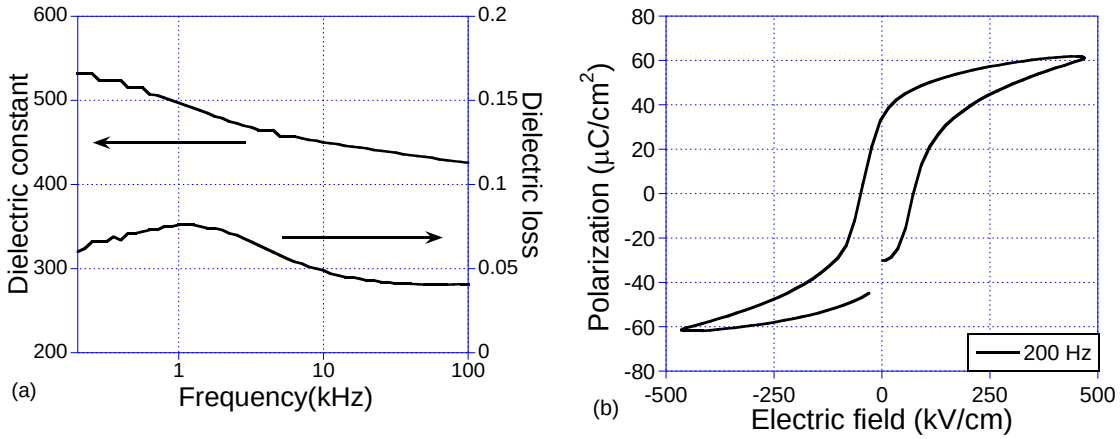

Figure 4.8 – For a 500 nm thick film, processed in two layers: (a) dielectric constant of around 500 and dielectric loss relaxation peak at around 1 kHz and (b) hysteresis.

4.3 Preventing Cu_2O and second phase (fluorite-like) formation

The interfacial Cu_2O layer could be prevented in most cases by wrapping the films in a copper foil envelope during crystallization. Since the envelope is thought to provide a buffer against oxidizing conditions during film heating and cooling (insertion and extraction from the hot zone), the use of this envelope as a tool precludes the thought of altering the pO_2 during crystallization. The pO_2 was thus brought to approximately the equilibrium for Cu_2O formation before the sample was inserted into the hot zone. It is assumed that during crystallization the pO_2 is somewhere in the Cu_2O-PbO stability region. A cross sectional SEM

image shown in Fig. 4.9 indicates the absence of an interfacial layer. A typical XRD pattern showing the Cu_2O-free PZT film is shown in Fig. 4.10.

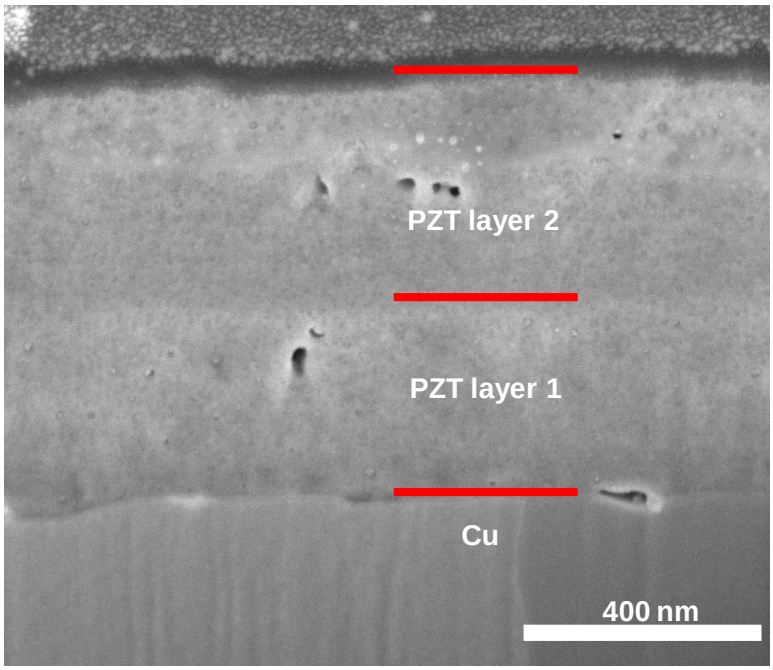

Figure 4.9 – Cross sectional SEM image of a 2-layer, 700 nm thick PZT film. Each layer was crystallized at 650°C for 15 min.

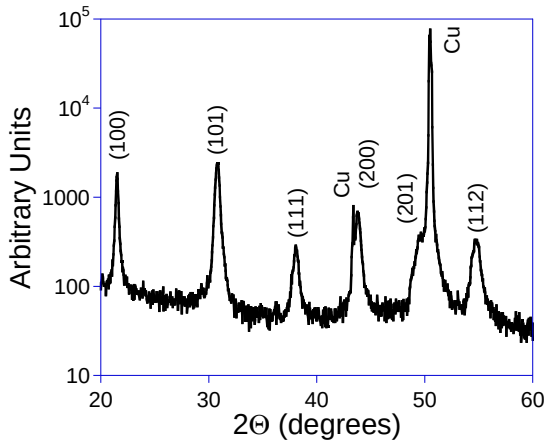

Figure 4.10 – Typical XRD pattern of a 585 nm Cu_2O-free PZT on Cu foil, crystallized at 650°C for 15 min.

Even when wrapping the films in a copper foil envelope during crystallization, in the case of thicker films (> 500 nm) an interfacial layer was occasionally observed. Some examples are given in Fig. 4.11; a 990 nm sputtered film, crystallized at 650°C and 750°C. In the case of the film crystallized at 650°C, a second phase was indicated at 2θ=29.5°, which is recognized to be a fluorite-like Pb-deficient phase. [130] In the case of the film crystallized at 750°C a second phase appeared as a shoulder in the PZT (111) peak and the interfacial layer, with an exceptionally broad peak, appeared at 36.2°.

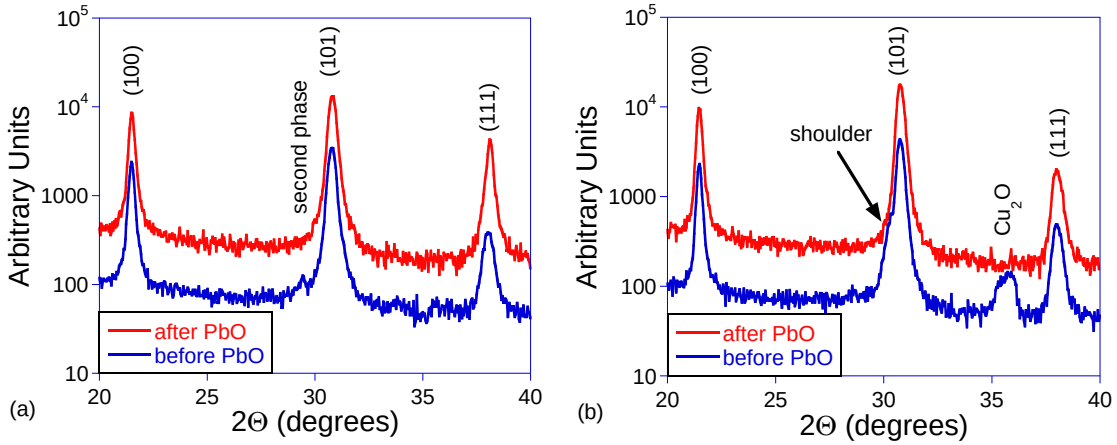

Figure 4.11 – 990 nm films crystallized at (a) 650°C and (b) 750°C and subsequently spin cast with PbO and annealed at 650°C for 20 min.

In the above cases, the Cu_2O interlayer could be removed (as observed by XRD) by one of two methods. First, annealing the film after spin casting a thin solution-based PbO layer resulted in removal of the Cu_2O peaks. [70] Originally this technique was developed to heal a dead layer at the surface of a film by reversing the formation of a fluorite-like second phase. Here the technique

allowed the film to be annealed in a low pO_2 environment while mitigating Pb loss from the surface. Second, annealing the film in a low pO_2, low temperature environment was found to reduce the Cu_2O peaks found by XRD. The temperature had to be kept low enough in order to diminish the extent of Pb loss during the heat treatment. The first method was preferable.

The first method was used to heal the defects seen in the XRD patterns in Fig. 4.11. All of these structural defects were healed, at least to the resolution of the x-ray diffractometer. It is thought that the shoulder was due to a second phase near the film surface which was healed by the PbO. The reduction of the Cu_2O might have been due to additional annealing at reduced pO_2 or it might require on the PbO. Results are inconsistent with simply annealing the film. However, annealing in PbO seems to do the trick every time. For instance, increasing the annealing time from 30 min to 45 min actually resulted in an increase of interfacial Cu_2O. But after treatment with PbO both samples were free of any trace of Cu_2O or second phase in the diffraction pattern.

Above we saw that wrapping the films in a copper envelope greatly reduced the Cu_2O interfacial layer. However, it was also seen that this interfacial layer could reappear in very thick films. In any case, when bare Cu foils were wrapped in the copper envelopes there was never a detectable amount of Cu_2O present after experiencing the same crystallization conditions as a foil with a PZT film. As in the case of the unwrapped films, the introduction of O_2 during sputtering

significantly enhanced the Cu_2O interfacial layer XRD peaks. It was also seen to reappear in films crystallized at low temperatures. An example of such an interfacial layer XRD peak is given in Fig. 4.12. The films were crystallized at 550°C for 45 min, 650°C for 30 min or 725°C for 15 min. The Cu_2O peak was gone after spin casting PbO and annealing, as before. The problem of the substrate oxidizing under thick PZT films or films crystallized at low temperatures has persisted to a small degree, even when the films are wrapped in the copper foil envelope. Fortunately, the technique of spin casting PbO and annealing allows these films to largely recover.

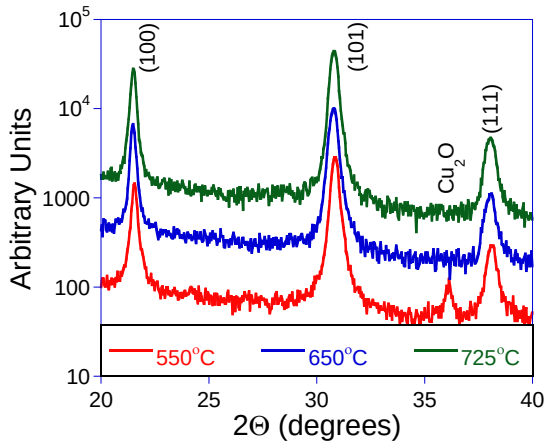

Figure 4.12 – XRD patterns of 585 nm films crystallized at several temperatures.

Occasionally, tiny grains or a second phase appeared on the surface of the film, and was visible in SEM and AFM images. This phase appears as nodules emanating from the grain boundaries. Similar formations have been observed before and were called a fluorite-like or pyrochlore phase due to their

appearance in films derived from 10% PbO excess sol gel solutions, and absence in films from 30% PbO excess sol gel solutions. [127] The fluorite-like phase has been identified with the stoichiometry $Pb_{2+x}Ti_{2-x}O_{7-y}$ and the pyrochlore phase with $PbTi_3O_7$ [56]

Another reason to assert that the nodules are a fluorite-like second phase is what happens when they are heat treated post-crystallization. 350 nm of PZT was sputtered on polished copper foil and crystallized at 650°C for 15 min, wrapped in copper foil. This process was repeated to make a 2-layer film. The post-crystallization heat treatment consisted of either annealing the samples at 400°C in a highly reducing atmosphere for 30 min or spin casting 0.1 M PbO and annealing at 650°C for 30 min in the Cu_2O-PbO stability window. The samples were wrapped in copper foil for both treatments. The results of SEM imaging on these samples are shown in Fig 4.13.

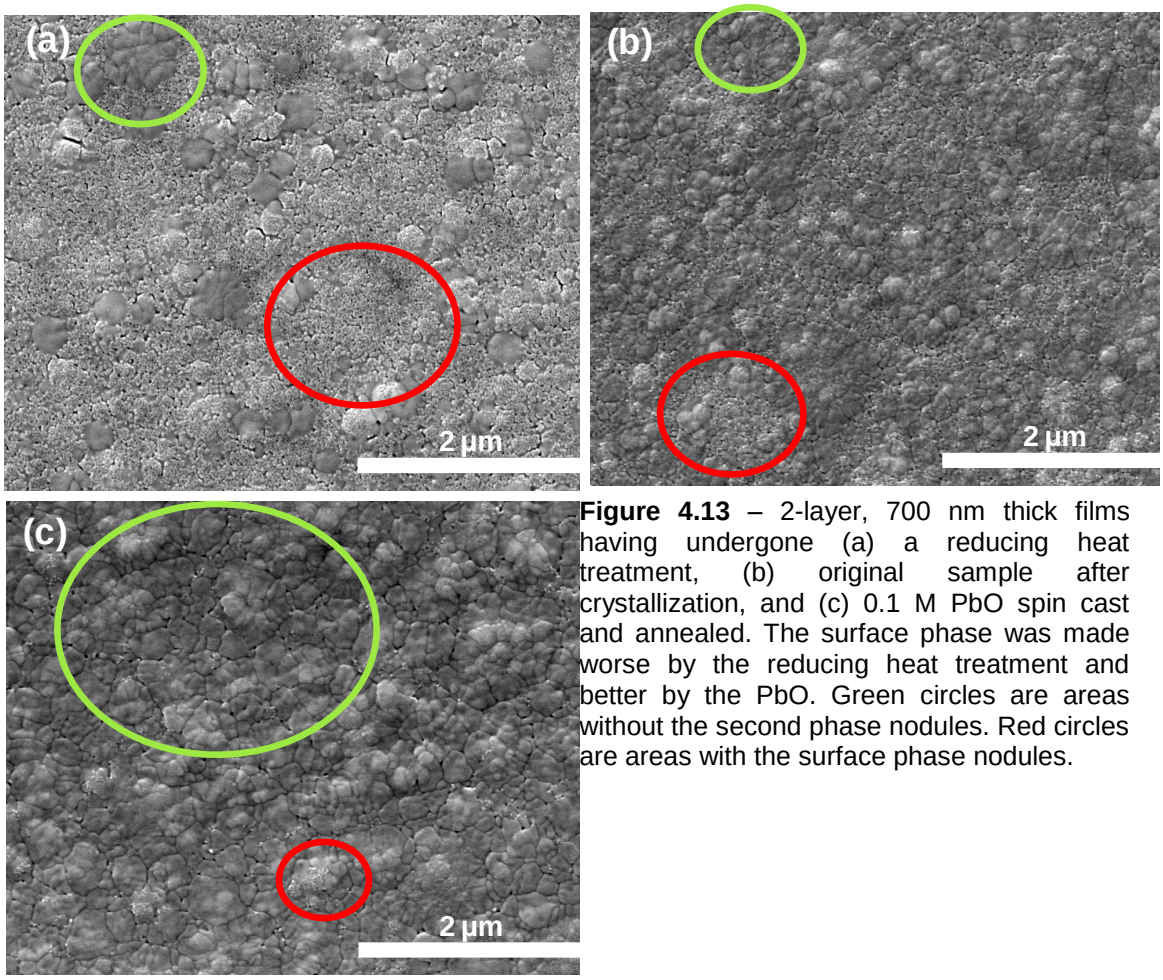

Figure 4.13 – 2-layer, 700 nm thick films having undergone (a) a reducing heat treatment, (b) original sample after crystallization, and (c) 0.1 M PbO spin cast and annealed. The surface phase was made worse by the reducing heat treatment and better by the PbO. Green circles are areas without the second phase nodules. Red circles are areas with the surface phase nodules.

The electrical properties for these three films are shown in Figs. 4.14 and 4.15. The low pO_2, low temperature heat treatment was found to increase the dielectric constant and increase the loss, while reducing, in whole or in part, the Cu_2O interfacial layer to Cu. Spin casting and annealing a 0.1 M PbO layer often has the effect of decreasing the dielectric constant, remnant polarization, and the loss, at least at low frequency. The decrease in the remnant polarization is possibly due to a reduction in the space charge associated with the shoulder on the hysteresis loops seen in the original and low pO_2 heat treated cases.

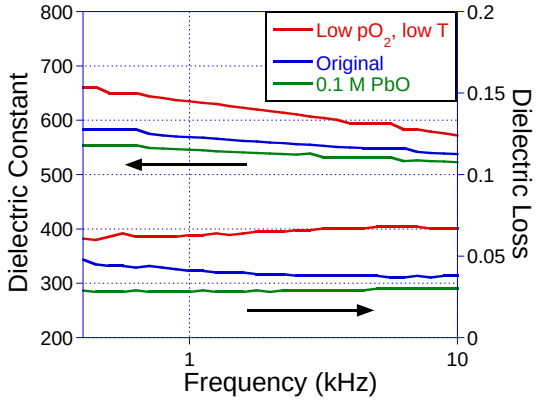

Figure 4.14 – 2-layer, 700 nm thick films having undergone either no extra processing, a reducing heat treatment, or 0.1 M PbO spin casting and anneal.

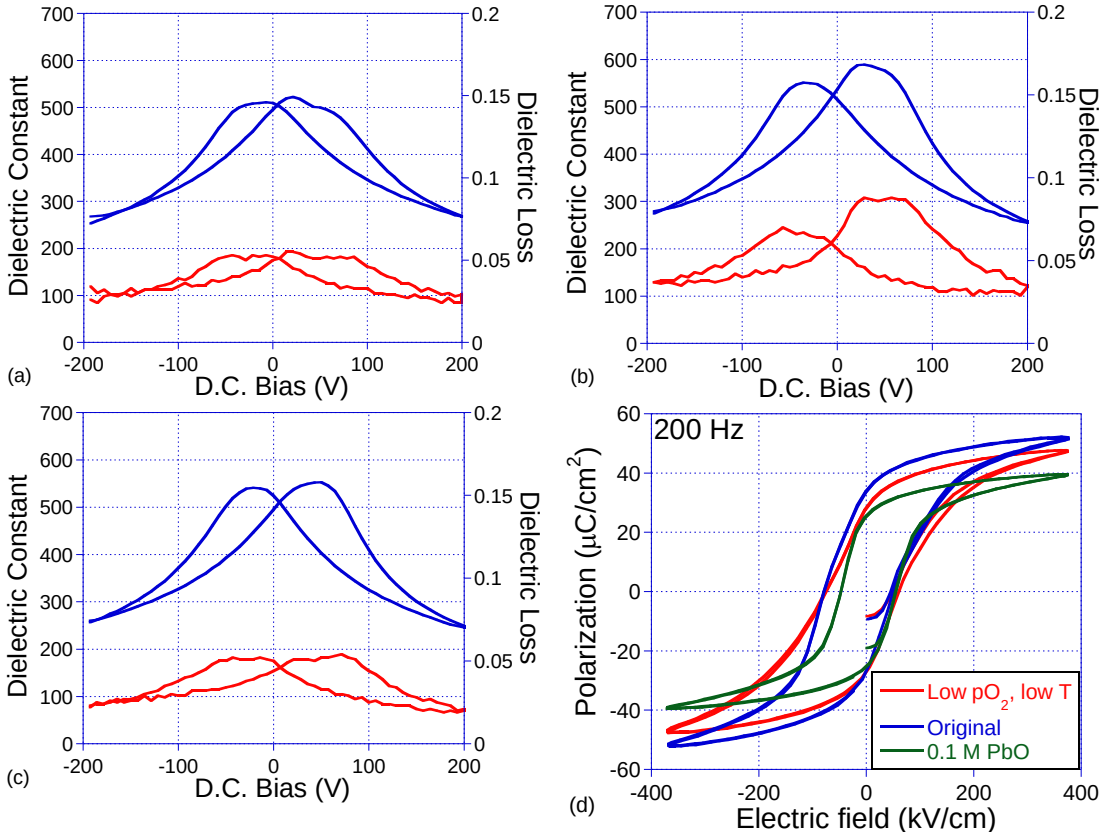

Figure 4.15 – 2-layer, 700 nm thick films having undergone (a) a reducing heat treatment, (b) original sample, (c) 0.1 M PbO, and (d) hysteresis loops for the same films.

4.4 Microstructure of interfacial layer-free PZT/Cu films

The films displayed interesting surface morphologies, as seen by AFM. Fig. 4.16 compares 250 nm and 585 nm thick films wrapped in a copper envelope and crystallized for 550°C, 45 min or 650°C, 30 min or 725°C 15 min, and then annealed at 650°C for 20 min after spin casting a 0.1M PbO layer, estimated to be around 40 nm thick. The films display a trend of increased grain development with increasing temperature. Many tiny grains or nodules, very similar to the ones appearing in the SEM images of section 4.3, appear on the surface, especially at lower temperatures. Unlike the nodules which appeared in the SEM images in section 4.3, these nodules did not disappear with a PbO spin casting and anneal. Furthermore, they have a uniform coverage and do not appear to congregate around the grain boundaries. Despite having such different grain sizes and surface topologies, the films have remarkably similar electrical properties, as will be seen in the next few sections.

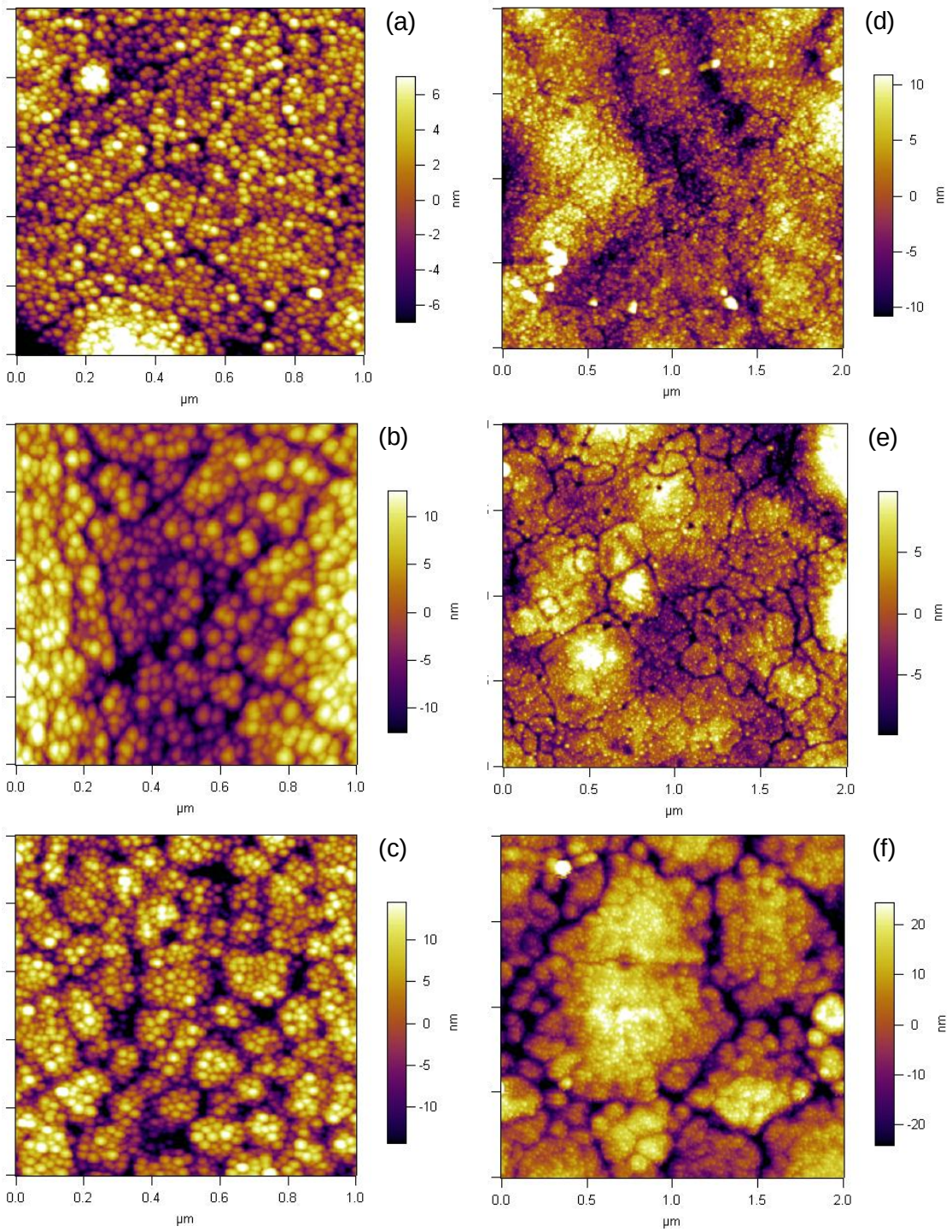

Figure 4.16 – 250 nm films crystallized at (a) 550°C, (b) 650°C, and (c) 725°C; 585 nm films crystallized at (d) 550°C, (e) 650°C, and (f) 725°C. Note the scale difference between (a-c) and (d-f).

Two 990 nm films crystallized at 650°C for 30 min or 750°C for 20 min are shown in Fig. 4.17. The 990 nm film crystallized at 750°C was very rough, although the grains themselves appeared quite smooth and free of nodules. Aside from being the most rough, this film had by far the highest P_r with the spot average being ~41 μC/cm^2. This seemed to be a rather high value, yet it was reproduced with very similar results; the average P_r was ~38 μC/cm^2. Despite having a very large grain size (even larger than the 750°C film) the properties of the 990 nm film crystallized at 650°C were characterized by very lossy hysteresis behavior and high coercive fields (E_c). Roughness increased with both crystallization time and thickness, as expected; values are given in Table 4.1.

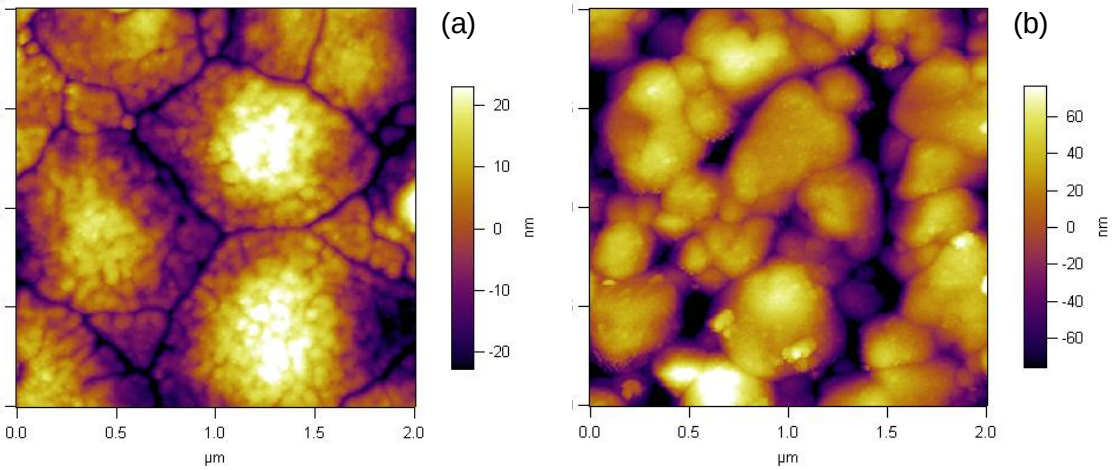

Figure 4.17 – 990 nm films crystallized at (a) 650°C for 30 min and (b) 750°C for 20 min.

Table 4.1 – RMS roughness (nm) for the films in Figs. 4.12 and 4.13. The 990 nm film was crystallized at 750°C.

	550°C	650°C	725°C/750°C
250 nm	4.782 nm	6.214 nm	8.349 nm
585 nm	5.348 nm	4.896 nm	12.011 nm
990 nm		11.322 nm	39.049 nm

4.5 Electrical properties of interfacial layer-free PZT/Cu films

The small signal dielectric constant of the films was 400 – 600 for all films. This fact was interesting for its consistency across a wide range of parameters. The dielectric constant was largely independent of the annealing temperature, and sputtering power and pressure. There was a slight increase in the dielectric constant with increasing film thickness.

The dielectric behavior of a representative film as a function of frequency is shown in Fig. 4.18. The dielectric constant decreases monotonically with the log of frequency. An artifact of the measurement system causes the loss to increase at low frequencies. Otherwise, the loss is well below 5 percent over the range. There is no relaxation such as what is seen in the films with the Cu_2O interfacial layer present.

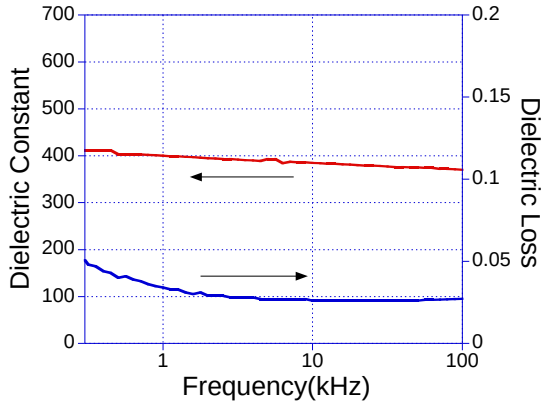

Figure 4.18 – Dielectric dispersion of a Cu_2O free film.

The dielectric constant is considerably lower than (111)-fiber textured PZT films on Pt substrates, which typically have dielectric constants in excess of 1000. [76] In some cases, lower dielectric constants have been attributed to a dead layer. [145] Although no dead layer was observed in the SEM cross section, it was noted in the introduction that even a Cu_2O layer of 10 nm would be enough to drop the dielectric constant by half, according to the series capacitance formula.

The average P_r and dielectric constant at 1 kHz are plotted against the crystallization conditions in Fig. 4.19. 0.2 mm and 0.3 mm diameter electrodes (nominally – actual areas were not measured) were averaged for each sample. Individual spots were found to vary by ≈10 percent in both the P_r and dielectric constant within a sample. There is no obvious correlation between the average P_r and the thickness or crystallization temperature. It is also clear that no strong connection exists between the dielectric constant and crystallization conditions. However, the dielectric constant was seen to increase with film thickness. There was one anomalous sample, 990 nm thick and crystallized at a higher

temperature of 750°C, which had a significantly larger P_r and a slightly higher dielectric constant. This film was subsequently remade using the same process to verify, with similar results, as mentioned above. It is possible that the resultant electrical properties were affected by the changing condition of the target, which was difficult to track. Thick PZT films deposited on copper foils by electrophoretic deposition and sintered at 900°C were reported with a dielectric constant around 600. [146] The dielectric constant reported for PZT films on electroless Ni(P) foils were around 300. [121, 122] Films with a higher dielectric constant of around 800 were made using solution deposition directly on copper foils. [9, 10] It could be that the dielectric constant is simply lower for PZT films on Cu rather than textured Pt substrates. The reason could be a dead layer due to copper interdiffusion, residual stress caused by the thermal expansion mismatch, the reducing atmosphere of crystallization generating oxygen vacancies, or a combination of these reasons.

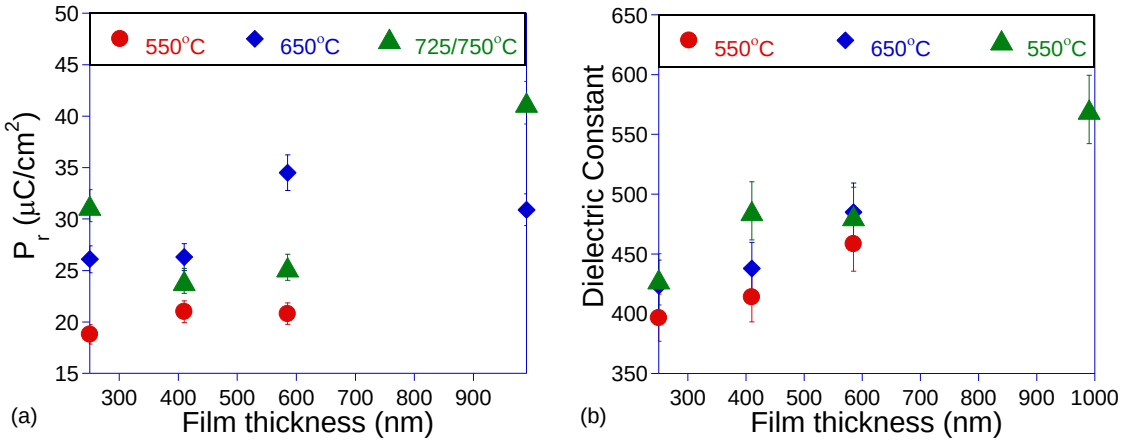

Figure 4.19 – (a) P_r and (b) dielectric constant of films crystallized at 550°C for 45 min, 650°C for 30 min or 725°C for 15 min. The 990 nm film was crystallized at 750°C for 20 min. All films were spin coated with PbO and annealed at 650°C for 20 min.

The coercive fields (E_c) for the films discussed here are plotted in Fig. 4.20. The E_c of the films crystallized at the highest temperature decrease monotonically with increasing film thickness. Scaling theory states that E_c ought to be proportional to $d^{-2/3}$, where d is film thickness, whereas these E_c's fall with ~$d^{-1/4}$. [76, 147] For lower crystallization temperatures the data diverge from what is expected as film thickness increases. This could indicate the presence of a dead layer or internal field, which contributes to an increase in E_c with film thickness relative to that expected from the scaling theory.

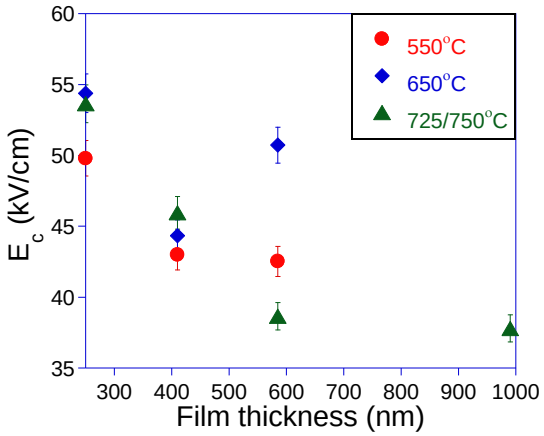

Figure 4.20 – E_c for the films from Figure 4.21. E_c for the 990 nm thick film crystallized at 650°C would not fit on this scale, it was 147 kV/cm.

Hysteresis loops for the films in Fig. 4.19-20 are shown in Fig. 4.21. It is remarkable that the PZT was so consistent over such a large range of crystallization conditions and film thickness. The 990 nm films were a notable exception. Recall that all of the 990 nm films had some kind of second phase present before the PbO spin coat and anneal. Crystallized at 650°C, the hysteresis appeared to be lossy with a very high E_c and a P_r very similar to thinner films. Crystallized at 750°C, the film had very sharply defined loops and a high P_r which averaged 41 μC/cm^2 over the 10 electrode spots which were tested. This value is less than that obtained from *c*-axis, (001)-oriented epitaxial films on MgO, which have P_r of around 50 μC/cm^2. [148, 149] However, this P_r compares favorably to those obtained from solution deposited PZT on copper substrates, around 20 – 26 μC/cm^2, although the dielectric constant is still smaller than those films. [9, 10, 146] As before, the second phase noted in the XRD patterns was removed by the process of spin coating and annealing PbO.

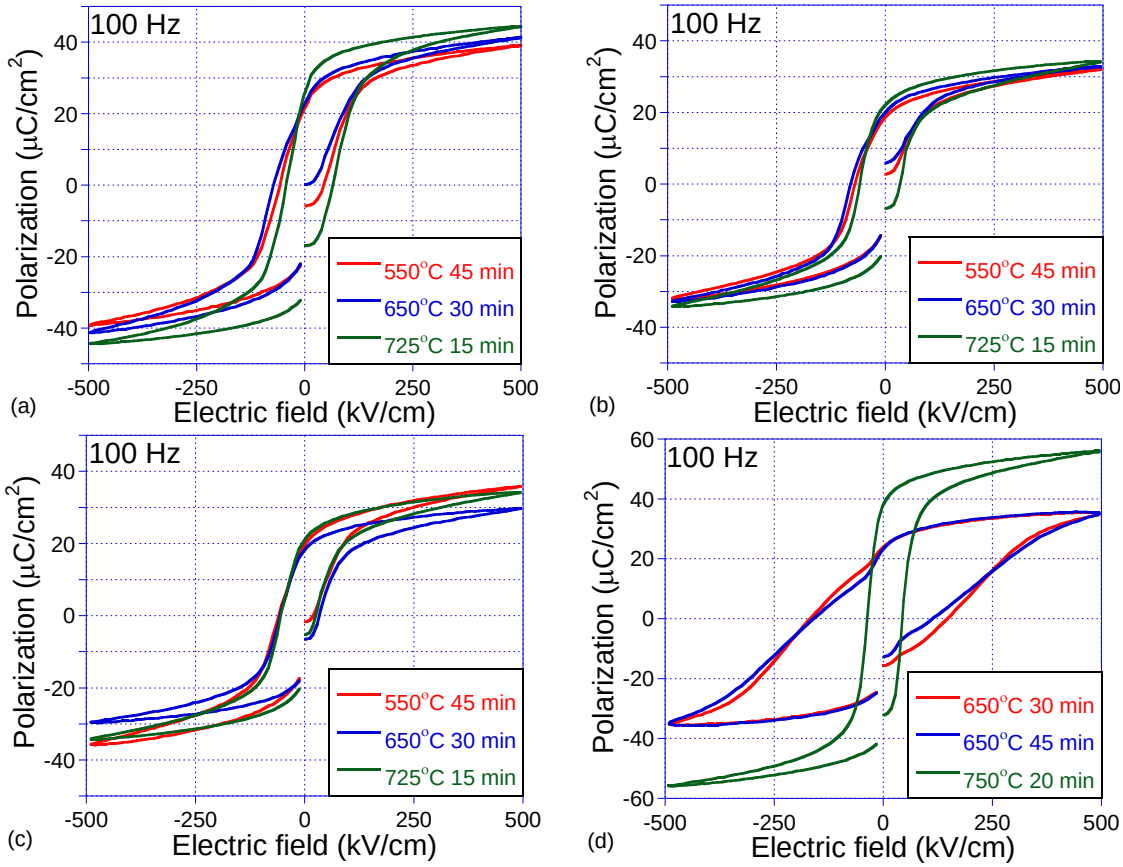

Figure 4.21 – Hysteresis loops for the films in Fig. 4.12; (a) 250 nm, (b) 410 nm, (c) 585 nm, and (d) 990 nm.

All of the hysteresis loops are shifted -15 kV/cm on the abscissa, indicating the presence of an internal electric field. [34] In this case the measurement is made with respect to the top electrode; the bottom electrode (the Cu foil substrate) is always at ground. The sign of the internal bias field is therefore positive with respect to these coordinates. This is consistent with a concentration of holes due

to oxygen vacancies at the top surface of the film. It has also been found that the deposition of Pt, Ag, or Cu can decompose Pb-O bonds at the surface, thus forming a Schottky barrier. [80] This is thought to be the result of competition between the condensation energy of the metal/PZT surface and the strength of the Pb-O bonds at the surface of the PZT film. It was proposed that the activation energy of the reduction would be smaller in a situation where the surface has many defects, as might be the case with PZT thin films annealed in a reducing environment. [150] Such a reduction of Pb at the surface may also cause more dangling bonds, as well as which increase the effective internal field further.

4.6 Comparison to previous work on PZT/Cu films

As was discussed in the introduction and earlier in this chapter, research has been conducted on PZT/Cu thin films. Most utilized was a solution method, sol-gel synthesis, to deposit films. A short summary of those efforts, and how they differ from this work, is given below.

In 2001, researchers at North Carolina State University (NCSU) deposited lanthanum-doped PZT onto electroless nickel-coated copper foils from a solution. [121] As-deposited films were pyrolyzed at 450°C for 15 min followed by crystallization at 600°C for 30 min. All of this was done in a tube furnace under flowing N_2. An interlayer around 30 nm thick was detected by transmission electron microscopy (TEM) and used to explain the low dielectric constant of 240

at 10 kHz. In 2005, several researchers from NCSU reported the successful fabrication of PZT thin films directly onto copper foil substrates without any observed interfacial layer. [9, 10] In both studies, films were thermolyzed at 400°C prior to crystallization at 650°C in flowing N_2. The dielectric constant varied from 800 – 1050, and the P_r from 20 – 26 μC/cm^2. One important difference in these two studies was the attribution of a Cu_2O interfacial layer to various factors. Kingon varied pO_2 and found the formation of Cu_2O to follow closely with the thermodynamic equilibrium prediction. Losego tried several processes and tried crystallizing at both 10^{-6} and 10^{-17} atm O_2 and found no appreciable difference in Cu_2O formation on changing the pO_2. Variations in chemistry and heating and cooling temperature-pO_2 curves in the two experiments may be responsible for the differing conclusions. It should be noted that a flowing N_2 environment is sufficient to oxidize copper, and this was perhaps not observed due to the PZT film acting as an oxygen diffusion barrier. Published work since these studies has continued in the same vein, and with similar results to those discussed above.

An important difference between this and previous work is that our samples were quenched (i.e. inserted and removed directly to and from the hot zone in the thermodynamic stability window) whereas films in previous works were not. Another key element of this work is the wide range in film thickness and crystallization temperature over which films could be crystallized. However, due to the necessity of wrapping films in a copper envelope, the pO_2 is apparently not

a variable which can be precisely known using our experimental method although it is assumed to be just below the Cu/Cu_2O equilibrium line. Results of several previous studies, and the work presented earlier in this chapter, are briefly summarized in Table 4.2.

Table 4.2 – Comparison of previous and current work: processing and electrical properties. Note that an N_2 atmosphere will give a pO_2 of around 10^{-6} atm.

Film/Substrate	Deposition method	$T_{pyrolisis}$ (°C)	T_{cryst} (°C)	pO_2 (atm)	Interfacial layer	P_r ($\mu C/cm^2$)	Dielectric constant	Refs.
600 nm PZT/ e-Ni/Cu	sol-gel	450	600	N_2	30 nm, TEM	not given	240 at 10 kHz	Maria (2001) [121]
700 nm PZT/Cu	sol-gel	400	650	N_2	not det. by XRD	26	700 at 10 kHz	Losego (2005) [9]
1200 nm PZT/Cu	sol-gel	400	650	N_2/H_2, 10^{-14}	not det. by XRD	20	1050 at 1 kHz	Kingon (2005) [10]
700 nm PZT/Cu	sol-gel	400	650	N_2	not det. by XRD	not given	800 at 10 kHz	Losego (2007) [123]
700 nm PZT/Cu	sol-gel	300	650	N_2	Cu_2O	not given	350 at 10 kHz	Losego (2007) [123]
300-1100 nm PZT/e-Ni/Cu	sol-gel	450	550~ 650	N_2	assumed 50 nm	not given	250~350 at 10	Kim (2007) [122]
25 µm PZT/Cu	electro-phoresis	N/A	900	N_2/H_2, 10^{-8}	not det. by XRD	19	600 at 10 kHz	Wu (2009) [146]
250 nm PZT/Cu	sputtered	N/A	550 quenched	N_2/H_2, 10^{-12}	not det. by XRD	19	400 at 1 kHz	this work
250 nm PZT/Cu	sputtered	N/A	650 quenched	N_2/H_2, 10^{-14}	not det. by XRD	26	425 at 1 kHz	this work
250 nm PZT/Cu	sputtered	N/A	725 quenched	N_2/H_2, 10^{-16}	not det. by XRD	31	425 at 1 kHz	this work
990 nm PZT/Cu	sputtered	N/A	750 quenched	N_2/H_2, 10^{-16}	not det. by XRD	40	570 at 1 kHz	this work

4.7 Relaxation, AC conductivity and defects

The films with Cu_2O present always exhibit a space charge relaxation at around 1 kHz, whereas the films without Cu_2O present do not exhibit a low frequency relaxation. The films qualitatively exhibited the Maxwell-Wagner type behavior modeled by Catalan for the temperature dependence of the space charge relaxation found in interfacial layers on multilayer capacitors. [151] At frequencies lower than then relaxation the dielectric loss begins to rise again, similar to that model. However, the relaxation itself is so pronounced that it more closely resembles the Debye model. The temperature dependence of the center relaxation frequency and dielectric constant of the 500 nm, two-layer film from section 4.2 is shown, for several temperatures, in Fig. 4.22.

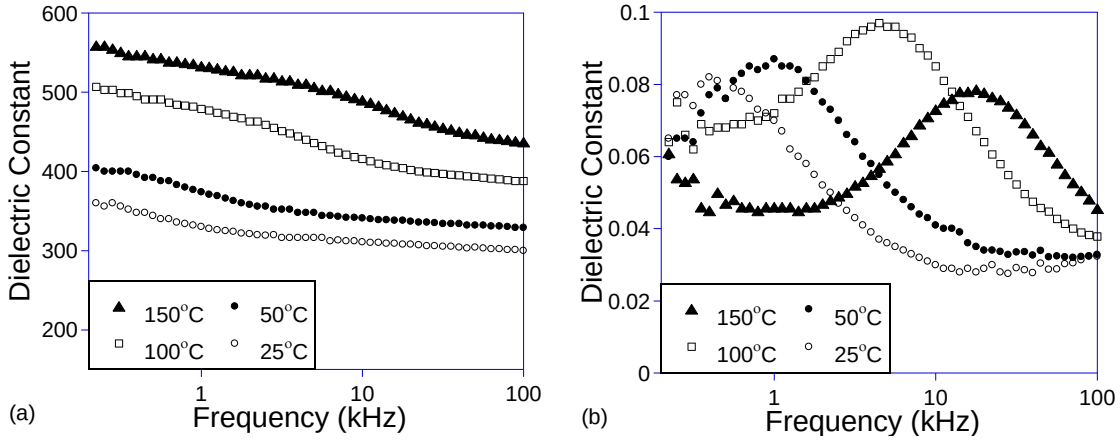

Figure 4.22 – Temperature dependence of dielectric constant (a) and dielectric loss (b) is characteristic of space charge at an interface.

The activation energy of the defect responsible for the relaxation was fit to an Arrhenius form of Eqn. 2.35. The activation energy for the mobile charge carriers responsible for the extrinsic and intrinsic AC conductivity, σ_{AC}, were also fit to an Arrhenius form of Eqn. 2.33 and 2.34, respectively. The work functions of the electrode materials used in this research, Cu (4.65 eV) and Ag (4.25 eV), are very similar, as are the Schottkey barrier heights PZT/Cu (2.11) and Ag/PZT (2.21) calculated for 20/80 PZT. [80, 152]

Cu_2O has several kinds of shallow traps, where the trap energy lies below the Fermi level, with $E_A=(E_t-E_v)$ of 0.45 eV and 0.25 eV which are attributed to a Cu vacancy and either a Cu di-vacancy complex or an interstitial oxygen according to the theory of Peterson and Wiley. [153-155] Their model was chosen for this comparison because their temperature range, on which the system and the activation energies depend, overlapped with the crystallization temperatures used in this research. The Cu di-vacancy is ultimately deemed more likely since the interstitial oxygen is a questionable acceptor, and the Cu vacancy is found to be 10 times more mobile than the oxygen interstitial. [156] Furthermore the enthalpy of formation of oxygen interstitials is much higher than that required to form a copper vacancy and so Cu_2O is decidedly p-type under all but the most extreme conditions. [155] The enthalpy of formation of a copper vacancy is said to be around 0.76 eV, which matches the average value of several authors, 0.74 eV, well. [106, 155, 157-159] A Cu_2O film has a dielectric constant of around 7-12 around 1 kHz. [79, 106]

PZT has a trapped hole concentration which decreases with increasing temperature with a trapped hole activation enthalpy ($\Delta H_A/2$) of -0.4 to -0.49 eV, having a trap energy or acceptor ionization enthalpy of 0.7 eV. [160, 161] At temperatures up to 375 K, deep traps with $E_A=(E_v-E_t)$ around 0.39 eV exist above the Fermi level, calculated to be E_F=0.29 eV. Also, shallow traps, $E_A=(E_t-E_v)$ of 0.19 eV to 0.3 eV exist, right at or just below the Fermi level, which were reported for activation of the space charge limited current (SCLC) hole mobility. [85] Above 400 K the conduction became Schottky emission. Extrinsic and intrinsic conduction were found to have E_A=0.1 eV and E_A=0.53 eV, respectively, in $PbZrO_3$ (PZ) with a transition temperature at 400 K. [162] Both of these were attributed to shallow traps, although the Fermi level was not calculated (the band gap of PZ is higher than that of MPB PZT by as much as 0.6 eV). [163] Given the large band gap of PZT, these were attributed to shallow traps. Extrinsic oxygen vacancies make the conduction p-type, and the Pt/PZT and Au/PZT energy barriers suggest that p-type conductivity gives the most reasonable values for the electron affinity. [85, 160] Typical space charge defect density is on the order of 10^{18}-10^{19} cm^{-3}. The free carrier concentration is highly dependent on temperature, but experiments have found it to be around 10^{14} below 400 K. [85]

Plots of temperature dependence of the dielectric relaxation frequency, ω_R, and AC conductivity, σ_{AC}, are shown in Fig. 4.23 for three single layer films and one double layer film with a Cu_2O interfacial layer, and not wrapped in a copper envelope. The single layer films were crystallized at 725°C for 10 minutes near

the Cu_2O equilibrium curve. The two-layer film is the one from section 4.2 along side data from only the first layer, crystallized at 725°C in the middle of the Cu_2O-PbO stability window, and also not wrapped in a copper envelope.

The first layer from the two-layer film displayed no dielectric relaxation. There is a distinct transition temperature for the relaxation activation energy in the range 323-373 K for the thicker 500 nm films, but it is very slight for the thinner films. The transition can be seen in σ_{AC} in all films, at the same temperature. Extrinsic conduction was observed to increase with increasing film thickness. Activation energies and transition temperatures are summarized in Table 4.3. It must be emphasized that a defect analysis based on activation energies derived from the Arrhenius equations is only valid if a single defect dominates the relaxation or σ_{AC}. [82]

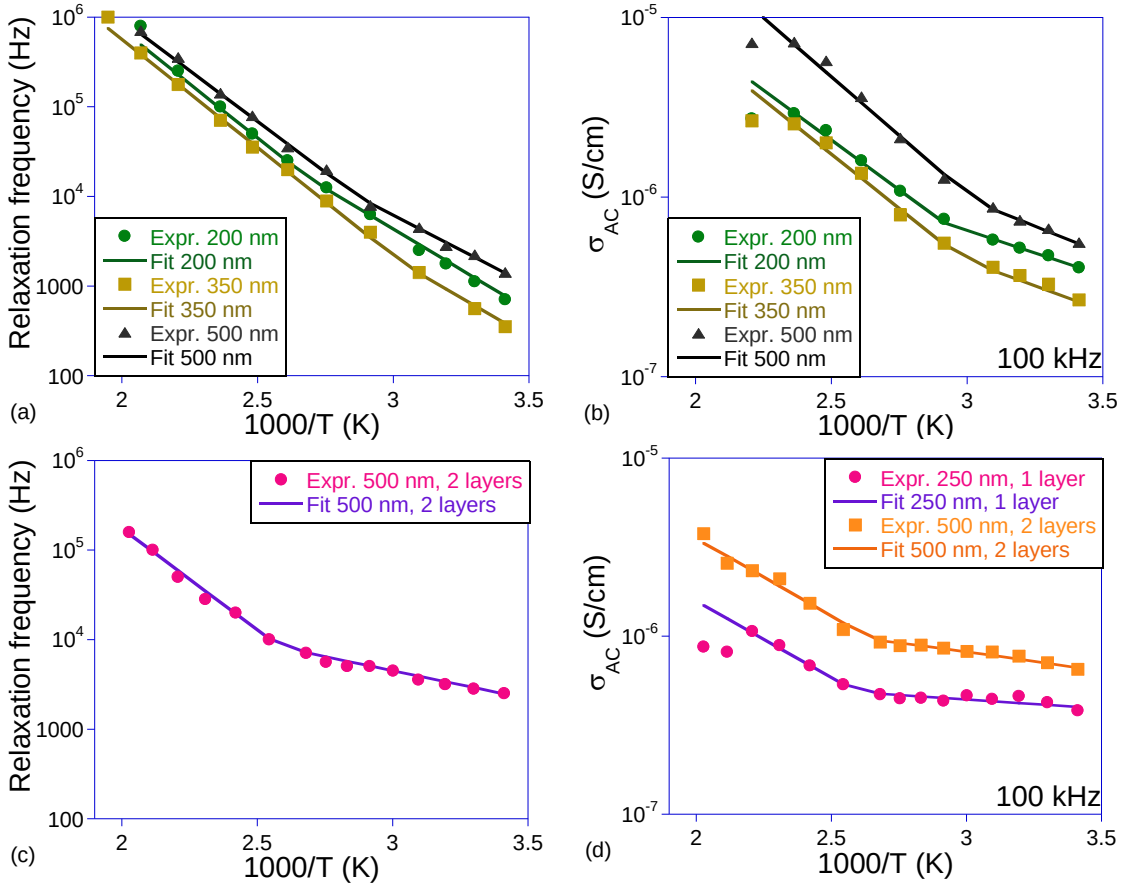

Figure 4.23 – Activation energies for (a) dielectric relaxation and (b) AC conductivity for single-layer films and (c) dielectric relaxation and (d) AC conductivity for double-layer films with a Cu_2O interlayer.

In the case of Cu_2O free films, there was no dielectric relaxation to observe. Plots of the temperature dependence of σ_{AC} are shown in Fig. 4.24. In the low temperature region, σ_{AC} actually decreased slightly as the temperature increased. Again, extrinsic conductivity was observed to increase with film thickness. The 990 nm thick film crystallized at 750°C yields a higher extrinsic conductivity but exhibits almost no temperature dependence until a higher temperature.

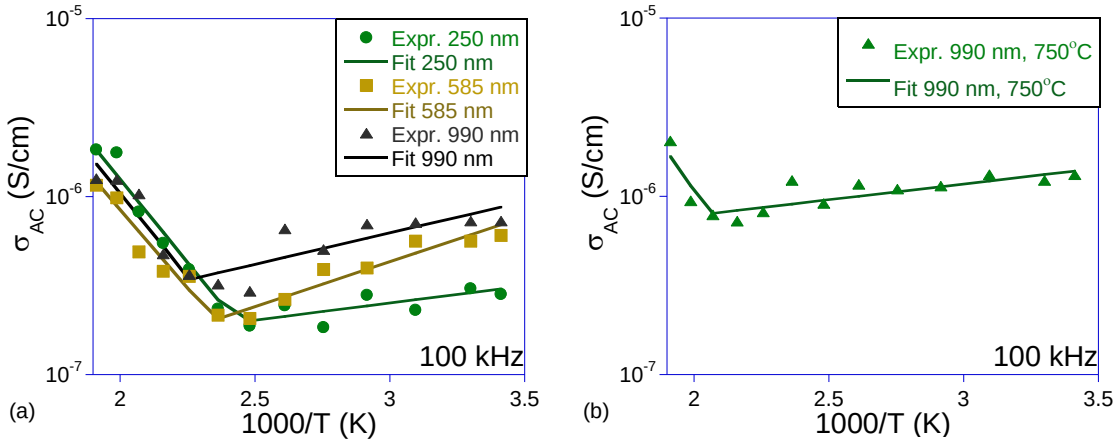

Figure 4.24 – (a) Activation energy for thermally activated conduction in single layer films of various thickness crystallized at 650°C for 30 min and (b) for the 990 nm thick film crystallized at 750°C for 20 min. All films were wrapped in Cu_2O and were spin coated with 0.1 M PbO and annealed for 20 min.

Table 4.3 – Experimentally determined activation energies for the dielectric relaxation and σ_{AC} for the films described above. The in the column headings low T and high T refer to the extrinsic and intrinsic regions, respectively, "relax." refers to data from relaxation frequency-1/T plots and "cond." refers to data from σ_{AC}-1/T plots.

	Cu_2O present	E_A (eV) low T (relax.)	E_A (eV) high T (relax.)	E_A (eV) low T (cond.)	$(E_A+H/2)_{(H)}$ (eV) high T (cond.)
250 nm, 650°C, 1 layer	**no**	**n ne**	**none**	**negative**	**0.37**
585 nm, 650°C, 1 layer	**no**	**none**	**none**	**negative**	**0.35**
990 nm, 650°C, 1 layer	**no**	**none**	**none**	**negative**	**0.37**
990 nm, 750°C, 1 layer	**no**	**none**	**none**	**negative**	**0.43**
200 nm, 725°C, 1 layer	**yes**	**0.36**	**0.48**	**0.1**	**0.22**
350 nm, 725°C, 1 layer	**yes**	**0.35**	**0.48**	**0.11**	**0.24**
500 nm, 725°C, 1 layer	**yes**	**0.31**	**0.45**	**0.12**	**0.26**
250 nm, 725°C, 1 layer	**yes**	**none**	**none**	**0.02**	**0.17**
500 nm, 725°C, 2 layers	**yes**	**0.125**	**0.45**	**0.07**	**0.21**

The relaxation is clearly connected to the presence of Cu_2O. The relaxation does not appear on samples without Cu_2O and its magnitude becomes smaller as the copper oxide disappears. The question is whether the formation of Cu_2O causes vacancies in the PZT layer or whether there are defects in the Cu_2O which are causing the relaxation. The carrier concentration and number of traps have been found, by others, to increase in the range 300-375 K, and here both the relaxation and conductivity data show a change in slope in that range. [85] There is no such transition in the activation energies for Cu_2O occurring below 600 K, which indicates that the relaxation is due to oxygen vacancies in the PZT, rather than Cu_2O.

The activation energy of the relaxation for the three single layer films with Cu_2O averages to 0.34 eV. The value appears to change to an average E_A of 0.47 eV at around 353 K. The relaxation frequency is increasing faster with temperature, indicating some kind of change in the system is occurring. One possibility is that trapped moisture from processing is heated and reacts with the Cu_2O to form CuO.

Meanwhile, the activation energy for σ_{AC} indicates extrinsic conduction with E_A=0.1 eV until the transition temperature, at which time the shallow trap levels are accessible by the thermally activated charge carriers. The negative slope of σ_{AC} vs. 1/T is, on average, 0.22 eV for the intrinsic conduction which includes the

enthalpy term which could indicate the thermal oxidation of shallow traps, $V_O^{//}$. The strong relaxation and bounty of shallow traps would indicate hopping is the dominant conduction mechanism. Also, the abundance of shallow traps implies that oxygen vacancies are the primary defect responsible for conduction. It is possible that Cu_2O scavenged from the film was the cause of the oxygen vacancies. Also, XPS data had indicated the diffusion of copper into the PZT, which could have displaced some Pb in the lattice.

In the case of the Cu_2O-free films past the transition temperature, the slope of lnJ-1/T was, on average, 0.37 eV. Subtracting the trapped hole activation enthalpy from the slope gives a value for the acceptor ionization enthalpy,

$E_A=0.37-\Delta H_A/2=0.37+0.4=0.77$ eV

which is in good agreement with one literature value of 0.7 eV. [161] These are deep traps indicating that cation vacancies are responsible for conduction in these films. This increase in conduction does not set in until the transition temperature at ~375 K. The initial negative slope at lower temperatures is likely due to instrumental noise.

As an aside, several researchers have advised annealing the film just above the Curie temperature in flowing N_2 in order to achieve lower conductivity from the samples. [82, 83]

4.8 Conclusions and future work

The first attempts at using layered samples to control the observed trends in copper substrate oxidation with film thickness had limited value. Interfacial layer (Cu_2O)-free films were finally obtained by obtained by wrapping the films in copper foil during crystallization and any subsequent annealing step. A PbO spin coat and anneal was found to have effects on the microstructure such as reversing minor amounts of second phase (possibly fluorite-like) near the surface. As well, additional annealing in the presence of PbO was found to reduce the Cu_2O interfacial layer while retaining good film quality.

The grain size was found to increase with temperature over the range 550°C to 750°C, as well as with film thickness from 250 nm to 1 μm. The development of the microstructure with temperature and thickness is interesting, although the impact on electrical properties remains unclear. A series of sputter targets should be made, of varying composition in PbO and sputtered at several power densities, pressures and target-substrate distances and the films crystallized with the copper envelope technique to determine the best conditions for deposition separate from the pO_2 variable.

The electrical properties including the dielectric constant and loss tangent maintained consistency over a wide range of crystallization conditions and film

thickness. However, at the extreme end of both film thickness and temperature it was possible to achieve films with fairly high P_r. It would be interesting to attempt the method of Warren, *et al*., who noticed excellent recovery of fatigued films by application of a poling field in the presence of a UV light. [68]

The relaxation phenomena, activation energies and transition temperatures were consistent across a wide range of single and double layer films of various thicknesses and crystallized at different temperatures, which had a Cu_2O peak detectable in the XRD pattern. In the future, it would be interesting to study the effect of pO_2 on the mobility activation, to determine the n or p-type conductivity as well as the type of defect(s) present in PZT/Cu films annealed at low pO_2. Another idea would be to attempt a UV-ozone re-oxidation, if the films were determined to exhibit n-type conduction. It would also be beneficial to finalize the exact conduction mechanism for samples with and without copper oxide.

5. Extrinsic contributions to polarization

This chapter is concerned with the extrinsic contributions to the dielectric properties of PZT on Cu foils. The extrinsic component of polarization is due to domain reorientation and is most often associated with hysteresis. The small field dielectric constant also has a large extrinsic component thought to be due to be due to the oscillations of domain walls. Defect pinning of domain walls might reduce this extrinsic contribution in $Pb(Zr,Ti)O_3$ (PZT) films. This effect may be markedly worse in PZT on copper foils, which are necessarily crystallized in reducing environments where both oxygen and cation vacancies are formed more readily.

Substrate clamping is another factor that can affect the mobility of domain walls in a thin film. Several factors related to the copper foil substrate are hypothesized to either increase or decrease the mobility of domain walls in PZT/Cu thin films. The large compliance of the copper foil is generally thought to improve the mobility of domain walls in PZT since the foil is more susceptible to elastic deformation. However, the difference in the thermal expansion coefficients of PZT and copper, with copper being up to four times that of PZT, means that the crystallized films are subject to considerable compressive thermal residual stresses in the plane of the film. These compressive stresses could limit the ability of the PZT to switch due to domain clamping resulting in an increase in the coercive field with increasing stress. [164, 165] However, the compressive

stresses may also cause an increase in the remanent polarization by opposing back-switching when the field is withdrawn. [97, 98] The determination of residual stress, as well its potential effects on electrical properties, will be discussed in this chapter.

5.1 Comparison of Stoney's and $\sin^2\psi$ residual stress

It was shown in chapter 4 that the dielectric constant could be correlated to film thickness and roughly to crystallization temperature over a wide range. However, the remanent polarization was not well correlated with the thickness or crystallization temperature. One consideration is that films are expected to be subjected to a great amount of residual stress, and this has a dominant impact on the electrical properties. The formation of 90° domain boundaries in a film is a well-known mechanism for stress relief. [166] The films are presumed to be under large compressive stresses in the plane due to the thermal expansion mismatch between Cu and PZT.

The goal of this section is to describe the effect of stress, as determined by the $\sin^2\psi$ method, on the properties of the thickness and temperature series films discussed in chapter 4.4 and 4.5. The samples were square coupon films, unsuitable for a curvature measurement via Stoney's method. These were of varying thickness and crystallized at 550°C to 725°C except for the thick 990 nm

film which was crystallized at 750°C. A coat of 0.1 M PbO was spin cast and annealed for 20 min on all the samples.

Stoney's method is a method for determining the average biaxial stress that is not biased by texture or strain depth gradients in the film. On the other hand, it is no help in evaluating anisotropy or stress gradients. It can be used complimentary to the $\sin^2\psi$ method to validate those results. To that end, the $\sin^2\psi$ method was also used to evaluate the stress on the 700 nm thick film strip.

Stoney's equation, which was described in the introduction, was used to calculate the stress in films deposited as approximately 3 cm inch long strips and these results were compared to the the $\sin^2\psi$ method for curvature. A 700 nm thick film was deposited on two flat, polished copper foil substrates which were 25 μm and 100 μm thick before polishing. These substrates were approximately 20 μm and 70 μm after polishing, respectively. The films displayed some curvature after sputtering, which is known to put the deposited film under some compressive stress due to the plasma pressure. The films were then crystallized at 650°C. The curvatures were both determined to be 3.2 cm on the 20 μm substrate and 32 cm on the 70 μm substrate after crystallization. The residual stresses were calculated to be -512 +/-145 MPa and -627 +/-93 MPa for the 20 μm and 70 μm films, respectively. This is assuming a copper bulk elastic modulus of 111 GPa and Poisson's ratio of 0.355. Uncertainty in the measurement is due to an estimated uncertainty in the thickness of +/-2.5 μm for

the 20 μm substrate and +/-5 μm for the 70 μm substrate. This is a measure of the average plane residual stress which demonstrates approximately the extent that the film is being compressed in the plane. The thickness of the film was neglected in this treatment, since it was at least 30 times thinner than the substrate.

All of the films, including the 700 nm thick film deposited on a long strip, showed signs of either preferred texture, stress gradient, or a combination of the two which manifest as a parabolic dependence of the d-spacing on $\sin^2\chi$ at $\chi<30°$. If only to infer the presence of significant anisotropy, the integrated intensities for several peaks were compared to the bulk pattern of 44/56 PZT in the JCPDS database. The ideal ratio of the (100) + (001) to the (101) + (110) integrated intensities in counts per second was divided by the measured ratio and plotted as a function of $\sin^2\chi$ in Fig. 5.1, where data for the 410 nm and 585 nm films are shown. The 990 nm films had the same profile. The 250 nm films did not, and they will be discussed separately, later.

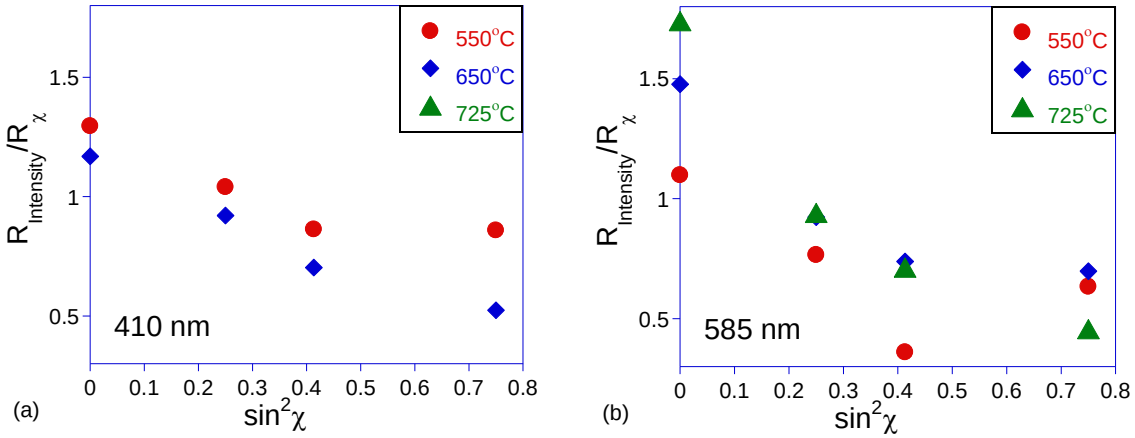

Figure 5.1 – Ideal ratio of the (100) + (001) to the (101) + (110) integrated intensities (counts per second degrees) divided by the measured ratio for (a) 410 nm thick films and (b) 585 nm thick films.

Taking the ratios of peak intensities, it appears that there is some degree of preferred orientation, although the degree is uncertain and we cannot rule out a stress gradient effect as well. Since the films appeared to have some anisotropy, an approximation was used for the calculation of stress from each peak, where the elastic modulus in the direction of each plane's normal was used for the calculation of the residual stress. The direction cosine matrix is approximately the same for a tetragonal and cubic structure and so the simpler cubic equations were used.

$$a_1 = \frac{h^2}{\sqrt{h^2 + k^2 + l^2}}$$ Equation 5.1

$$a_2 = \frac{k^2}{\sqrt{h^2 + k^2 + l^2}}$$ Equation 5.2

$$a_3 = \frac{l^2}{\sqrt{h^2 + k^2 + l^2}}$$ Equation 5.3

The open circuit directional elastic modulus was determined for each plane according to

$$\frac{1}{E_{hkl}} = (a_1^4 + a_2^4)s_{11} + a_3^4 s_{33} + a_1^2 a_2^2(2s_{12} + s_{66}) + (a_3^2 - a_3^4)(2s_{13} + s_{44})$$ Equation 5.4

where s_{ij} are the independent elastic compliance coefficients of the symmetric compliance tensor, the inverse of the stiffness. The elastic stiffness coefficients used for calculation of the directional elastic moduli were calculated for the tetragonal and rhombohedral structures of 50/50 PZT using first-principles. [167]

The films were assumed to be an equal mixture of isotropic rhombohedral and tetragonal PZT for the purposes of calculating average directional elastic moduli for the observed peaks at $2\theta \approx 21.5°$ and $2\theta \approx 31°$. Since the rhombohedral (012) and tetragonal (100)/(001) peaks, occurring at $2\theta \approx 21.5°$, are too close together to resolve the directional elastic moduli for these planes were averaged together. Similarly, the directional elastic moduli for the rhombohedral (104)/(110) and tetragonal (110)/(101) planes, occurring at $2\theta \approx 31°$, were averaged together as well. The calculated average directional elastic moduli for the observed peaks at

$2\theta \approx 21.5°$ and $2\theta \approx 31°$ were 68.4 GPa and 125.5 GPa, respectively. The residual stresses were estimated to be the average of the stress calculated from the d-spacing shift of the peaks at $2\theta \approx 21.5°$ and $2\theta \approx 31°$. Errors in the stress are reported as 1/2 of the difference between those stresses.

A note should be given on several caveats to the above described method. The method allows at least a first approximation to the effective directional elastic moduli and thus residual stress. Obtaining true effective elastic moduli would require a bending apparatus *in-situ* the diffractometer. Also, a very large stress might cause the (001) tetragonal peak to be more prominent than the (100) tetragonal peak at $\chi=0°$ and less so at large angles of χ, for instance. Other factors could conceivably impart a small degree of anisotropy to the film. In that case a rigorous quantitative stress analysis would require the orientation distribution function for the film. Lastly, the surface of the film is preferentially sampled as χ increases, due to the x-ray absorption, according to the Beer-Lambert law. Compositional gradients in the film could potentially cause the lattice parameter to change as a function of χ. We shall see that using the above approximations, the differences between the stresses predicted by observing the (001) or the (110) and (101) planes become acceptably small and also conform surprisingly well in two direct comparisons to residual stress measurements obtained using Stoney's method.

The residual stress measured in the 700 nm thick film on top of the long, thin substrates using the $\sin^2\psi$ method was -652 +/-60 MPa and -792 +/-64 MPa for films on the 20 μm and 70 μm foils, respectively. The d-spacings of the (001) and (110)/(101) planes in the 700 nm film on long, thin 70 μm thick foil are shown in Fig. 5.2. The difference between the residual stresses using the two different methods, not including the uncertainties, are 26% and 27% for the two films. That is not bad for a comparison between the two techniques and at the very least the $\sin^2\psi$ method seems to overshoot by a consistent amount. The match to the results obtained by Stoney's method is good enough to estimate the residual stress by the $\sin^2\psi$ method in side-inclination (χ) mode to a first approximation.

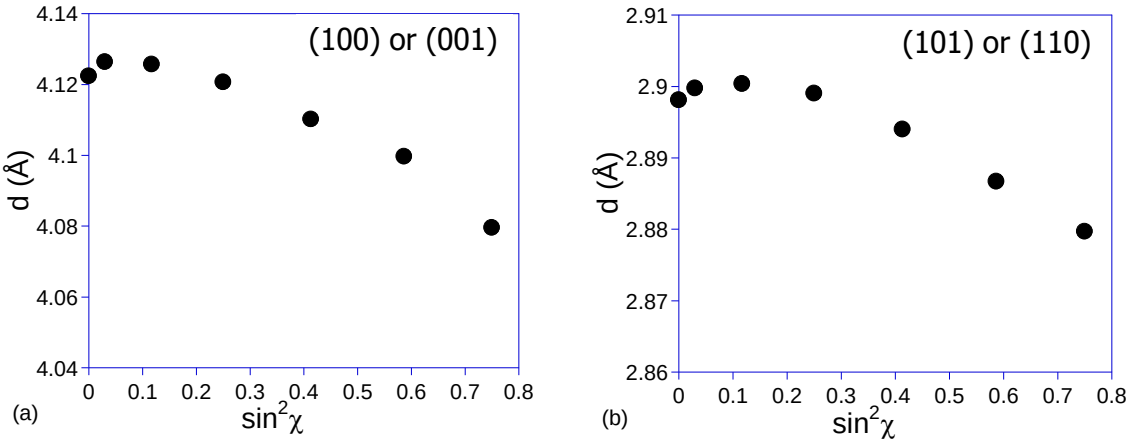

Figure 5.2 – Experimental d-spacing of the (a) (100) or (001) reflection and (b) (110) and (101) reflections as a function of $\sin^2\chi$.

The experimental data from the $\sin^2\chi$ measurement on the square coupon films is shown in Figs. 5.3 to 5.5. The shape of the (001) reflection d-spacing with $\sin^2\chi$ is very much parabolic, while the d-spacings for the (110)/(110) reflections follow a more oscillatory path. Both plots become very linear after 30°, sloping down as

the force is compressive. This indicates that there is partial texture but it is not very significant. The only way to completely deconvolute strain gradients and texture effects is to use the constant volume approach mentioned previously.

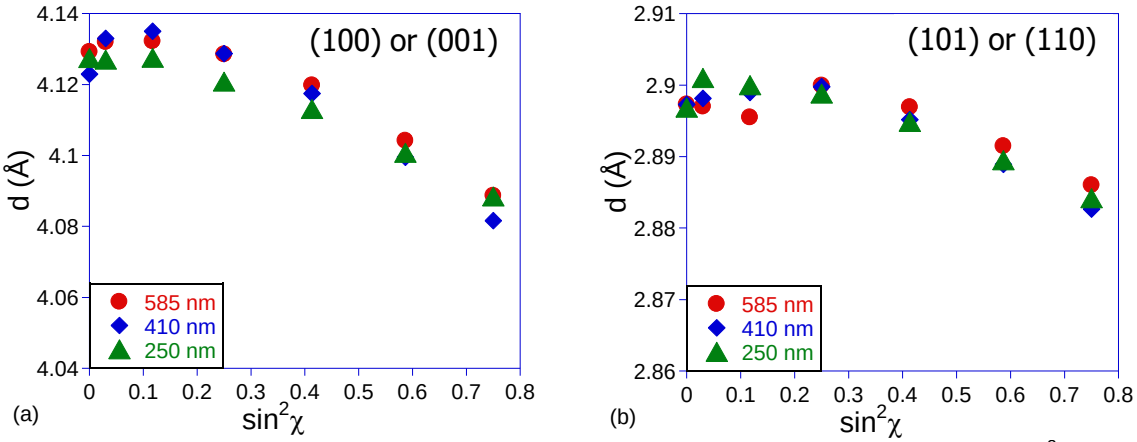

Figure 5.3 – Experimental (a) (100) or (001) and (b) (110) or (101) d-spacing versus $\sin^2\psi$ plots for the square coupon films after PbO spin cast and anneal for the films crystallized at 550°C.

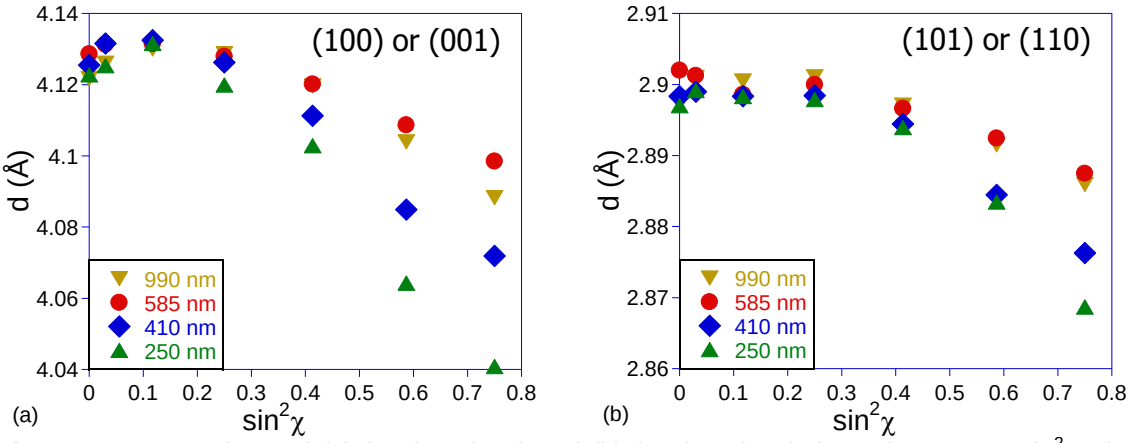

Figure 5.4 – Experimental (a) (100) or (001) and (b) (110) or (101) d-spacing versus $\sin^2\psi$ plots for the square coupon films after PbO spin cast and anneal for the films crystallized at 650°C.

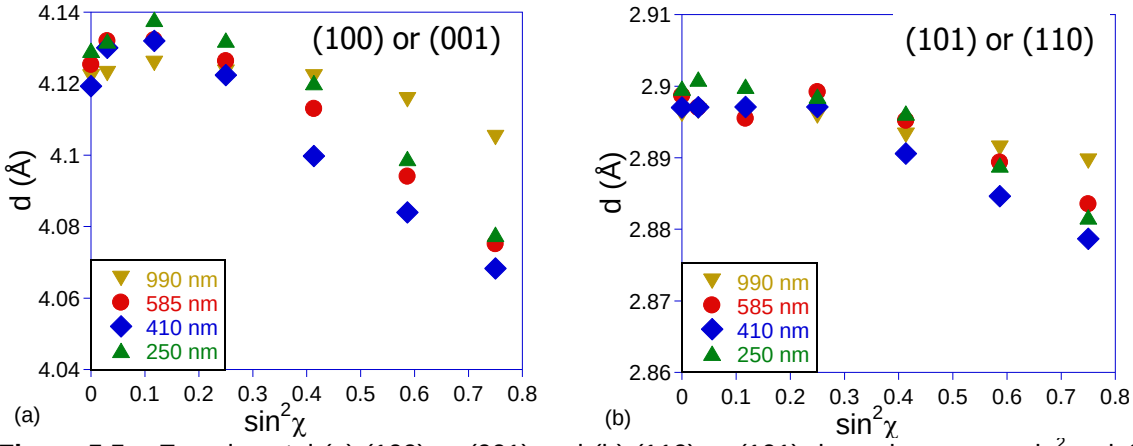

Figure 5.5 – Experimental (a) (100) or (001) and (b) (110) or (101) d-spacing versus $\sin^2\psi$ plots for the square coupon films after PbO spin cast and anneal for the films crystallized at 725°C or 750°C for the 990 nm thick film.

The measured stresses and estimated errors using the techniques and approximations described above are given in Fig. 5.6. This shows that the residual stress tends to decrease with increasing film thickness with the exception of the 250 nm thick films.

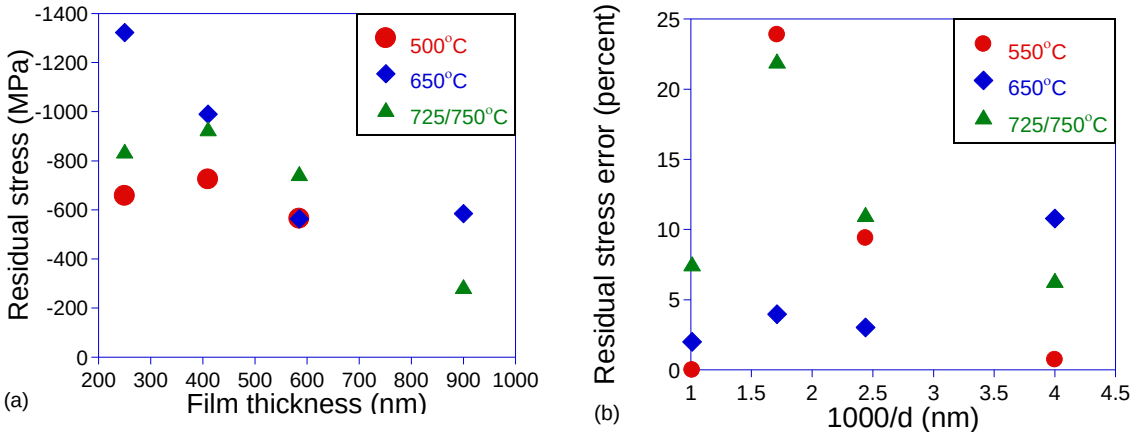

Figure 5.6 – (a) Average residual stress calculated from the (100) + (001) and the (110) + (101) reflections and (b) error, in percent, as defined above.

Stress in the 250 nm film is anomalously low, deviating from the trend of decreasing stress with increasing thickness (except for the sample crystallized at 650°C). In all of the 250 nm thick films and the 410 nm thick film crystallized at 725°C the peaks appeared to separate into pairs with a new peak, at a larger d-spacing, appearing to shift to smaller 2θ relative to the original peak as seen in Fig. 5.7. Without modeling the distribution of the paired peaks in 2θ, it could not be said if the new peak was actually shifting, since the overlap was significant. It is possible that the anomalous calculated stresses in the 250 nm peak were due to this separating of peaks. The stresses for samples with peaks which separated should be larger, but the extent is not certain. The peaks at 21°, 31°, and 38° in 2θ each appear as a single peak. It is not presently understood what caused this separation of the peaks. This separation appeared to occur in all of the 250 nm thick films crystallized from 550°C-725°C and the 410 nm film crystallized at 725°C.

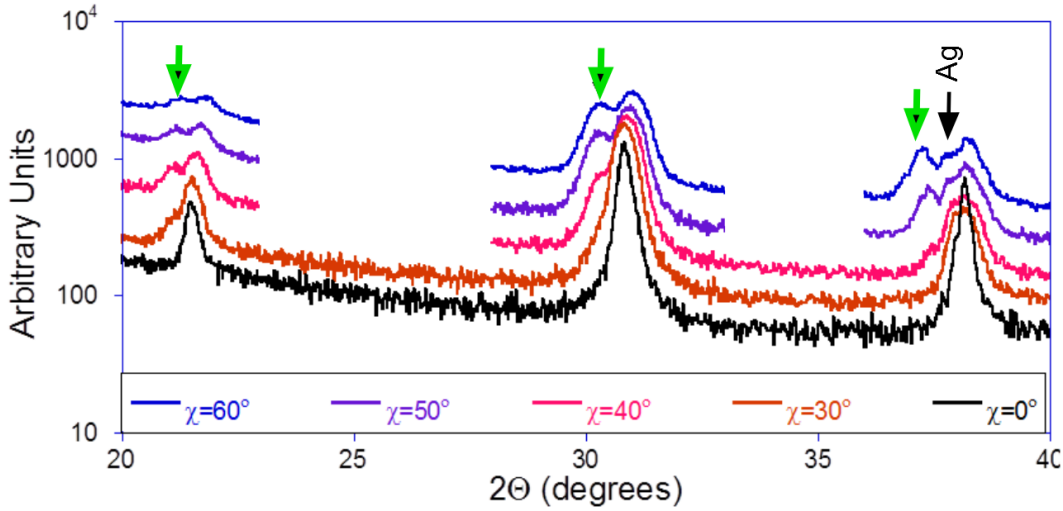

Figure 5.7 – Separated peaks emerging at high angles of χ near 22.1°, 30.2°, and 38.1°. Green arrows indicate the new peaks, which only appear at stage tilts > 30°. The silver electrodes appear as a small shoulder at ~38°.

5.2 Residual stress and relation to electrical properties

The electrical properties are most often positively correlated to the grain size which usually increases with thickness and crystallization temperature. A large grain size is usually associated with improved electrical properties including lower coercive field, and higher remanent polarization and dielectric constant. Thinner films may have more defects per volume, thereby building up a larger internal field, due to having the largest surface area to volume ratio. The residual stress has previously been correlated to the electrical properties. Compressive residual stress has been found to encourage *c*-axis domain orientation and thus increase remanent polarization. [149] Residual stress can reduce the dielectric constant through inhibited domain wall motion and increase of the coercive field and possibly even the rate of fatigue. [164, 168, 169] Unfortunately, the effects of

stress and partial texture of domains cannot always be unambiguously decoupled from grain size, crystallization temperature and film thickness.

A residual stress in the plane of the film has been suggested to increase the formation of either *a*-axis (tensile) or *c*-axis (compressive) domains. [97, 98] In the case of *a*-axis aligned domains the films have a higher dielectric constant while films with *c*-axis aligned domains have a higher remanent polarization. [93] In a nanoscale switching study it was found that a compressive stress normal to the film surface resulted in the inability to switch 90° domains. This suggests that a compressive residual stress in the plane of the film would result in enhanced 90° switching and possibly an increased remanent polarization due to the compression increasing the stability of oriented 180° domains. [164, 170] At the same time large, inhomogeneous strain internal strain fields can lead to the stress minimizing formation of 90° domain walls which imply a mixture of the a-axis and c-axis aligned domains. [97] The critical grain size, below which 90° domain walls do not form, is typically found to lie in the region of 300 nm to 1000 nm which is larger than the grains of 250 nm thick PZT/Cu films but around the grain size of the thicker PZT/Cu films. [171] The evidence discussed in the previous section suggests that there is some degree of anisotropy which favors the the preferential formation of *c*-axis domains. However, the XRD data also shows that the films have a mixture of orientations.

Since the $\sin^2\psi$ method is a macroscopic residual stress measurement, the entire sampling volume provides an average stress value. A stress gradient likely exists due to the free-clamped geometry of a thin film, and the experimental evidence for this is the negative upside down parabolic shape of the d vs. $\sin^2\psi$ plots. The assumption is thus made that the stress gradient is linear in form. Under this assumption, the residual stress gradient is related to the coercive field in Fig. 5.8. The switching behavior of the film is likely to be affected by stress. [165] This should cause an increase in the coercive field with increasing compressive stress gradient, which is indeed seen in the figure.

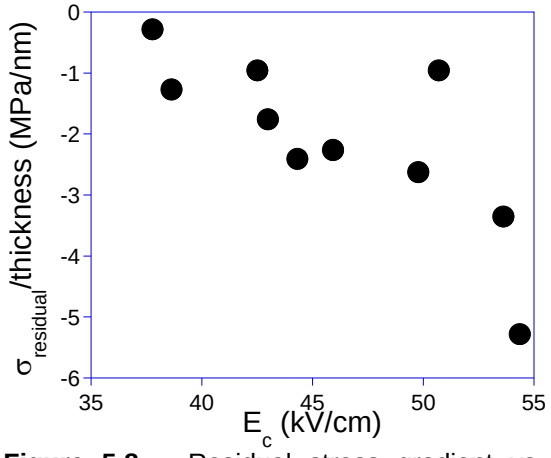

Figure 5.8 – Residual stress gradient vs. coercive field.

However, grain size alone cannot explain the all of the trends in the electrical properties for these sputtered PZT/Cu thin films. The dielectric constant (average of spots) was seen to increase monotonically with increasing film thickness in

chapter 4, Fig. 4.22. The remanent polarization was found to increase with increasing film thickness as well. The remanent polarization of the 250 nm thick film crystallized at 725°C was actually seen to increase relative to the 410 nm and 585 nm thick films. This film had the third highest average remanent polarization of all the films tested, ~31 μC/cm^2. The grains were larger than those crystallized at lower temperatures, though still small relative to the thicker films. For films crystallized at lower temperatures the remanent polarization increased with film thickness. Note that the 990 nm thick film crystallized at 650°C was an exception; however, the extremely large coercive field (~140 kV/cm) seems to imply that there were significant defects which preclude a direct comparison to the other films. The lowest remanent polarization of all the films was from the 250 nm film crystallized at 550°C, as expected. Unlike the 410 nm and 585 nm thick films, the 250 nm films displayed the expected increasing remanent polarization with crystallization temperature.

Residual stress was found to increase with film thickness aside for the 250 nm thick films. The anomalous lower residual stress in the 250 nm thick films coincided with an increase in the remanent polarization. However, it was explained above that the measured stress in the 250 nm thick film is likely underestimated due to a second set of partially overlapping peaks, which appeared as the χ tilt increased, having a d-spacing roughly corresponding to the unstrained position (χ=0°). This has been previously seen in sputtered ZnO films annealed at 400°C to 800°C, where measured residual stresses were on the

order of 2 GPa. [172] It was attributed to a peak asymmetry caused by the different paths of the incident and diffracted x-rays as a function of χ tilt. This explanation is unsatisfactory because the new peaks were only observed in the 250 nm thick films and a 410 nm thick film crystallized at 725°C. There are several alternative explanations for the appearance of the extra peaks.

The appearance of the second set of peaks could be due to plastic deformation which relieved elastic strain. It has been observed that in epitaxial and polycrystalline thin films that elastic strain associated with the lattice mismatch can be relieved through the formation of dislocations. [173] Cracking is another stress relief mechanism. [174] Although the crack density was not calculated, the 250 nm thick films all had a higher number of shorted electrodes which might have shorted through cracks. Plastic deformation has been seen to occur in PZT as low as 70-140 MPa. [93, 175] The threshold for plastic deformation is likely higher in compression than in tension but the residual stresses measured here are high enough. [176] Given the small grains observed via AFM and the fact that the sin2ψ method gives a measure of the macroscopic strain, it seems possible that only some of the grains experienced sufficient stress to cause plastic deformation. Plastic deformation can potentially cause highly asymmetric peaks such as this. [177, 178] This is usually associated with a reduction in properties. [173] There is much reported evidence to suggest there is a relationship between remanent polarization and compressive elastic strain, and it has usually but not always been shown to be a positive one. [97, 179-181] Inhomogeneous internal

strain fields in the film could actually lead to a decrease in the remanent polarization. It should be considered that the measured stress value of the 250 nm thick film is relatively accurate and that a moderate increase in polarization observed in the 250 nm thick film crystallized at 725°C was due instead to the relief of elastic strain in some fraction of grains through the formation of dislocations. The existence of some grains with reduced stress, perhaps even a separate population with greatly reduced stress is plausible, but the peaks actually appear at a higher d-spacing than the peaks at χ=0°, which is very strange.

The second explanation is that the separating peak is due to a residual stress induced phase change from a nominally tetragonal to rhombohedral film, perhaps at the film-substrate interface where the residual stress is thought to be larger. The parabolic shapes of the d-spacing vs. $\sin^2\chi$ plots do indicate a stress gradient. Numerous calculations using the Landau-Devonshire-Ginzberg theory have shown that it is possible that stress during processing can cause a phase change from rhombohedral to tetragonal. [112, 182] Others have predicted a tetragonal to rhombohedral transition, said to be possible in the realm of 650 MPa. [110] Recently, thin PZT films of a nominally tetragonal composition were found to have undergone a tetragonal to rhombohedral transformation at the interface due to a stress gradient. [109, 183] However, there are two problems with this reasoning. The peaks only appear as χ increases, and the incident x-ray beam should be sampling more of the surface of the film, not the substrate-film

interface, where it is expected that the stress is greatest and therefore where the rhombohedral phase might be most likely to form. Also, the peaks which appear do not shift much, if at all, and therefore would indicate the presence of stress-free rhombohedral crystallites which seems unlikely.

If there were a tetragonal-rhombohedral PZT interface it might account for an increased remanent polarization. A Zr-rich surface was observed by XPS in the 2-layer film from chapter 4. Since the amount of zirconium enrichment was significant, as much as 70/30 near the surface, it is quite possible that the surface of the film is rhombohedral. It is also thought that 52/48 PZT thin films often adopt a tetragonal structure in response to residual stresses. [182] A stressed film might have a tetragonal structure throughout the bulk, becoming rhombohedral at the Zr-rich surface. At the interface between the tetragonal and rhombohedral, there may be increased directions available for domain growth which accounts for the increased remanent polarization of the 250 nm thick films. Additionally, the x-ray beam samples more of the surface as χ increases which supports the theory that there is something on the surface which is relatively free of stress. A serious problem with this explanation is that the rhombohedral phase at the interface must be said to be relatively unstressed since those peaks do not appear to shift d-spacing for further χ tilt, in fact they appear to move towards higher d-spacing. This could perhaps be explained since, if the Zr-content increases towards the surface, the bulk d-spacing should increase as we are sampling an increasing amount of the surface. That could potentially offset the

expected effect of a compressive stress, which would normally cause a decrease in the d-spacing.

Three explanations, yet none of them satisfactory, have been provided above for the appearance of new peaks as χ tilt increases. A determination of the actual structure of the film as a function of depth will require a TEM diffraction analysis. Grazing incidence x-ray diffraction (GIXD) could be used to determine roughly whether there are distinct phases at the surface.

5.3 Rayleigh analysis

A primary extrinsic contribution to the dielectric constant is thought to be due to the oscillation of domain walls. It was mentioned in the introduction that the domain wall oscillations can have a reversible component, which appears in the term ε'_{init}, as well as an irreversible component characterized by the Rayleigh parameter. Two factors which are thought to influence the Rayleigh behavior and reduce the Rayleigh coefficient are substrate clamping and electronic defect pinning sites. It was hoped that the substrate clamping would be reduced by using a compliant material such as copper. If substrate clamping were a significant factor then it is reasonable to expect that residual stress might be another factor. The residual stresses in the film may impede domain wall motion.

The electric field dependence of the dielectric constant was measured at 1 kHz. Example plots for the films crystallized at 725°C (and 750°C for the 990 nm thick film) are given in Fig. 5.9. Note that the Rayleigh measurements were made on a different instrument than the dielectric constant measurements. The impedance analyzer used for Rayleigh measurements consistently measured capacitance 6% higher than that used for dielectric constant measurements. The losses determined from both instruments were identical.

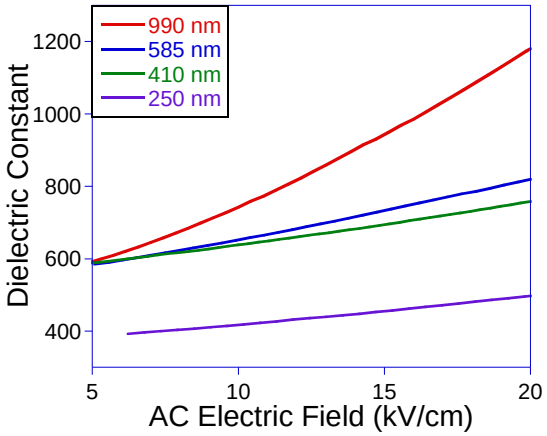

Figure 5.9 – Plots of the AC electric field dependence of the dielectric constant for several films crystallized at 725°C.

The Rayleigh parameter was found to increase with film thickness and temperature (see Fig. 5.10). The Rayleigh parameter is interesting because it gives some insight into processes which might impede domain wall motion. The films crystallized at 725°C showed a monotonic increase in Rayleigh parameter with increasing thickness, whereas the films crystallized at lower temperatures

did not. This could be due to the increasing grain size with thickness. When the grains are below a critical thickness they become essentially single domain. [145] This automatically puts an upper bound on the size to which domain boundaries can move and domains can grow in response to an applied field. However, the grains of the 585 nm thick film are much larger than those of the 250 nm thick film when both are crystallized at 650°C, yet there was no corresponding increase in the Rayleigh parameter. It might have been expected that the higher temperature would create more defects, such as oxygen vacancies, thus pinning the domain walls. Yet that does not seem to be the major factor.

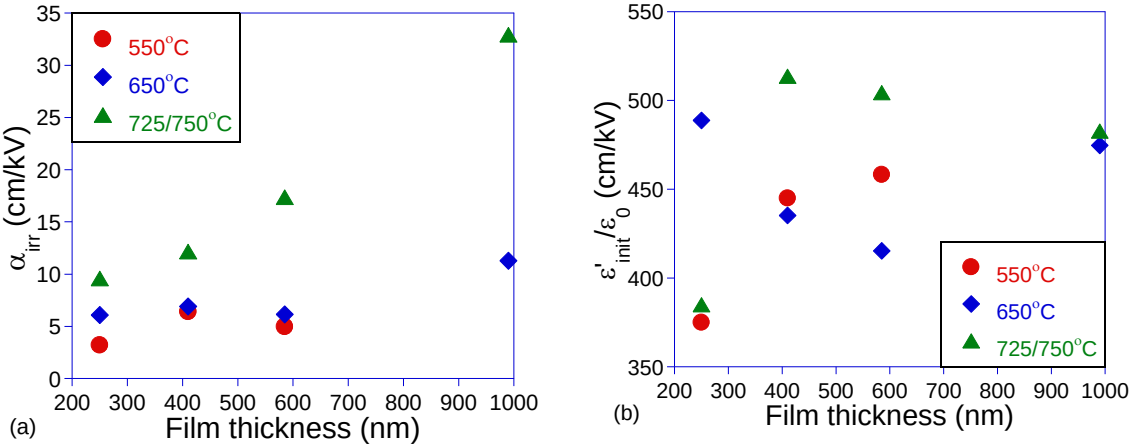

Figure 5.10 – (a) Extrinsic and (b) combined intrinsic and reversible Rayleigh parameters.

The zero-field dielectric constant, or $\varepsilon'_{init}/\varepsilon_0$, parameter showed no such obvious dependence on either thickness or temperature. FORC data (presented in the next section) provides evidence that the intrinsic component of the $\varepsilon'_{init}/\varepsilon_0$ parameter is roughly the same for all of the films but the plot in Fig. 5.10 varies

by around 25 percent. It seems plausible that the variation could be related to the the residual stresses in the film. Reversible domain motion will have an associated lossless energy barrier. Additional constraints, such as the internal elastic energy associated with the residual stress, might limit the reversible domain wall motion and decrease its contribution to the permittivity. The internal strain energy of a ferroelectric element would be proportional to the elastic strain and thus stress as well as the volume of the element which is proportional to the thickness of the film. The product of residual stress and film thickness has units of surface energy, J/m^2. The plots of $-\varepsilon'_{init}/\varepsilon_0$ (negative to assist visual comparison) and the product $\sigma_{residual}$ x *thickness*, are given in Fig. 5.11. Qualitatively the plots for each temperature as a function of thickness match very well. For instance, in both cases the plots from films crystallized at 725°C fall and then rise with thickness. Both of the plots from films crystallized at 550°C fall monotonically with thickness. The only point which is off significantly is the 200 nm thick film crystallized at 650°C, and so this plot was removed from the graphs in Fig. 5.11 for clarity. The connection between $\varepsilon'_{init}/\varepsilon_0$ and $\sigma_{residual}$ x *thickness* product strongly indicates that they are correlated. In general, as the residual stress increases the surface energy increases and $\varepsilon'_{init}/\varepsilon_0$ decreases.

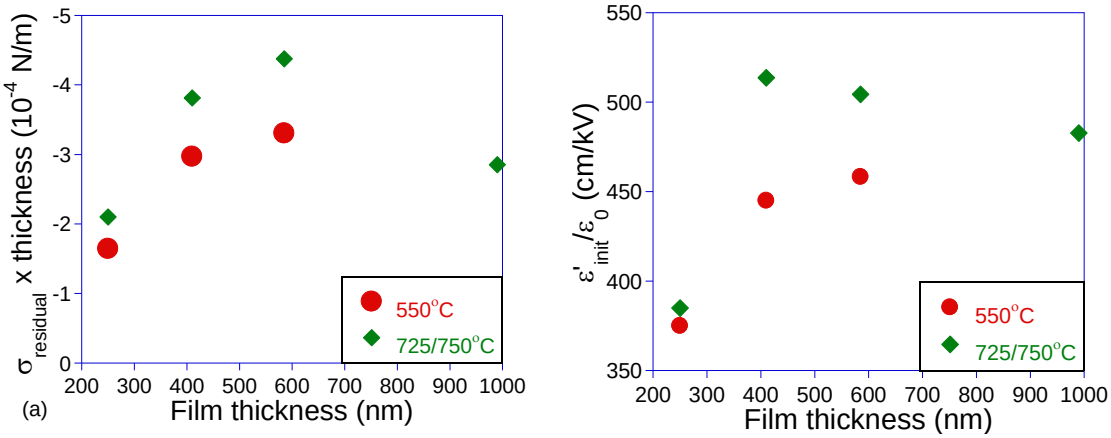

Figure 5.11 – (a) The product of the residual stress and film thickness versus film thickness and (b) $\varepsilon'_{init}/\varepsilon_0$ versus film thickness.

Another interesting metric is the ratio of the Rayleigh parameter to the zero-field dielectric constant, $\varepsilon'_{init}/\varepsilon_0$. Since both are inversely proportional to the electrode area the result is conveniently put in terms of inverse electric field units. This is given in Fig. 5.12. Even given the uncertainty in the measurement, the Rayleigh parameter is shown to increase with increasing film thickness and crystallization temperature. This would be the expected behavior for several reasons. Grain size usually increases with film thickness and crystallization temperature, and larger grains usually have more bulk-like properties. Also, residual stress decreases in the film with increasing thickness, which should reduce the elastic force restricting the motion of domain walls.

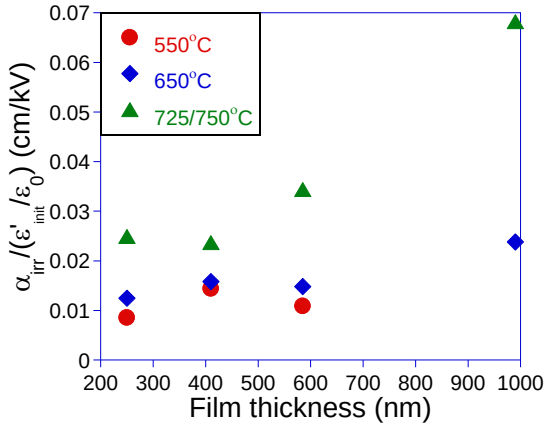

Figure 5.12 – Ratio of irreversible to intrinsic and reversible Rayleigh parameters.

The values for the Rayleigh parameter of the 990 nm films are on par with those typically seen for PZT on Pt/Si substrates. [37, 47, 48] The Rayleigh parameters are smaller for thinner films, which is to be expected. Thinner films experience more clamping due to residual stress and, possibly, defects due to PbO loss during crystallization. The intrinsic part of the dielectric constant is much smaller than that of PZT on other substrates. However, the ratio of the Rayleigh parameter to intrinsic dielectric constant is similar to those reported. It was mentioned in the introduction that the ratio varies from around 0.01 to 0.04, which is the same range of these films. The 990 nm thick film has a much larger ratio of ~0.068. [37, 47, 48] The response, especially for the thicker films with larger Rayleigh parameters, seems to be dominated by the extrinsic mechanism past a field of several tens of kV/cm. This may be due to a reduction in domain wall pinning due to the higher compliance of the copper substrate. The substrate must

deform elastically at the interface in order for the domains at the interface to undergo 90° reorientation.

The imaginary part versus the real extrinsic part of the dielectric constant and the slopes of the plots are shown in Fig. 5.13.

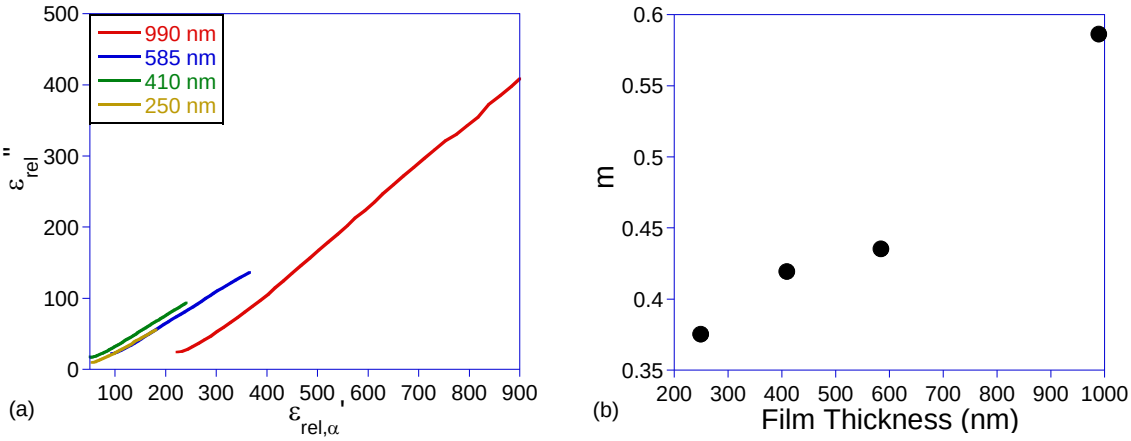

Figure 5.13 – (a) Plots of the imaginary part vs. the real extrinsic part of the dielectric constant and (b) slope of the linear fit, m, vs. film thickness for films crystallized at 725°C (990 nm thick film crystallized at 750°C).

It was mentioned in the introduction that the theoretical slope of this line is $m=3/4\pi$, or ~0.42, when the extrinsic contribution is entirely due to irreversible processes. [45] When the dielectric data from the sputtered PZT/Cu films crystallized at 725°C (750°C for the 990 nm thick film) were plotted in this way, the theoretical slope was not obtained for all films. It was found previously that the slopes of hard, or acceptor doped, PZT often show signs of a reversible extrinsic contribution which lowers the slope of the imaginary versus real extrinsic linear relationship. Evidence of acceptor doping, such as caused by cation loss,

is not unexpected in these films due to the low pO_2 processing environment and was discussed briefly in the introduction and chapter 4. As the film thickness increases, less cation loss might be expected as the surface area to volume ratio decreases. In Fig. 5.13 it does appear that the films are approaching the theoretical value as the film thickness increases from 250 nm to 585 nm.

However, for the 990 nm thick film there is an unexpectedly large slope. Thus, rather than an increase in the dielectric constant due to an increase in reversibility, this suggests an increasing irreversibility caused by a lossy mechanism. Indeed, the film is particularly lossy as the AC field strength is increased, when compared to other films. However, at higher fields the loss was actually less, as indicated by slimmer hysteresis loops and smaller coercive fields (see chapter 4).

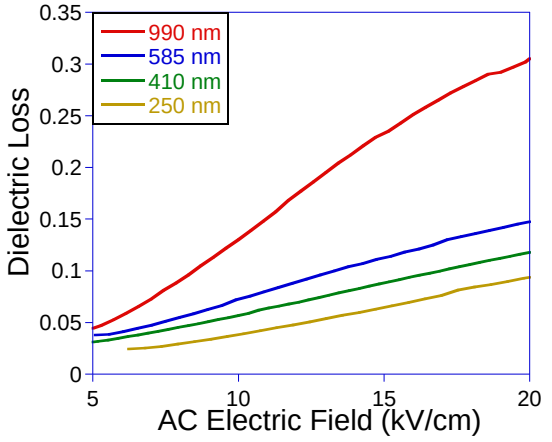

Figure 5.14 – Dielectric loss tangent as a function of AC electric field for the films shown in Fig. 5.12.

5.4 First order reversal curves (FORCs)

It was mentioned in the introduction that FORCs are a valuable tool to assess the fatigue behavior of films and more generally to assess the switching behavior and identify domain wall pinning due to defects. FORCs can also be used to separate the reversible and irreversible components to the dielectric constant at higher fields, and so compliment the Rayleigh data. [48, 184]

The FORC distributions can be computed in the following way; the descending branch leaves the ascending branch of the major loop as the field is removed beginning at α. The descending curves appear as pairs of columns in the matrix, where the rows represent the polarization at the corresponding return field E_r. Depending on the minimum and maximum applied field, the measurement frequency, and limitations of the equipment, E_r may not be spaced at regular intervals, hindering numerical evaluation of the distributions $\rho(E, E_r)$ and $\rho_{rev}(E)$. Therefore, the descending curves were each linearly interpolated to make a matrix of polarization data at regular intervals of E. The resulting matrix was differentiated in E and E_r by using the approximations below to acquire the irreversible and reversible components of the hysteresis, respectively. [48]

$$\rho^{+}_{FORC}(E_r, E) = \frac{1}{2}\frac{P(E_r, E) - P(E_r, E + \Delta E) - P(E_r + \Delta E_r, E) + (E + \Delta E, E_r + \Delta E_r)}{\Delta E_r \Delta E}$$

Equation 5.6

$$\rho_{rev}(E_r) = \frac{1}{2}\frac{P(E_r, E_r) - P(E_r, E + \Delta E)}{\Delta E_r}$$ Equation 5.7

The FORC loops are shown in Fig. 5.15. An asymmetry between the positive and negative saturation of the loops ($+P_{sat}$ and $-P_{sat}$) is evident where the positive saturation is fatter. This indicates that the wiping out property essential to a strict Preisach analysis is not met. [50, 51, 53] This is particularly evident in the 410 nm thick films where it appears that the major loop is approached but not achieved when looking at the positive saturation. The loops appear to be mostly congruent; however, the full loops with different histories but the same extrema were not tested for. The films cannot meet the congruency criteria strictly since the polarization increases even after the field is reversed during the steep switching field region. [48]

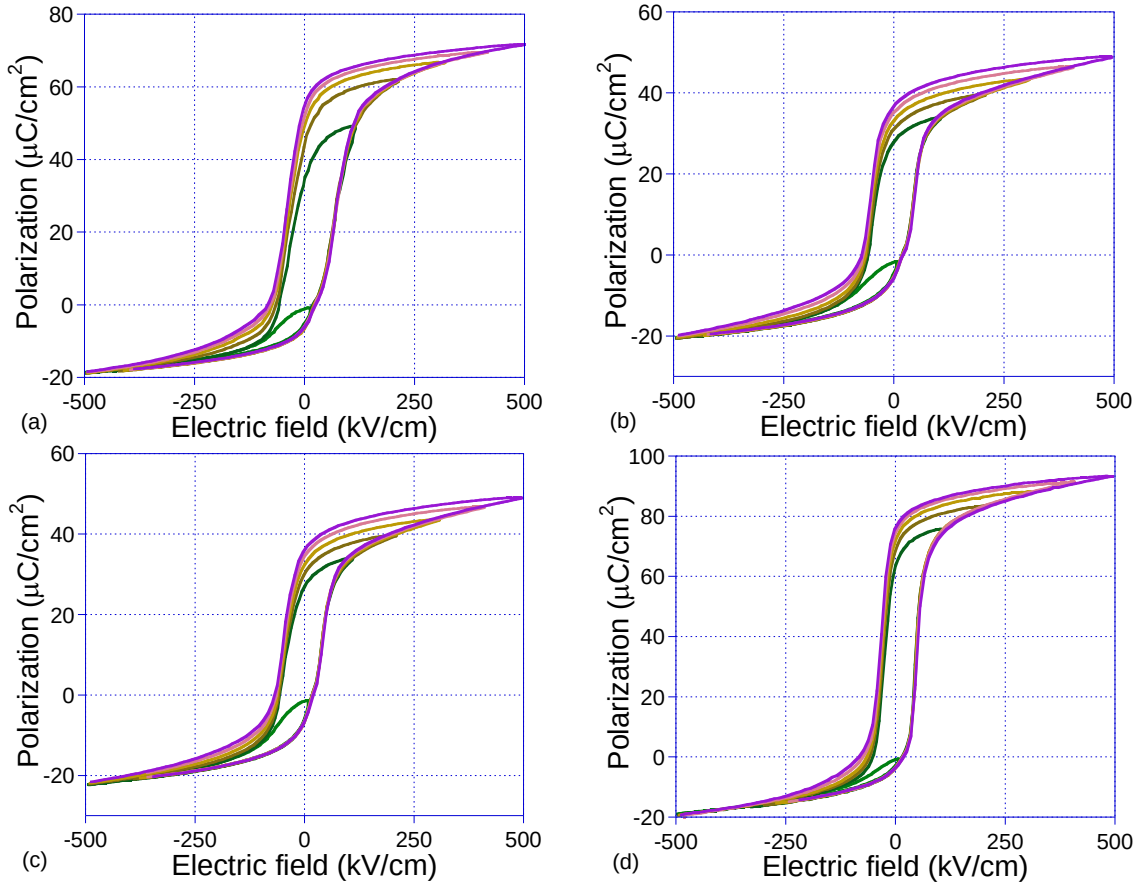

Figure 5.15 – FORCs for films (a) 250 nm, (b) 410 nm, (c) 585 nm, and (d) 990 nm thick. All were crystallized at 725°C except the 990 nm film was crystallized at 750°C and all had the PbO spin casting and annealing treatment.

The FORC distributions for the 725°C films are shown in Fig. 5.16. The distributions became more localized nearer to the origin as the thickness increased. The 250 nm and to a lesser degree 410 nm thick film had switching fields highly distributed in the maximum fields E_r, where the minor loop leaves the major loop. As thickness increased these fields became more localized. Internal, inhomogeneous strain fields as well as electronic defects can be responsible for a broader distribution of switching fields. [185, 186] Porous ferroelectrics which were found to have broadly distributed switching fields have been successfully

modeled by decoupling the dipole interaction during switching, which was argued on the basis of porosity changing the internal mechanical boundary conditions. [187]

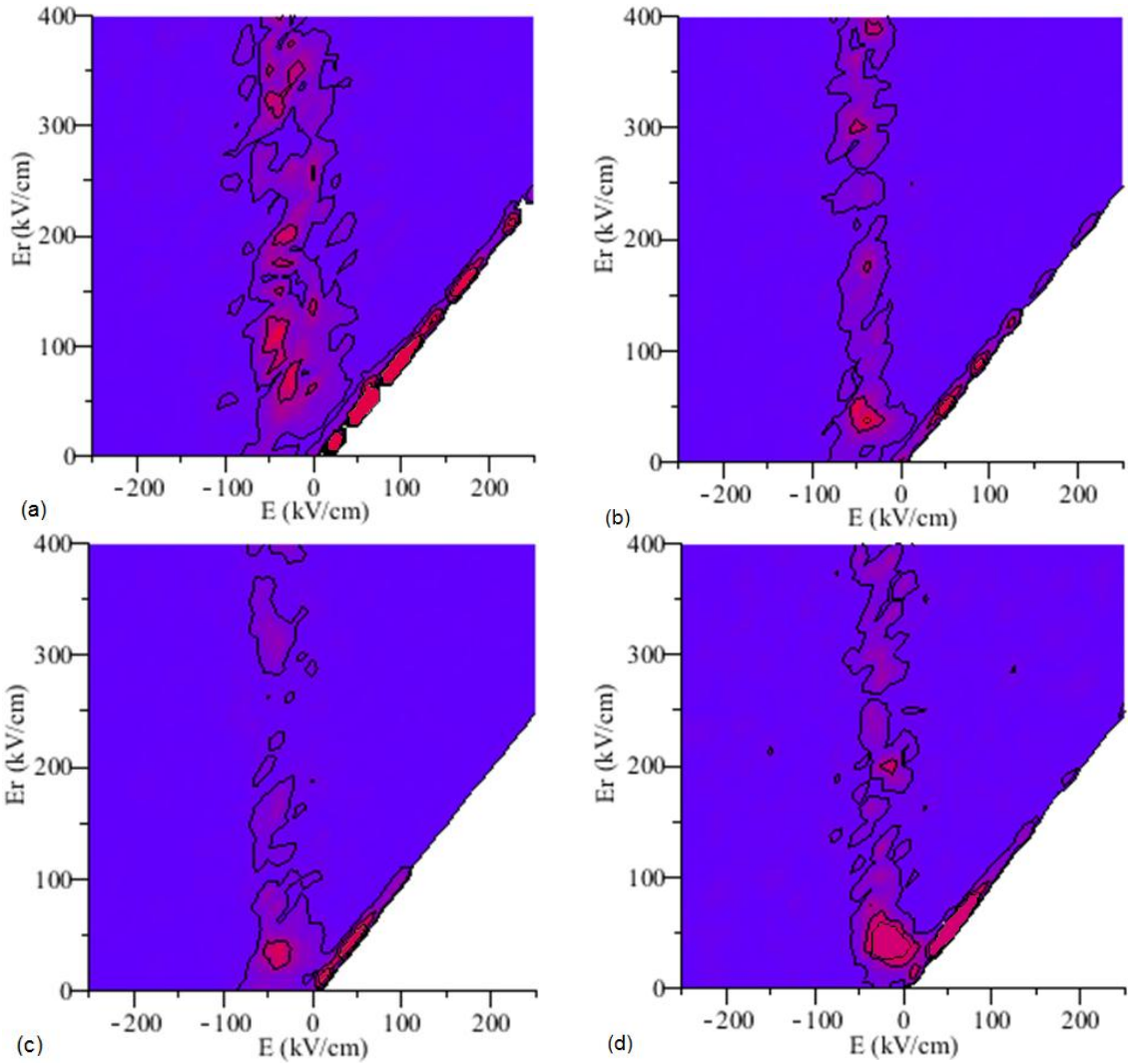

Figure 5.16 – Irreversible FORC distributions for the films in Fig. 5.15. They are (a) 250 nm, (b) 410 nm, (c) 585 nm, and (d) 990 nm thick.

The FORC analysis has been used previously to characterize fatigue in ferroelectric films. [52, 53] The FORC distribution of the 250 nm film appears to have some of the same symptoms of a fatigued film such the broad distribution in switching fields determined by FORC analysis as well as higher E_c. This may be due to defects pinning domains and inhibiting switching since the thinner film might have more defects, particularly when annealed at low pO_2. [188] There is evidence of charge buildup at the interface in the most of the films which caused $+E_c$ to generally be larger than $-E_c$. It was mentioned in chapter 4 that is consistent with a negative charge buildup near the surface, caused by oxygen vacancies.

However, the electronic mechanism of fatigue should lower the remanent polarization by strengthening the depolarization field. [189] Despite this, the 250 nm thick film had a large polarization and remanent polarization overall when compared to the other films. The domains were able to switch their polarization only at higher fields, however, once polarized the polarization tended to remain. The broad FORC distribution coupled with large remanent polarization might point to the elastic residual stress being an important factor. The compressive elastic residual stress may promote a large P_r while generating an inhomogeneous internal strain field which distributes the FORC switching fields. Again, this is supported by the nanoscale switching study of grains compressed by the electrode along the applied field axis. [170]

The same trend could be seen in the irreversible FORC distributions of films crystallized at 550°C and 650°C, where those of the 250 nm thick films were distributed through E_r. There was not much affect of temperature on any of the FORC distributions except on the absolute magnitude of the scale. The FORC distributions did not become broader in a temperature series, but they did as thickness decreased. One exception, only by looking at the hysteresis loops of the 990 nm film crystallized at 650°C, it can be seen that they would have FORC distributions which were dispersed, given their E_c > -100 kV/cm. The likely explanation for that is something other than oxygen vacancies, such as an interfacial reaction, which was indicated by the XRD pattern before the PbO spin casting and annealing treatment.

The reversible FORC distributions were extracted from the FORCs and are plotted in Fig. 5.17. The extrinsic contributions to the dielectric constant are small relative to the total polarization, at high fields. This implies that the only component to the reversible polarization at high fields is the intrinsic one, where domain walls have been driven out of the sample. [184] That the reversible distribution curves converge implies a comparable intrinsic dielectric constant between the samples. [48] This further implies that neither the residual stress, crystallization temperature nor the grain size had a considerable impact on the intrinsic dielectric constant since they all converge to roughly the same point.

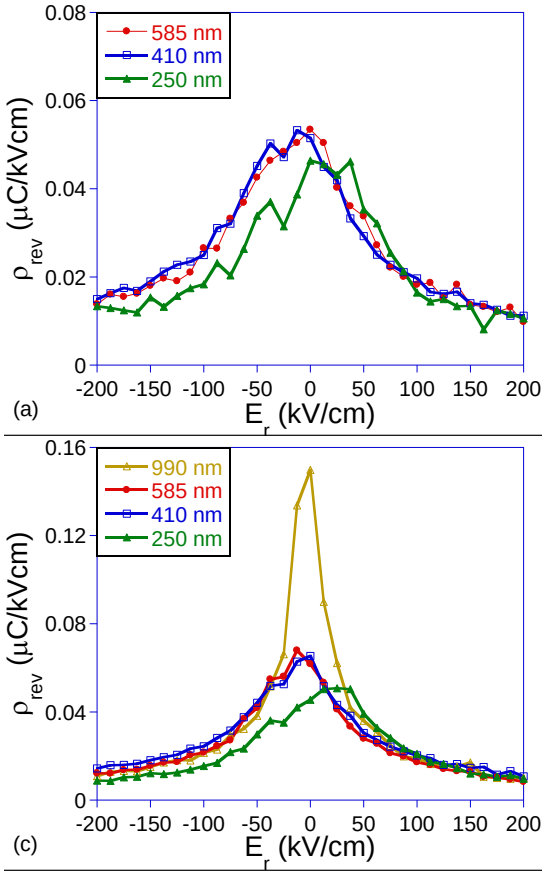

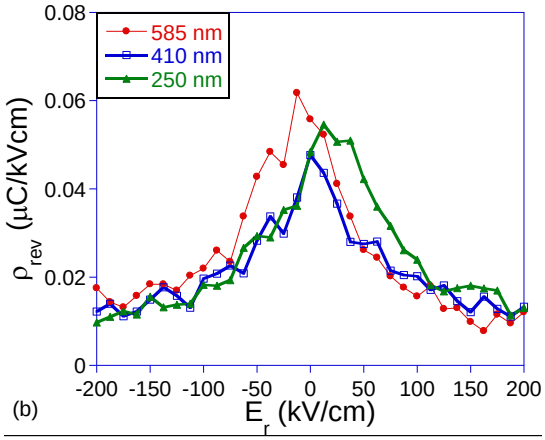

Figure 5.17 – Reversible distribution functions for films crystallized at (a) 550°C, (b) 650°C, and (c) 725°C or 750°C for the 990 nm thick film. The 410 nm and 585 nm films were very similar, but the 250 nm film distributions were consistently shifted to positive fields. The 990 nm film had a large reversible contribution.

5.5 Temperature dependence of the permittivity

The temperature dependence of the dielectric constant may give indications of the stress state of the film. At higher temperatures, the substrate expands more than the film, relieving some of the compressive stress. The effect cannot be definitively decoupled from the typical ferroelectric property of increasing dielectric constant towards the Curie temperature. Fig. 5.18 shows the temperature dependence of the dielectric constant at 1 kHz for several of the

films wrapped in the copper foil envelope during crystallization, which were described just above.

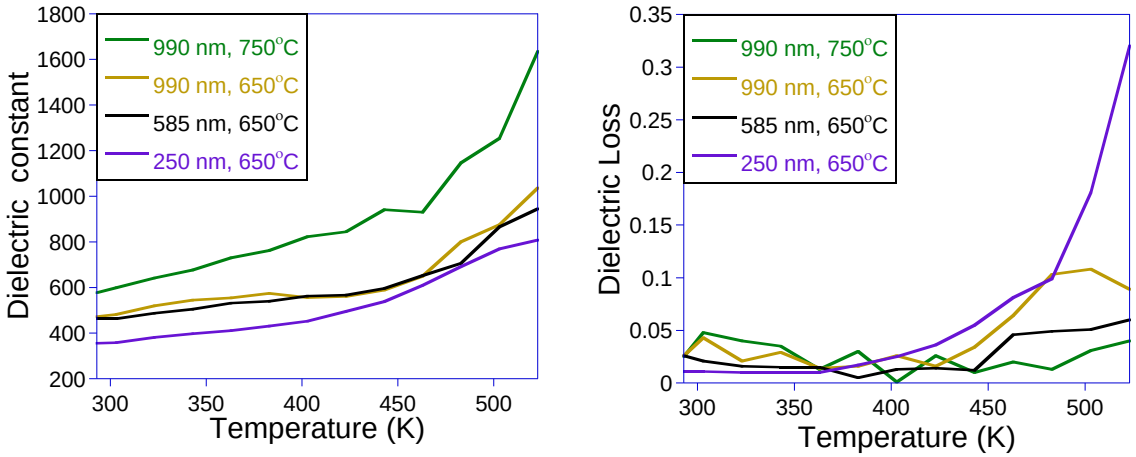

Figure 5.18 – Temperature dependence the dielectric constant and loss for several films wrapped in copper foil during crystallization and annealing under spin coated PbO.

The slope of the dielectric constant versus 1/T was fit to a linear equation for comparison of the slope. The slopes are shown in Table 5.1 for the temperature regions 300 K < T < 400 K and 400 K < T < 500 K. The temperature dependence of the dielectric constant tended to increase with film thickness. The 990 nm film crystallized at 750°C had the highest temperature coefficient for the dielectric constant which was comparable to the literature values for other thin films, in the low temperature region. [63, 190] The slope of the dielectric constant with temperature was roughly the same for the three films crystallized at 650°C, whereas the residual stress was found to decrease from the 250 nm to the 585 nm film. Thus, with the limited information, stress cannot be said to play a role in the temperature coefficient of the dielectric constant. However, the coefficient appears to increase with higher crystallization temperature and film thickness.

Table 5.1 – Slope of the dielectric constant vs. T (K) for low T, 400 K < T < 500 K and high T, 293 < T < 400 K.

Film and conditions	Slope ε_r low T	Slope ε_r high T	ε_r at 293 K
250 nm, 650°C, 1 layer	0.885	3.16	355
585 nm, 650°C, 1 layer	0.936	3.31	463
990 nm, 650°C, 1 layer	0.883	4.07	472
990 nm, 750°C, 1 layer	2.18	6.18	577

5.6 Conclusions and future work

The residual stress could be determined from the $\sin^2\psi$ method using side-inclination (χ) mode. The validity of these results were verified by Stoney's method on a long, thin film. Electrical results from chapter 4 were put into the context of the residual stress measurements.

For future work, it would be nice to have a more accurate view of the stress and texture in the films. The $\sin^2\psi$ method in constant volume mode can be used to separate the effects of strain gradients and texture gradients in the depth of a film. Other useful methods for deconvoluting stress and texture include the Warren-Averbach Fourier analysis and the calculation of an orientation distribution function from pole figures. An x-ray diffraction study of phase transformations induced by residual stress is potentially something that could shed further light on the behavior of the MPB in the stress-temperature-composition space.

The coercive field was found to correlate to residual stress gradient. This was explained in terms of an elastic-mechanical clamping at the substrate interface which increases the energy required to switch 180° domains. The switching of 90° domains is associated with a change in the shape of the material, which might cause a reduction in the residual elastic stress. It would be interesting to see if the effect of 90° domain switching could be seen in the residual stress measurement. If so, could it indicate the extent to which 90° domain switching occurs.

Rayleigh analysis was performed and data extracted about the intrinsic, reversible and irreversible contributions to the dielectric constant. Residual stress was correlated to a decrease in the zero-field dielectric constant, $\varepsilon'_{init}/\varepsilon_0$, while reversible FORC density density plots show that the intrinsic dielectric constant is the same for all films. This implies that the reversible contribution is responsible for the difference between the zero-field dielectric constants.

The FORC analysis as performed here only shows that the 250 nm films are reminiscent of a fatigued film. However, the large P_r suggests that the strain field mechanism is more important to understanding these films than the defect model. It would be much more valuable to fatigue the samples through cycling. Fatigue is usually thought of as a purely electrical segmentation of charge. However, it may be that the high compliance of the substrate has some effect on

the fatigue behavior. The effect of biaxial stress on the fatigue characteristics is something else that could be investigated.

6. Cantilever energy harvesters

One goal of this project was to fabricate cantilevers and demonstrate the direct piezoelectric effect with them, collecting data on the resonant frequency and voltage output. This chapter is divided into two parts with a discussion of the model, based on the Euler-Bernoulli beam theory, followed by the experimental observations.

6.1 Modeling cantilever energy harvesters

The unimorph piezoelectric cantilever operating in d_{31} mode discussed in the introduction was fabricated. In order to verify that the output as measured on the oscilloscope was truly due to the piezoelectric device, the parameters were entered into a model to determine the theoretical resonant frequency and voltage output of the device.

The bending modulus per unit width, *D*, describes the tendency of the material to bend. It depends on the elastic moduli, E_p and E_s, of the piezoelectric and substrate layers as well as their thicknesses, h_i. [191]

$$D = \frac{E_p^2 h_p^4 + E_s^2 h_s^4 + 2E_p E_s h_p h_s (2h_p^2 + 2h_s^2 + 3h_p h_s)}{12(E_p h_p + E_s h_s)} \qquad \text{Equation 6.1}$$

The resonant frequency is the point at which maximum deflection is seen in the beam tip. The resonant frequency of the n^{th} bending mode of the cantilever is f_n, given by

$$f_n = \frac{\nu_n}{2\pi}\frac{1}{L^2}\sqrt{\frac{D}{m}} \qquad \text{Equation 6.2}$$

$$m = \rho_s h_s + \rho_p h_p \qquad \text{Equation 6.3}$$

where ν_n is the n^{th} mode eigenfrequency and m and L are the mass per unit area and length of the cantilever, respectively. The densities are denoted ρ.

For a cantilever beam of uniform cross section (single material) the ν_1, ν_2 and ν_3 are 1.875, 4.694 and 7.855, respectively. [192] However, these may not be accurate values for a real cantilever. The actual surface coverage and geometry of the electrodes, non-uniform substrate thickness, and stresses applied during fabrication and mounting can affect this value. In principle these eigenfrequencies should be obtained experimentally. By measuring the n^{th} mode resonant frequencies of several beams of different lengths we can arrive at a system of equations with only two unknowns that allow us to calculate the desired ν_n and D. [193]

The first three resonant frequencies are plotted in Fig. 6.1 for a 700 nm thick PZT film as a function of cantilever length assuming a 20 μm thick substrate and a 2.5 cm long cantilever. The bulk elastic moduli are assumed to be 120 GPa for copper and 55 GPa for the PZT film. Densities of the copper and PZT are

assumed to be 9000 g/cm^3 and 7600 g/cm^3, respectively. The ideal values for the eigenfrequencies given above are assumed to hold.

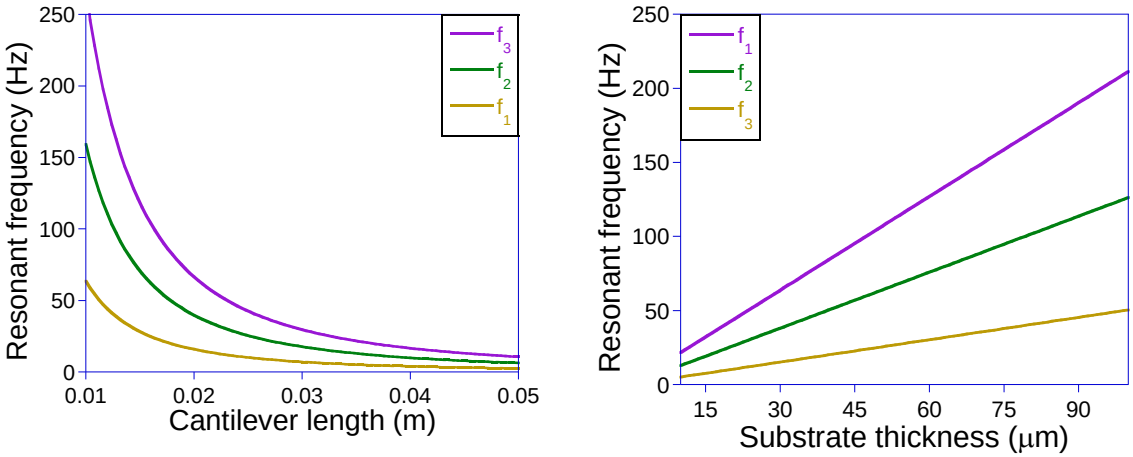

Figure 6.1 – Resonant frequency as a function of cantilever length and copper foil thickness.

The dynamic behavior cantilevers were modeled by the Euler-Bernoulli and piezoelectric constitutive equations as described by Mo. [194] The analytic equation takes time and frequency as variables and computes an output voltage, given material parameters. The radius of curvature of the cantilever, *r*, is determined by analyzing the motion of a unimorph cantilever with a piezoelectric film and non-piezoelectric substrate under an accelerating force.

$$r = \frac{-12 s_s s_p (s_p h_s + s_s h_p) E_c I_c \frac{\partial^2 w}{\partial x^2} + b 6 s_s s_p d_{31} h_p h_s (h_s + h_p) E_3}{bB} \qquad \text{Equation 6.4}$$

where b is the cantilever width and B is a constant given by

$$B = s_s^2 h_p^4 + 4 s_p s_s h_s h_p^3 + 6 s_p s_s h_p^2 h_s^2 + 4 s_p s_s h_p h_s^3 + s_p^2 h_s^4 \qquad \text{Equation 6.5}$$

and where E_c and I_c are the effective elastic modulus and second moment of area of the cantilever. The effective elastic modulus of the cantilever is described by the following equation, using the values obtained here, where E_p and I_p are the values for the piezoelectric layer and E_s and I_s are the values for the substrate. [195]

$$E_c I_c = E_p I_p + E_s I_s \qquad \text{Equation 6.6}$$

The other material parameters are s_p and h_p, and s_s and h_s, the elastic stiffness and thickness of the piezoelectric and substrate, respectively. The electric field across the piezoelectric is E_3 and d_{31} is the piezoelectric coefficient. The deflection of the beam from the neutral axis at any point along its length is $w(x)$ and so the acceleration is $\partial^2 w/\partial w^2$.

The quantity $\partial^2 w/\partial x^2$ can be measured using a high-speed video camera and E_3 can be measured with an oscilloscope. The unknowns in the equation above are the d_{31} and s_p, which is quadratic. By performing the above analysis of the curvature, as well as the resonant frequencies, and then fitting d_{31} and s_p to r, these last two unknowns could theoretically be determined. For the purpose of the model, a d_{31} value of 50×10^{-12} m/V is assumed.

The voltage generated across the device is given by the following equation [194]

$$V_{gen} = \frac{\sum_n -6\frac{s_p s_m d_{31} h_m (h_m + h_p) M_n}{B}}{\frac{\varepsilon_{33} bL}{h_p}\left(1+\left(3\frac{s_m s_p^2 h_p h_m^2 (h_m + h_p)^2}{s_h B} - 1\right)K_{31}^2\right)} \qquad \text{Equation 6.7}$$

where k_{31} is the electromechanical coupling coefficient given by

$$K_{31} = \frac{d_{31}}{\sqrt{\varepsilon_{33} s_p}} \qquad \text{Equation 6.8}$$

and ε_{33} is the dielectric permittivity of the piezoelectric. The bending moment M, given by Eqn. 6.9, is equivalent to the curvature of the cantilever as a function of position and time.

$$M(x,t) = E_c I_c \frac{\partial^2 w(x,t)}{\partial x^2} = \sum_n M_n \qquad \text{Equation 6.9}$$

In the sum M_n denotes the n^{th} bending mode. The bending moment $M(x, t)$ is the sum of the contribution from all of the bending modes. The full equations for the bending moments are not shown here, but rough estimates for the generated voltage can be obtained by using only the first of the bending modes and attributing the entire second derivative of deflection to that mode.

The estimated peak voltage output for the first bending mode, as a function of frequency, is given in Fig. 6.2 for two cantilever energy harvesters on 20 μm and 70 μm thick copper substrates. The parameters used in the model are detailed in Table 6.1, below.

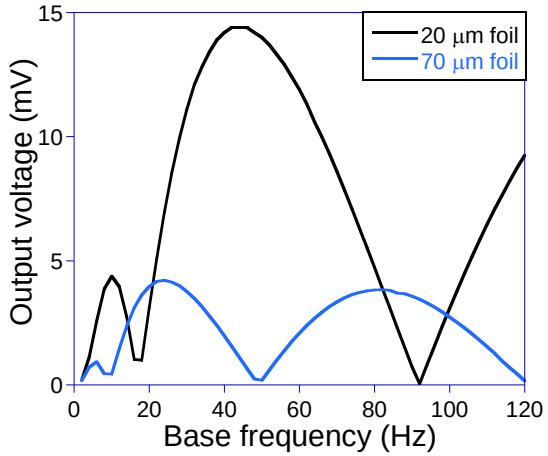

Figure 6.2 – Cantilever energy harvesters with different sets of parameters labeled (a) C1 and (b) C2. The parameters are described in Table 6.1.

Table 6.1 – Important parameters used in the model in Fig. 6.2.

Model parameter	Value
Substrate width (cm)	0.5
Substrate length (cm)	2.5
Piezoelectric thickness (nm)	700
Substrate elastic modulus (GPa)	120
Piezo elastic modulus (GPa)	55
Piezoelectric coefficient d_{31} (m/V)	50×10^{-12}
Dielectric permittivity ε_{33} (F/m)	4.43×10^{-9}
Base excitation amplitude (cm)	0.25
Damping coefficient	0.025

6.2 A note on electrode yield

The first and most difficult problem that was faced in fabricating PZT/Cu cantilevers was in getting a decent electrode yield. The maximum operating frequency of our test bench was approximately 100 Hz. The cantilevers were also found to undergo deformation at base excitation amplitudes larger than 0.25 cm at frequencies higher than about 50 Hz. It can be seen in the plots of frequency in section 6.1, in order to fabricate cantilevers which could be tested at less than 50 Hz it was necessary to make them 2 cm long and 0.25 cm wide, or 0.5 cm^2. As it were, the largest electrodes that we could make on films without Cu_2O, and achieve good yield were about 0.01 cm^2. When Cu_2O was present the electrode yield was better since the Cu_2O provided large total resistance on small area pinholes and micron scale cracks. However, the quality of the films was poor and the yield was still not good, less than 10% for the desired size.

In order to produce a higher yield, it was necessary to heat the crystallized films on a hot plate at 325°C for several hours prior to electrode deposition. Most likely this treatment oxidizes copper exposed through pinholes and cracks. The electrode yield came close to 75%. The procedure also unavoidably oxidizes the exposed bottom side of the bottom electrode. Oxide was then removed from a small area on the bottom electrode for the electrical connection to the oscilloscope. An alternative for future experimentation would be to make bimorph

cantilevers, which would produce a larger signal, as well as preventing oxidation of the copper surface.

6.3 Experimental results

The cantilever energy harvester test bench is shown in below, in Fig. 6.3.

Figure 6.3 – Cantilever energy harvester test bench.

A custom Teflon bracket was fitted onto a shaker table (K2007E01, The Modal Shop, Inc.). The shaker table is capable of operating up to around 100 Hz safely and has three amplitude settings: 0.25 cm, 0.5 cm and 1 cm. The bracket held screws which touched contacts inside the bracket and also clamped the cantilever. Two leads from the screws went directly to the oscilloscope. The single wire leads were made as short as possible before entering the coaxial cable to limit electromagnetic noise from the shaker table. The shaker table was

driven by a sinusoidal signal from a function generator at the desired frequency and ~5 V (Simpson 420).

The fabricated cantilever resonant frequencies and output voltages were found to be a very good match to the model. However, the overall shape of the output was somewhat unusual in that they were sometimes asymmetric, resonant peaks were sharper than the model, and small peaks appeared near the expected first resonance. There are three explanations, all of which likely contribute something to the observed difference. The actual damping factor is unknown; the damping factor will have more of an effect for larger accelerations. After approximately 50 Hz, most of the samples deformed somewhere in the middle due to the accelerating force which made continued measurement pointless. Finally, the shape of the cantilevers is imperfect and does not exactly match the profile of the uniform cross sectional beam assumed by the Euler-Bernoulli equations. A side-profile of the cantilever under magnification is shown in Fig. 6.4.

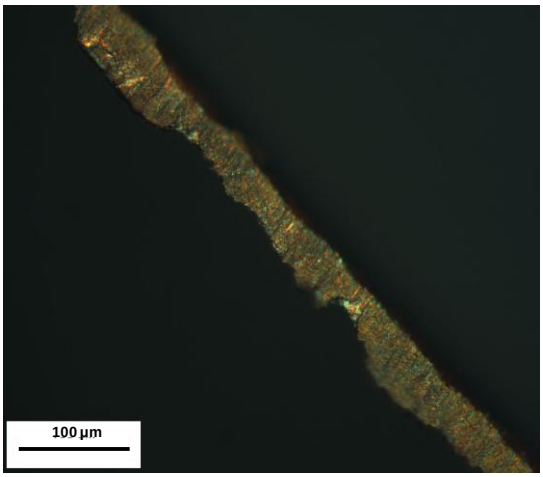

Figure 6.4 – Side profile of a cantilever which was 50 µm before polishing.

Despite some shortcomings, the experiment did match the model in some respects. For instance, the resonant frequency Eqn. 6.2 predicts for first and second resonant frequencies is 16 Hz and 40 Hz, respectively for a 20 µm thick foil. The dynamic model predicts resonances at 10 Hz and 45 Hz. The behavior of a cantilever fabricated from 25 µm thick copper foil (before polishing) is shown in Fig. 6.5 showing resonances at approximately 17 Hz and 35 Hz, which is in general agreement with the calculated resonances.

The dynamic model predicts peak voltages to be 4.4 mV and 14.4 mV. The experimentally obtained outputs are 2.5 mV and 7.1 mV, which are proportional to the expected outputs, though the magnitude halved. However, the absolute magnitude of the output predicted from the model is very sensitive to the damping coefficient and the piezoelectric coefficients, both of which are unknown.

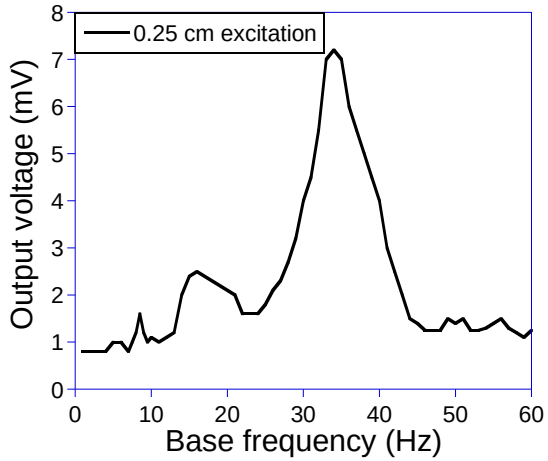

Figure 6.5 – Cantilever voltage output was occasionally well behaved.

In the model the output voltage is proportional to the base excitation amplitude, and hence the acceleration, when the damping is minimal. In Fig. 6.6, plots of the output voltage with frequency for two base amplitudes show this behavior. The unique shape of the outputs matches very well. There is a shoulder to the right of the main resonance which is repeated identically in both. This shoulder is likely due to some deformation which moves the cantilever away from a truly uniform beam, but the output is approximately doubled from the 0.25 cm to the 0.5 cm excitation over the entire range.

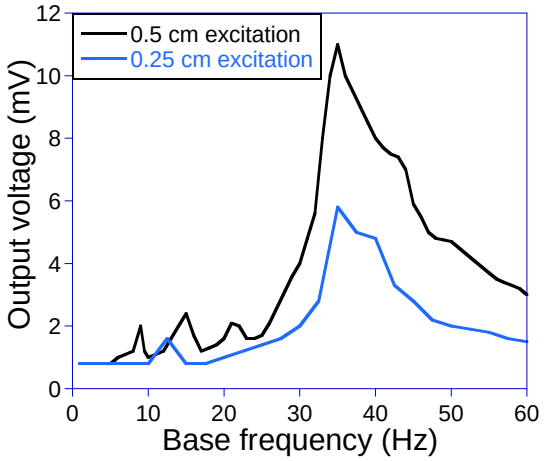

Figure 6.6 – Effect of base excitation amplitude on output voltage.

Increasing the amplitude occasionally caused mechanical failure of the cantilever. This did not usually happen at low amplitude (0.25 cm travel), but did at the intermediate amplitude (0.5 cm travel). The effect of this is shown in Fig. 6.7 where the cantilever was first tested at low and then intermediate amplitude.

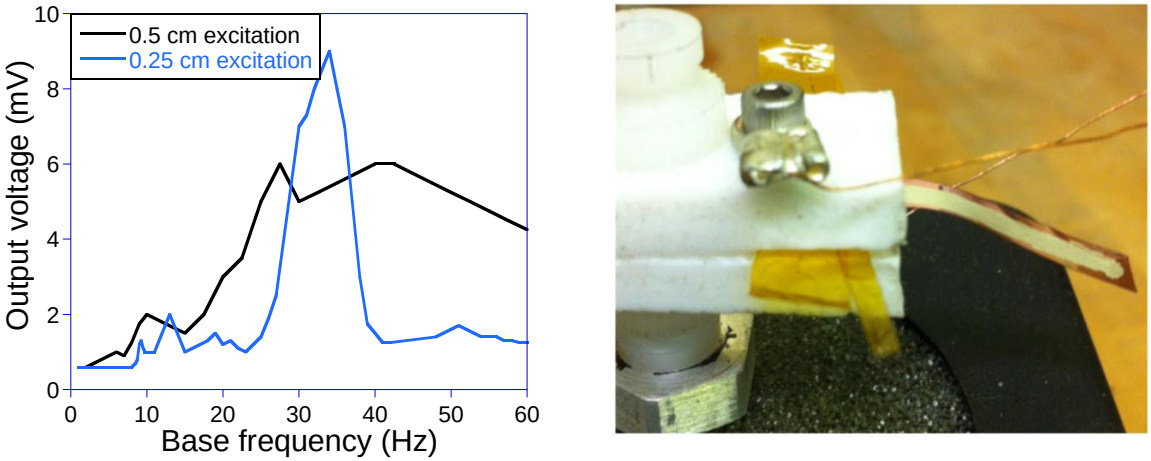

Figure 6.7 – Mechanical breakdown occurred at medium base excitation amplitude in some cantilevers. The deformed cantilever is shown at right.

At low amplitude the film showed the expected small output resonance at 12 Hz and then the large one at 35 Hz. When the cantilever was then driven by a 0.5 cm base excitation a failure occurred just after 25 Hz. When the shaker table was stopped it could be seen that the cantilever was bent down and deformed with some undulations along its length.

6.4 Conclusions and future work

The cantilevers were found to perform similar to that expected from the model. The resonant frequency matched well to the resonances calculated from the standard beam equation and the dynamic model. The output voltages for the first and second resonance fit the dynamic model qualitatively but not quantitatively, being smaller by a half to a third. The reason was that piezoelectric coefficient and the damping coefficient had to be assumed. Also the beam profile deviated from the ideal geometry which could have resulted in a reduced action at resonance.

Large amplitude vibrations tended to deform the substrate, causing permanent kinks which cause unpredictable operation. It is possible that a more uniform substrate or an improved mounting system would allow make the measurement more robust. Also, much more work needs to be done in order to improve the electrode yield without a post crystallization pinhole oxidizing heat treatment

step. If the heat treatment cannot be avoided then a bimorph cantilever arrangement would be preferred.

7. Conclusions

The conclusions and future work were summarized at the end of each chapter. These are summarized below.

Chapter 4. Properties of sputtered PZT thin films on copper foils

i. Cuprous oxide was characterized by XPS, XRD and cross sectional SEM. The increased formation of cuprous oxide was correlated to the increasing film thickness and decreasing temperature. This suggests an interfacial reaction between the PZT film and the copper foil substrate.

ii. The formation of cuprous oxide was prevented by wrapping the films in a copper foil envelope during crystallization. In cases where cuprous oxide or second phases formed despite the use of an envelope (ie when crystallizing thicker films at lower temperatures), it could be reversed by further annealing under a spin cast PbO layer without a loss of properties.

iii. It would be beneficial to determine the actual defect(s) responsible for the relaxation in PZT/Cu films with cuprous oxide, and conduction in films with and without cuprous oxide. Leakage current measurements must be carried out at varying levels of pO_2 and temperature. This experiment could also yield the dominant conduction mechanism in each type of film.

iv. The effect of depositing and crystallizing layer by layer, introducing oxygen during sputtering, and changing Ar sputter pressure and sputter power

should be explored in greater detail using the technique of the copper envelope to avoid oxidation of the substrate.

v. An interesting experiment would be to attempt an ozone reoxidation or a UV light assisted recovery under a poling field. Films show indications of oxygen deficiency and internal fields which are characteristic of fatigued films. It is possible that one or both of these techniques could improve the properties of these films.

vi. The samples should be fatigued in order to substantiate their ability to work in real world applications.

Chapter 5. Extrinsic contributions to polarization

i. Residual stress was determined from $\sin^2\psi$ measurements in side-inclination (χ) mode and values were compared to long cantilevers whose residual stress was measured using Stoney's equation.

ii. Signs of either stress gradients or a small degree of anisotropy were detected. In order to characterize the stress accurately a Warren-Averbach analysis should be performed or the orientation distribution function computed using pole figures.

iii. The coercive field was correlated to the residual stress. However, further measurements should be done to deconvolute the effect of film thickness since this also is correlated to residual stress.

iv. Rayleigh analysis was performed. At the higher temperature (725°C) the Rayleigh parameter was strongly dependent on film thickness, but less so

at the lower temperatures. The reversible part of the dielectric constant was found to be correlated directly to the parameter $\sigma_{residual}$ x film thickness, which is thought of as a surface energy. Further measurements should be made to verify this result.

v. First order reversal curves (FORCs) were measured and used to characterize the effects of defects on switching. It was found that as the film thickness decreased, the irreversible switching density spread across the Preisach plane, resembling a fatigued film. The FORC obtained reversible switching component indicates that the intrinsic part (not associated with domain walls) of the dielectric constant was relatively constant across all films. Further testing should be performed on fatigued PZT/Cu films.

vi. The temperature coefficient of the dielectric constant was found to increase with increasing film thickness. This could not be connected directly to the residual stress although such a comparison was attempted. Testing of more samples is required.

Chapter 6. Cantilevers

i. PZT/Cu cantilevers were fabricated. Pinholes and cracks, which otherwise would short the electrodes, are suspected to be oxidized on a hot plate and the technique provides good yield.

ii. The observed resonant frequencies a good match for the calculated values and the output voltage was of the same order as modeled by a

dynamic time-based model. Differences can be attributed to uncertainty in the film properties and non-idealities of the electrode-film-electrode stack geometry.

iii. Cantilevers were susceptible to deformation at medium-high vibration amplitudes as the frequency increased above ~50 Hz. Deformation caused a broadening and general decrease of the output voltage.

iv. The cantilevers should be made of varying substrate thickness and length and PZT thickness. By varying these parameters and observing the resonant frequencies and output voltages some of the unknown model parameters can be determined. These include the effective elastic moduli of the film and substrate and possibly the piezoelectric and damping coefficients.

References

1. Piticescu, R.M., et al., *Preparation and characterisation of $Pb(Zr_{0.52}Ti_{0.48})_{0.975}Nb_{0.025}O_3$ ceramics modelling the device.* Journal of The European Ceramic Society, 2005. **25**(12): p. 2491-2494.

2. Muralt, P., *PZT thin films for microsensors and actuators: Where do we stand?* IEEE transactions on ultrasonics, ferroelectrics and frequency control, 2000. **47**(4): p. 903-915.

3. Gebhardt, S., et al., *PZT thick films for sensor and actuator applications.* Journal of The European Ceramic Society, 2007. **27**(13-15): p. 4177-4180.

4. Kiyohara, M., et al., *Actuator characteristics of $Pb(ZrTi)O_3$ composition near morphotropic phase boundary.* Japanese Journal of Applied Physics, 1991. **30**: p. 2264-2266.

5. Randall, M., et al. *Thin Film MLCC, Assemblies & Materials Association*. in *CARTS 2007 Symposium Proceedings*. 2007. Arlington, VA: Electronic Components, Assemblies & Materials Association.

6. Imamiya, Y., et al., *Multilayer thin-film capacitors fabricated by redio-frequency magnetron sputtering*, in *2011 International Symposium on Piezoresponse Force Microscopy and Nanoscale Phenomena in Polar Materials*2011, IEEE: Vancouver, Canada.

7. Choi, W.S., et al., *Characterization of $Ba(Zr_{0.2}Ti_{0.8})O_3$ thin films deposited by rf-magnetron sputtering.* Journal of Crystal Growth, 2002. **237-239**: p. 438-442.

8. Yang, G., et al., *Dielectric responses of modified $BaTiO_3$ ceramics in multilayer ceramic capacitors to the combined uniaxial stress and dc bias field.* Journal of Applied Physics, 2008. **104**.

9. Losego, M.D., et al., *Ferroelectric Response from Lead Zirconate Titanate Thin Films Prepared Directly on Low-Resistivity Copper Substrates.* Applied Physics Letters, 2005. **86**.

10. Kingon, A.I. and S. Srinivasan, *Lead Zirconate Titanate Thin Films Directly on Copper Electrodes for Ferroelectric, Dielectric and Piezoelectric Applications.* Nature Materials, 2005. **4**: p. 233-237.

11. Suchaneck, G., et al., *Deposition of PZT Thin Film onto Copper-Coated Polymer Films by Mean of Pulsed-DC and RF-Reactive Sputtering.* Surface Coatings and Technology, 2011. **205**: p. S241-S244.

12. Suchaneck, G., et al. *Recrystallization of the Copper Bottom Electrode During Complex Oxide Deposition onto Kapton Films*. in *18th IEEE International Symposium on Applications of Ferroelectrics*. 2009.

13. He, X.-Y., et al., *Preparation of PZT(53/47) thick films deposited by a dip-coating process.* Microelectronic Engineering, 2003. **66**(1-4): p. 865-871.

14. Gentry, K.L., et al., *Thick film sol gel PZT transducer using dip coating.* IEEE Ultrasonics Symposium, 2000. **2**: p. 977-980.

15. Bronson, J.R., et al. *PZT mems actuated flapping wings for insect-inspired robotics*. in *IEEE 22nd International Conference on MEMS 2009*. 2009. IEEE.

16. Polcawich, R.G., et al. *Advances in Piezoelectrically Actuated RF MEMS Switches and PhaseShifters*. in *Microwave Symposium, 2007. IEEE/MTT-S International*. 2007.

17. Proie, R.M.J., et al., *Development of a PZT MEMS Switch Architecture for Low-Power Digital Applications.* Journal of Microelectromechanical Systems, 2011. **20**(4).

18. Sakabe, Y., *Multilayer Ceramic Capacitors.* Current Opinion in Solid State & Materials Science, 1997. **2**: p. 584-587.

19. Smay, J.E., S.S. Nadkarni, and J. Xue, *Direct Writing of Dielectric Ceramics and Base Metal Electrodes.* International Journal of Applied Ceramics Technology, 2007. **4**: p. 47-52.

20. Kishi, H., Y. Mizuno, and H. Chazono, *Base-Metal Electrode-Multilayer Ceramic Capacitors: Past, Present and Future Perspectives.* Japanese Journal of Applied Physics, 2003. **42**: p. 1-15.

21. Liu, D.D. and M.J. Sampson. *Reliability Evaluation of Base-Metal-Electrode Multilayer Ceramic Capacitors for Potential Space Applications*. in *CARTS USA*. 2011. Jacksonville, FL: Electronic Components Association.

22. Kahn, M., *Multilayer Ceramic Capacitors–Materials and Manufacture*, 2004, AVX Corp: Myrtle Beach, SC.

23. Curie, J. and P. Curie, *Development by Pressure of polar electricity of hemihedral crystals with inclined faces.* Bulletin de la Societe Mineralogie de France, 1880. **3**: p. 90-102.

24. Cross, L.E. and R.E. Newnham, *History of Ferroelectrics, Ceramics and Civilization, Vol. III, High Technology Ceramics-Past, Present and Future*. 1987: The American Ceramic Society.

25. Spaldin, N., *Analogies and Differences between Ferroelectrics and Ferromagnets*, in *Physics of Ferroelectrics: A Modern Perspective*, K.M. Rabe, C.H. Ahn, and J.-M. Triscone, Editors. 2007, Springer.

26. Moulson, A.J. and J.M. Herbert, *Electroceramics*. 2003: Wiley.

27. Noheda, B., et al., *Tilts and Ionic Shifts in Rhombohedral Perovskites.* Journal of the Korean Physical Society, 1998. **32**: p. S162-S164.

28. Fanning, D.M., et al. *Antiferroelectric to Paraelectric Phase Transition in Lead Zirconate Thin Films*. in *MRS Fall Meeting*. 1998. Boston, MA: Materials Research Society.

29. Chen, H.D., et al., *Electrical Properties' Maxima in Thin Films of the Lead Zirconate-Lead Titanate Solid Solution System.* Applied Physics Letters, 1995. **67**.

30. Noheda, B., et al., *A Monoclinic Ferroelectric Phase in the $Pb(Zr_{1-x}Ti_x)O_3$ Solid Solution.* Applied Physics Letters, 1999. **74**.

31. Noheda, B., et al., *Tetragonal-to-Monoclinic Phase Transition in a Ferroelectric Perovskite: The Structure of $PbZr_{0.52}Ti_{0.48}O_3$.* Physics Review B, 2000. **61**(13): p. 8687-8695.

32. Durbin, M.K., et al., *X-ray Diffraction and Phenomenological Studies of the Engineered Monoclinic Crystal Domains in Single Crystal Relaxor Ferroelectrics.* Journal of Applied Physics, 2000. **87**(11): p. 8159-8164.

33. Kuroiwa, Y., S. Aoyagi, and A. Sawada, *Evidence for Pb-O Covalency in Tetragonal $PbTiO_3$.* Physical Review Letters, 2001. **87**(21).

34. Afanasjev, V.P., et al., *Polarization and Self-polarization in Thin $PbZr_{1-x}Ti_xO_3$ (PZT) Films.* Journal of Physics: Condensed Matter, 2001. **13**: p. 8755-8763.

35. Tagantsev, A.K., et al., *Non-Kolmogorov-Avrami Switching Kinetics in Ferroelectric Thin Films.* Physical Review B, 2002. **66**.

36. Bintachitt, P., et al., *Collective dynamics underpins Rayleigh behavior in disordered polycrystalline ferroelectrics.* PNAS, 2010. **107**(16): p. 7219-7224.

37. Bassiri-Gharb, N., et al., *Domain wall contributions to the properties of piezoelectric thin films.* Journal of Electroceramics, 2007. **19**: p. 47-65.

38. Chae, B.G., et al., *Comparative analysis for the crystalline and ferroelectric properties of $Pb(Zr,Ti)O_3$ thin films deposited on metallic $LaNiO_3$ and Pt electrodes.* Thin Solid Films, 2002. **410**: p. 107-113.

39. Viola, G., et al., *Effect of composition on rate dependence of ferroelastic/ferroelectric switching in perovskit ceramics.* Materials Science and Technology, 2009. **25**(11): p. 1312-1315.

40. Stewart, M., M.G. Cain, and D.A. Hall, *Ferroelectric hysteresis measurement & analysis*, in *NPL Report CMMT(A) 152*1999, National Physics Laboratory: Teddington, Middlesex, United Kingdom.

41. Damjanovic, D., *Stress and frequency dependence of the direct piezoelectric effect in ferroelectric ceramics.* Journal of Applied Physics, 1997. **82**.

42. Eitel, R.E., *Rayleigh law response in ferroelectric ceramics: Quantifying domain wall dynamics and structural relationships*, in *Sixteenth IEEE International Symposium on Applications of Ferroelectrics*2007, IEEE. p. 319-323.

43. Robels, U. and G. Arlt, *Domain wall clamping in ferroelectrics by orientation of defects.* Journal of Applied Physics, 1993. **73**.

44. Damjanovic, D. and M. Demartin, *Contribution of the irreversible displacement of domain walls to the piezoelectric effect in barium titanate and lead zirconate titanate ceramics.* Journal of Physics: Condensed Matter, 1997. **9**.

45. Garcia, J.E., R. Perez, and A. Albareda, *Contribution of reversible processes to the non-linear dielectric response in hard lead zirconate titanate ceramics.* Journal of Physics: Condensed Matter, 2005. **17**.

46. Perez, R., et al., *Extrinsic contribution to the non-linearity in a PZT disc.* Journal of Physics D: Applied Physics, 2004. **37**.

47. Kighelman, Z., et al., *Properties of ferroelectric $PbTiO_3$ thin films.* Journal of Applied Physics, 2002. **91**: p. 1495.

48. Fujii, I., E. Hong, and S. Trolier-McKinstry, *Thickness dependence of dielectric nonlinearity of lead zirconate Titanate films.* IEEE transactions on ultrasonics, ferroelectrics and frequency control, 2010. **57**(8): p. 1717-1723.

49. Robert, G., et al., *Preisach modeling of piezoelectric nonlinearity in ferroelectric ceramics.* Journal of Applied Physics, 2001. **89**.

50. Mayergoyz, I.D., *Hysteresis models from the mathematical and control theory points of view.* Journal of Applied Physics, 1985. **57**.

51. Mayergoyz, I.D., *Mathematical Models of Hysteresis and Their Applications*. 2003: Elsevier Science.

52. Cima, L., E. Laboure, and P. Muralt, *Characterization and model of ferroelectrics based on experimental Preisach density.* Review of Scientific Instruments, 2002. **73**(10).

53. Stancu, A., et al., *First-order reversal curves diagrams for the characterization of ferroelectric switching.* Applied Physics Letters, 2003. **83**.

54. Robert, G., D. Damjanovic, and N. Setter, *Preisach distribution function approach to piezoelectric nonlinearity and hysteresis.* Journal of Applied Physics, 2001. **90**.

55. Cheng, J. and Z. Meng, *Thickness-dependent Microstructures and Electrical Properties of PZT Films Derived from Sol-gel Process.* Thin Solid Films, 2001. **385**: p. 5-10.

56. Muralt, P., *Ferroelectric thin films for micro-sensors and actuators: A review.* Journal of Micromechanical Microengineering, 2000. **10**: p. 136-146.

57. Mori, Z., et al., *Growth of bi-axially textured $Bi_2Sr_2Ca_1Cu_2O_{8+d}$ (2212) thin films on $SrTiO_3$ substrate by sputtering method.* Physica C, 2008. **468**: p. 1060-1063.

58. Theis, C.D., et al., *Adsorption-controlled growth of $PbTiO_3$ by reactive molecular beam epitaxy.* Thin Solid Films, 1998. **325**: p. 107-114.

59. Wu, J.Z., et al., *Epitaxial growth of $HgBa_2CaCu_20_{6+\delta}$ thin films on $SrTiO_3$ substrates.* Physica C, 1997. **277**: p. 219-224.

60. Bose, A., et al., *Influence of Plasma Pressure on the Growth Characteristics and Ferroelectric Properties of Sputter-Deposited PZT Thin Films.* Applied Surface Science, 2010. **256**: p. 6205-6212.

61. Thomas, R., et al., *Influence of Sputtering and Annealing Conditions on the Structure and Ferroelectric Properties of $Pb(Zr,Ti)O_3$ Thin Films Prepared by RF Magnetron Sputtering.* Japanese Journal of Applied Physics, 2001. **40**: p. 5511-5517.

62. Torii, K., et al., *Single-Target Sputtering Process for Lead Zirconate Titanate Thin Films with Precise Composition Control.* Journal of Applied Physics, 1991. **30**(12B): p. 3562-3566.

63. Wolf, R.A. and S. Trolier-McKinstry, *Temperature dependence of the piezoelectric response in lead zirconate titanate films.* Journal of Applied Physics, 2004. **95**(3).

64. Es-Souni, M., et al., *Crystallization kinetics and dielectric properties of solution deposited, La doped PZT thin films.* Materials Science and Engineering, 2002. **B94**: p. 229-236.

65. Malič, B., et al., *Crystallization Study of the Alkoxide-Based $Pb(Zr_{0.30}Ti_{0.70})O_3$ Thin-Film Precursor.* Acta Chimica Slovenica, 2005. **52**: p. 259-263.

66. Kang, M.-G., K.-T. Kim, and C.-I. Kim, *Plasma-induced damage in PZT thin films etched by inductively coupled plasma.* Thin Solid Films, 2003. **435**: p. 222-226.

67. Ahn, W.S., W.W. Jung, and S.K. Choi, *Ferroelectric properties and fatigue behavior of heteroepitaxial $PbZr_{1-x}Ti_xO_3$ thin film fabricated by hydrothermal epitaxy below Curie temperature.* Journal of Applied Physics, 2006. **99**.

68. Warren, W.L., et al., *Polarization Suppression in $Pb(Zr,Ti)O_3$ Thin Films.* Journal of Applied Physics, 1995. **77**.

69. Pike, G.E., et al., *Voltage Offsets in $(Pb,La)(Zr,Ti)O_3$ Thin Films.* Applied Physics Letters, 1995. **66**.

70. Brennecka, G.L., et al., *Reversibility of the Perovskite-to-Flourite Phase Transformation in Lead-Based Thin and Ultrathin Films.* Advanced Materials, 2008. **20**(8): p. 1407-1411.

71. Bi, Z., Z. Zhang, and P. Fan, *Characterization of PZT Ferroelectric Thin Films by RF-magnetron Sputtering.* Journal of Physics: Conference Series, 2007. **61**: p. 120-124.

72. Velu, G., D. Remiens, and B. Thierry, *Ferroelectric Properties of PZT Thin Films Prepared by Sputtering with Stoichiometric Single Oxide Target: Comparison Between Conventional and Rapid Thermal Annealing.* Journal of The European Ceramic Society, 1997. **17**(14): p. 1749-1755.

73. Bharadwaja, S.S.N., T. Dechakupt, and S. Trolier-McKinstry, *Laser Crystallized $(Pb,La)(Zr,Ti)O_3$ Thin Films.* Journal of the American Ceramic Society, 2008. **91**(5): p. 1580-1585.

74. Bharadwaja, S.S.N., et al., *Highly Textured Laser Annealed $Pb(Zr_{0.52},Ti_{0.48})O_3$ Thin Films.* Applied Physics Letters, 2011. **99**.

75. Bhaskar, A., et al., *Effect of Microwave Annealing Temperatures on Lead Zirconate Titanate Thin Films.* Nanotechnology, 2007. **18**.

76. Amanuma, K., et al., *Ferroelectric Properties of Sol-Gel Derived $Pb(Zr,Ti)O_3$ Thin Films.* Japanese Journal of Applied Physics, 1993. **32**: p. 4150-4153.

77. Takatani, S., et al., *Pt/$PbZr_xTi_{1-x}O_3$ Interfacial Reaction and Schottkey Barrier Formation Studied by X-ray Photoelectron Spectroscopy: Effect of H_2 and O_2 Annealing.* Journal of Applied Physics, 1999. **85**(11).

78. Wu, A., et al., *Microstructural Studies of PZT Thick Films on Cu Foils.* Acta Materiala, 2006. **54**: p. 3211-3220.

79. Yang, W.-Y., W.-G. Kim, and S.-W. Rhee, *Radio Frequency Sputter Deposition of Single Phase Cuprous Oxide Using Cu_2O as a Target Material and its Resistive Switching Properties.* Thin Solid Films, 2008. **517**: p. 967-971.

80. Chen, F., et al., *Reduction-Induced Fermi Level Pinning at the Interfaces between $Pb(Zr,Ti)O_3$ and Pt, Cu and Ag Metal Electrodes.* Journal of Physics D: Applied Physics, 2011. **44**.

81. Chen, Y. and P.C. McIntyre, *Effects of Chemical Stability of Platinum/Lead Zirconate Titanate and Iridium Oxide/Lead Zirconate Titanate Interfaces on Ferroelectric Thin Film Switching Reliability.* Applied Physics Letters, 2007. **91**: p. 232906.

82. Boukamp, B.A. and D.H.A. Blank, *High-Precision Impedance Spectroscopy: A Strategy Demonstrated On PZT.* IEEE Transactions on Ultrasonics, Ferroelectrics, and Frequency Control, 2011. **58**(12): p. 2521-2530.

83. Boukamp, B.A., et al., *Ionic And Electronic Conductivity In Lead–Zirconate–Titanate (PZT).* Solid State Ionics, 2004. **170**: p. 239-254.

84. Dietz, G.W. and R. Waser, *Charge injection in $SrTiO_3$ thin films.* Thin Solid Films, 1997. **299**: p. 53-58.

85. Juan, T.P.-C., S.M. Chen, and J.Y.-M. Lee, *Temperature Dependence Of The Current Conduction Mechanisms In Ferroelectric $Pb(Zr_{0.53},Ti_{0.47})O_3$ Thin Films.* Journal of Applied Physics, 2004. **95**.

86. Dietz, G.W., et al., *Leakage currents in $Ba_{0.7}Sr_{0.3}TiO_3$ thin films for ultrahigh-density dynamic random access memories.* Journal of Applied Physics, 1997. **82**.

87. Chen, H.-M. and J.Y.-M. Lee, *The temperature dependence of the transient current in ferroelectric $Pb(Zr_xTi_{1-x})O_3$ thin films for memory devices applications.* Journal of Applied Physics, 1997. **82**.

88. Scott, J.F., *High-dielectric constant thin films for dynamic random access memories (DRAM).* Annual Revue of Material Science, 1998. **28**: p. 79-100.

89. Chentir, M.T., et al., *Leakage current evolution versus dielectric thickness in lead zirconate titanate thin film capacitors.* Journal of Applied Physics, 2009. **105**.

90. Masuda, Y. and T. Nozaka, *Investigation into Electrical Conduction Mechanisms of Pb(Zr,Ti)O_3 Thin-Film Capacitors with Pt, IrO_2 and $SrRuO_3$ Top Electrodes.* Japanese Journal of Applied Physics, 2004. **43**: p. 6576-6580.

91. Rose, A., *Space-Charge-Limited Currents in Solids.* Physical Review, 1955. **97**(6): p. 1538-1544.

92. Lampert, M.A., *Simplified Theory of Space-Charge-Limited Currents in an Insulator with Traps.* Physical Review, 1956. **103**(6): p. 1648-1656.

93. Jaffe, B., W.R. Cook, and H. Jaffe, *Piezoelectric Ceramics*. 1971, London: Academic Press.

94. Bell, A.J., A.J. Moulson, and L.E. Cross, *The Effect Of Grain Size On The Permittivity Of $BaTio_3$.* Ferroelectrics, 1984. **54**(1).

95. Frey, M.H. and D.A. Payne, *Grain-Size Effect On Structure And Phase Transformations For Barium Titanate.* Physical Review B, 1996. **54**(5).

96. Meyers, M.A. and E. Ashworth, *A Model for the Effect of Grain Size on the Yield Stress of Metals.* Philosophical Magazine A, 1982. **46**(5): p. 737-759.

97. Tuttle, B.A., et al., *Relationships Between Ferroelectric 90° Domain Formation and Electrical Properties of Chemically Prepared Pb(Zr, Ti)O3 Thin Films*, in *Science and Technology of Electroceramic Films*, O. Auciello and R. Waser, Editors. 1995. p. 167-175.

98. Brennecka, G.L., et al., *Use of stress to produce highly oriented tetragonal lead zirconate titanate (PZT 40/60) thin films and resulting electrical properties.* Journal of the American Ceramic Society, 2004. **87**(8): p. 1459-1465.

99. Malzbender, J., *Stress profile and thermal expansion of layered materials determined from surface stresses.* Applied Physics Letters, 2004. **84**.

100. Hong, E., et al., *Residual stress development in Pb(Zr,Ti)O_3/ZrO_2/SiO_2 stacks for piezoelectric microactuators.* Thin Solid Films, 2006. **510**: p. 213-221.

101. Chen, X., D.N. Fang, and K.C. Hwang, *Micromechanics Simulation Of Ferroelectric Polarization Switching.* Acta Materiala, 1997. **45**(8): p. 3181-3189.

102. Fang, W., *Determination of the elastic modulus of thin film materials using self-deformed micromachined cantilevers.* Journal of Micromechanical Microengineering, 1999. **9**: p. 230-235.

103. Cohen, R.E. and E.F. Heifets, H. *First Principles Computation of Elasticity of $Pb(Zr,Ti)O_3$: The importance of elasticity in piezoelectrics*. in *Fundamental Physics of Ferroelectrics 2001*. 2001. Melville, NY: American Institute of Physics

104. Volinsky, A.A., et al., *Microstructure And Mechanical Properties Of Electroplated Cu Thin Films.* Material Research Society Symposium, 2001. **649**.

105. Kim, K., et al. *Residual Stresses in the Electrode of Pt/Ti for the Thermal Detector with Thin-film Structure*. in *12th IEEE International Symposium on Applications of Ferroelectrics*. 2000. Honolulu, HI.

106. Korzhavyi, P.A. and B. Johansson, *Literature Review On The Properties Of Cuprous Oxide Cu_2O And The Process Of Copper Oxidation*, in *Technical Report*2011, Swedish Nuclear Fuel And Waste Management Co.

107. Nix, F.C. and D. MacNair, *The Thermal Expansion Of Pure Metals: Copper, Gold, Aluminum, Nickel, And Iron.* Physical Review, 1941. **60**: p. 597-605.

108. Durand, M.A., *The Coefficient of Thermal Expansion of Magnesium Oxide.* Physics, 1936. **7**.

109. Kelman, M.B., et al., *Origin and implications of the observed rhombohedral phase in nominally tetragonal $Pb(Zr_{0.35}Ti_{0.65})O_3$ thin films.* Journal of Applied Physics, 2003. **94**(8).

110. Ramer, N.J., et al. *Stress-Induced Phase Transition in $Pb(Zr_{1/2}Ti_{1/2})O_3$*. in *The 5th Williamsburg workshop on first-principles calculations for ferroelectrics*. 1998. Williamsburg, VA: AIP Conference Proceedings.

111. Oh, S.H. and H.M. Jang, *Enhanced Thermodynamic Stability Of Tetragonal-Phase Field In Epitaxial $Pb(Zr,Ti)O_3$ Thin Films Under A Two-Dimensional Compressive Stress.* Applied Physics Letters, 1998. **72**.

112. Oh, S.H. and H.M. Jang, *Two-dimensional thermodynamic theory of epitaxial Pb.Zr,Ti.O3 thin films.* Physical Review B, 2000. **62**(22).

113. Oh, S.H. and H.M. Jang, *Epitaxial Pb(Zr, Ti)O_3 thin films with coexisting tetragonal and rhombohedral phases.* Physical Review B, 2001. **63**(13).

114. Feng, X., Y. Huang, and A.J. Rosakis, *On the Stoney Formula for a Thin Film/Substrate System With Nonuniform Substrate Thickness.* Transactions of the ASME, 2007. **74**.

115. Fitzpatrick, M.E., et al., *Measurement Good Practice Guide No. 52*, in *Determination of Residual Stresses by X-ray Diffraction - Issue 2*2005, National Physical Laboratory: Teddington, Middlesex, United Kingdom.

116. Withers, P.J., et al., *Methods for Obtaining the Strain-free Lattice Parameters When Using Diffraction to Determine Residual Stress.* Journal of Applied Crystallography, 2007. **40**: p. 891-904.

117. Daymond, M.R. and M.W. Johnson, *The determination of a stress-free lattice parameter within a stressed material using elastic anisotropy.* Journal of Applied Crystallography, 2001. **34**: p. 263-270.

118. Bonarski, J.T., L. Wcislak, and H.J. Bunge, *Investigation of inhomogeneous textures of coatings and near surface layers.* Material Science Forum, 1994. **157**: p. 111-117.

119. Kumar, A., U. Welzel, and E.J. Mittemeijer, *A Method for the Non-Destructive Analysis of Gradients of Mechanical Stresses by X-ray Diffraction Measurements at Fixed Penetration/Information Depths.* Journal of Applied Crystallography, 2006. **39**: p. 633-646.

120. Erbacher, T., et al., *X-ray diffraction at constant penetration depth – a viable approach for characterizing steep residual stress gradients.* Journal of Applied Crystallography, 2008. **41**: p. 377-385.

121. Maria, J.-P., et al., *Lead Zirconate Titanate Thin Films on Base-Metal Foils: An Approach for Embedded High-Permittivity Passive Components.* Journal of the American Ceramic Society, 2001. **84**(10): p. 2436-2438.

122. Kim, T., et al., *Lead Zirconate Titanate Thin Film Capacitors on Electroless Nickel Coated Copper Foils for Embedded Passive Applications.* Thin Solid Films, 2007. **515**: p. 7331-7336.

123. Losego, M.D., J.F. Ihlefeld, and J.-P. Maria, *Importance of Solution Chemistry in Preparing Sol-Gel PZT Thin Films Directly on Copper Surfaces.* Chemistry of Materials, 2008. **20**: p. 303-307.

124. Ohring, M., *Materials Science of Thin Films*. 2002, San Diego, CA: Academic Press, *An Imprint of Elsevier*.

125. Aulika, I., et al., *Compositional And Optical Gradient In Films Of $PbZr_xTi_{1-x}O_3$ (PZT) Family*, in *Ferroelectrics - Physical Effects*, M. Lallart, Editor. 2011, Intech. p. 307-453.

126. Vidyarthi, V.S., et al., *Plasma Emission Controlled Multi-Target Reactive Sputtering For In-Situ Crystallized $Pb(Zr,Ti)O_3$ Thin Films On 6" Si-Wafers.* Thin Solid Films, 2007. **515**: p. 3547-3553.

127. Etin, A., et al., *Controlled Elemental Depth Profile In Sol–Gel-Derived PZT Films.* Journal of the American Ceramic Society, 2006. **89**(8): p. 2387-2393.

128. Calderon, V., *Design and implementation of a controlled pO2 system for annealing electroceramic thin films on flexible metallic substrates*, in *Mechanical, Industrial Manufacturing Engineering*2010, Oregon State University: Oregon, U.S. p. 58.

129. Gaskell, D.R., *Introduction to the Thermodynamics of Materials, Fifth Edition*. 2008: Taylor and Francis.

130. Nittala, K., et al., *Phase Evolution In Solution Deposited Pb-Deficient PLZT Thin Films.* Journal of Material Science, 2011. **46**: p. 2148-2154.

131. Swanson, F., in *Joint Committee for Powder Diffraction Standards (JCPDS)*1953, National Bureau of Standards (U.S.).

132. Jin, Z., in *Joint Committee for Powder Diffraction Standards (JCPDS)*1998, Testing and Analysis Centre: Suzhou University, P.R. China.

133. Prisedsky, V.V. and V.M. Vinogradov, *Fragmentation Of Diffusion Zone In High-Temperature Oxidation Of Copper.* Journal of Solid State Chemistry, 2004. **177**: p. 4258-4268.

134. Gao, W., et al., *Oxidation Behaviour Of Cu Thin Films On Si Wafer At 175–400C.* Materials Letters, 2001. **51**: p. 78-84.

135. O'Reilly, M., et al., *Investigation Of The Oxidation Behaviour Of Thin Film And Bulk Copper.* Applied Surface Science, 1995. **91**: p. 152-156.

136. White, W.B. and R. Roy, *Phase Relations In The System Lead-Oxygen.* Journal of the American Ceramic Society, 1964. **47**(5): p. 242-249.

137. Rigato, V., G. Maggioni, and G. Della Mea, *Influence Of The Sputtering Pressure On Lead Silicate Glassy Film Stoichiometry.* Surface and Coatings Technology, 1995. **74-75**: p. 173-177.

138. Cabrera, N. and N.F. Mott, *Theory of the Oxidation of Metals.* Reports on Progress in Physics, 1949. **12**.

139. Feng, Y., et al., *The corrosion behaviour of copper in neutral tap water. Part I: Corrosion mechanisms.* Corrosion Science, 1996. **38**(3): p. 369-385.

140. Feng, Y., et al., *The corrosion behaviour of copper in neutral tap water. Part II: Determination of corrosion rates.* Corrosion Science, 1996. **38**(3): p. 387-395.

141. Tragert, W.E. and W.D. Robertson, *The Crystallographic Dependence Of The Oxidation Potential Of Solid Copper.* Journal of the Electrochemical Society, 1955. **102**(2).

142. Eichel, R.-A., et al., *Local variations in defect polarization and covalent bonding in ferroelectric Cu^{2+}-doped PZT and KNN functional ceramics at the morphotropic phase boundary.* Physical Chemistry Chemical Physics, 2009. **11**: p. 8698-8705.

143. Schwaller, P., et al., *Rapid depth profiling of lead zirconate titanate (PZT) thin films by pulsed glow-discharge optical emission spectroscopy.* Surface and Interface Analysis, 2006. **38**: p. 757-760.

144. Deineka, A., et al., *Ellipsometric Investigations of the Refractive Index Depth Profile in PZT Thin Films.* Physica Status Solidi (a), 2001. **188**(4): p. 1549-1552.

145. Bastani, Y., et al., *Critical thickness for extrinsic contributions to the dielectric and piezoelectric response in lead zirconate titanate ultrathin films.* Journal of Applied Physics, 2011. **109**.

146. Wu, A., P.M. Vilarinho, and A.I. Kingon, *Ceramic Processing Strategies For Thick Films On Copper Foils.* Acta Materiala, 2010. **58**: p. 2282-2290.

147. Dawber, M., et al., *Depolarization Corrections To The Coercive Field In Thin-Film Ferroelectrics.* Journal of Physics: Condensed Matter, 2003. **15**: p. L393-398.

148. Ishida, J., et al., *Large Remanent Polarization And Coercive Force By 100% 180° Domain Switching In Epitaxial $Pb(Zr_{0.5}Ti_{0.5})O_3$ Capacitor.* Applied Physics Letters, 2002. **80**.

149. Kanno, I., et al., *Piezoelectric Properties Of c-Axis Oriented $Pb(Zr,Ti)O_3$ Thin Films.* Applied Physics Letters, 1997. **70**(11).

150. McGilp, J.F., *On predicting the chemical reactivity of metal-semiconductor interfaces.* Journal of Physics C: Solid State Physics, 1984. **17**: p. 2249-2254.

151. Catalan, G., et al., *Relaxor Features In Ferroelectric Superlattices: A Maxwell–Wagner Approach.* Applied Physics Letters, 2000. **77**.

152. Pintilie, L., et al., *The influence of the top-contact metal on the ferroelectric properties of epitaxial ferroelectric $Pb(Zr_{0.2}Ti_{0.8})O_3$ thin films.* Journal of Applied Physics, 2008. **104**.

153. Paul, G.K., et al., *Defects In Cu_2O Studied By Deep Level Transient Spectroscopy.* Applied Physics Letters, 2006. **88**.

154. Wright, A.F. and J.S. Nelson, *Theory Of The Copper Vacancy In Cuprous Oxide.* Journal of Applied Physics, 2002. **92**.

155. Scanlon, D.O., B.J. Morgan, and G.W. Watson, *Modeling The Polaronic Nature Of P-Type Defects In Cu_2O: The Failure Of GGA And GGA+U.* Journal of Chemical Physics, 2009. **131**: p. 124703.

156. Peterson, N.L. and C.L. Wiley, *Diffusion And Point Defects In Cu_2O.* Journal of Physics and Chemistry of Solids, 1984. **45**(3): p. 281-294.

157. Porat, O. and I. Riess, *Defect Chemistry Of $Cu_{2-y}O$ At Elevated Temperatures. Part I: Nonstoichiometry, Phase Width And Dominant Point Defects.* Solid State Ionics, 1994. **74**: p. 229-238.

158. Tretyakov, Y.D., et al., *Nonstoichiometry And Defect Structures In Copper Oxides And Ferrites.* Journal of Solid State Chemistry, 1972. **5**: p. 157-167.

159. Xue, J. and R. Dieckmann, *The Non-Stoichiometry And The Point Defect Structure Of Cuprous Oxide ($Cu_{2-\Delta}O$).* Journal of Physics and Chemistry of Solids, 1990. **51**: p. 1263-1275.

160. Raymond, M.V. and D.M. Smyth, *Defects And Charge Transport In Perovskite Ferroelectrics.* Journal of Physics and Chemistry of Solids, 1996. **57**(10): p. 1507-1511.

161. Smyth, D.M. and M.P. Harmer, *Long Term Stability In Thin Film Ferroelectric Memories*, in *Final Report*1994, Advanced Research Projects Agency Office Of Naval Research.

162. Parui, J. and S.B. Krupanidhi, *Slim P-E Hysteresis Loop And Anomalous Dielectric Response In Sol-Gel Derived Antiferroelectric $PbZrO_2$ Thin Films.* Journal of Applied Physics, 2008. **104**.

163. Zametin, V.I., *Absorption Edge Anomalies in Polar Semiconductors and Dielectrics at Phase Transitions.* Physica Status Solidi (b), 1984. **124**(2): p. 625-640.

164. Berfield, T.A., et al., *Residual stress effects on piezoelectric response of sol-gel derived lead zirconate titanate thin films.* Journal of Applied Physics, 2007. **101**.

165. Choudhury, S., et al., *Strain effect on coercive field of epitaxial barium titanate thin films.* Applied Physics Letters, 2008. **92**.

166. Jang, J.W., et al., *Ninety degree domains in rf-sputtered $BaTiO_3$ thin films on platinum substrates.* Japanese Journal of Applied Physics, 1997. **36**(11): p. 6937-6941.

167. Heifets, E. and R.E. Cohen, *Ab initio study of elastic properties of $Pb(Ti,Zr)O_3$*, in *Fundamental Physics of Ferroelectrics*, R.E. Cohen, Editor. 2002, American Institute of Physics.

168. Corkovic, S. and Q. Zhang, *Correlation between critical coercive field and residual stress in antiferroelectric PZT 95/05 films.* Functional Materials Letters, 2008. **1**(1): p. 13-18.

169. Ong, R.J., D.A. Payne, and N.R. Sottos, *Processing effects for integrated PZT: Residual stress, thickness, and dielectric properties.* Journal of the American Ceramic Society, 2005. **88**(10): p. 2839-2847.

170. Gruverman, A., et al., *Asymmetric nanoscale swiitching in ferroelectric thin films by scanning force microscopy.* Applied Physics Letters, 2001. **78**.

171. Demczyk, B.G., R.S. Rai, and G. Thomas, *Ferroelectric domain structure of lanthanum-modified lead titanate ceramics.* Journal of the American Ceramic Society, 1990. **73**(3): p. 615-620.

172. Li, Y.F., et al., *Characterization of biaxial stress and its effect on optical properties of ZnO thin films.* Applied Physics Letters, 2007. **91**.

173. Nagarajan, V., et al., *Misfit dislocations in nanoscale ferroelectric heterostructures.* Applied Physics Letters, 2005. **86**.

174. Zhao, M.-H., et al., *Critical thickness for cracking of $Pb(Zr_{0.53}Ti_{0.47})O_3$ thin films deposited on Pt/Ti/Si(100) substrates.* Acta Materiala, 2002. **50**: p. 4241-4254.

175. Xiaoping, L., et al., *Electromechanical properties of a ceramic d_{31}-gradient flextensional actuator.* Journal of the American Ceramic Society, 2001. **84**(5): p. 996-1003.

176. Fett, T., D. Munz, and G. Thun, *Nonsymmetric deformation behavior of several PZT ceramics.* Journal of Materals Science Letters, 1999. **18**: p. 1641-1643.

177. Chen, H., Y.L. Yao, and J.W. Kysar, *Spatially resolved characterization of residual stress induced by micro scale laser shock peening.* Journal of Manufacturing Science and Engineering, 2004. **126**.

178. Prevey, P.S., *The use of Pearson VII distribution functions in x-ray diffraction residual stress measurement.* Advances in X-Ray Analysis, 1986. **29**: p. 103-111.

179. Lee, J.-W., et al., *Effects of residual stress on the electrical properties of PZT films.* Journal of the American Ceramic Society, 2007. **90**(4): p. 1077-1080.

180. Li, T., C. Chen, and J. Zhou, *Three dimensional phase field study on the thickness effect of ferroelectric polymer thin film.* Theoretical & Applied Mechanics Letters, 2011. **1**.

181. Desu, S.B., *Influence of stresses on the properties of ferroelectric $BaTiO_3$ thin films.* Journal of the Electrochemical Society, 1993. **140**(10): p. 2981-2987.

182. Lee, K. and S. Baik, *Morphotropic phase boundary in epitaxial Pb(Zr,Ti)O3 thin films: Two-dimensional planar size effect.* Applied Physics Letters, 2005. **86**.

183. Kelman, M.B., et al., *Thickness-dependent phase evolution of polycrystalline $Pb(Zr_{0.35}Ti_{0.65})O_3$ thin films.* Applied Physics Letters, 2002. **80**.

184. Ricinschi, D., et al., *First order reversal curves diagrams applied for the ferroelectric systems.* Journal of Optoelectronics and Advanced Materials, 2004. **6**(2): p. 623-627.

185. Robert, G., D. Damjanovic, and N. Setter, *Preisach modeling of ferroelectric pinched loops.* Applied Physics Letters, 2000. **77**.

186. Schloss, L.F. and P.C. McIntyre, *Polarization recovery of fatigued $Pb(Zr,Ti)O_3$ thin films: Switching current studies.* Journal of Applied Physics, 2003. **93**.

187. Stoleriu, L. and A. Stancu, *Analysis of switching properties of porous ferroelectric ceramics by means of first-order reversal curve diagrams.* Physical Review B, 2006. **74**.

188. Tagantsev, A.K., et al., *Polarization and fatigue in ferroelectric films: Basic experimental findings, phenomenological scenarios, and microscopic features.* Journal of Applied Physics, 2001. **90**.

189. Shur, V.Y., et al., *Kinetic approach for describing the fatigue effect in ferroelectrics.* Physics of the Solid State, 2002. **44**(11): p. 2145-2150.

190. Zhang, Q.M., et al., *Direct evaluation of domainwall and intrinsic contributions to the dielectric and piezoelectric response and their temperature dependence on lead zirconatetitanate ceramics.* Journal of Applied Physics, 1994. **75**.

191. Yi, J.W., W.Y. Shih, and W.H. Shih, *Effect of Length, Width and Mode on the Mass Detection Sensitivity of Piezoelectric Unimorph Cantilevers.* Journal of Applied Physics, 2002. **91**(3).

192. Maymon, G., *Structural Dynamics and Probabilistic Analysis for Engineers*. 2008: Butterworth-Heinemann.

193. Gavan, K.B., et al., *Size-dependent Effective Young's Modulus of Silicon Nitride Cantilevers.* Applied Physics Letters, 2009. **94**(23).

194. Mo, C.K., et al., *Energy Harvesting from a Vibrating Piezoelectric Unimorph Bender.* Journal of the Korean Society of Industrial Application, 2007. **10**(3): p. 157-163.

195. Poelma, R.H., et al., *A Numerical Experimental Approach for Characterizing the Elastic Properties of Thin Films: Application of Nanocantilevers.* Journal of Micromechanical Microengineering, 2011. **21**.